UiT
THE ARCTIC
UNIVERSITY
OF NORWAY

Faculty or Physics and Technology

Effect of permanent magnets on plasma confinement and ion beam generation in a double layer helicon plasma source

—

Erik Varberg

FYS-3900 Master's Thesis in Space Physics
June 2016

UNIVERSITY OF TROMSØ

Contents

List of Figures iii

List of Tables ix

Abstract xiii

1 Introduction 1

2 The Njord device 5

2.1 Sections of Njord 6

2.2 Generating plasma : Helicon source 8

2.3 Magnetic field configuration 11

3 Magnetic multipole confinement 17

3.1 Mathematical model of a multipole 19

3.2 Construction of the magnetic cusp field band 24

3.3 Characterization of the magnetic cusp 25

3.3.1 Estimation with MATLAB 27

3.3.2 Estimation with Data linearization 28

3.4 Effect of permanent magnets 32

4 Plasma diagnostics and analysis 35

4.1 The Retarding Field Energy Analyzer 36

4.2 Experimental set-up and diagnostics 39

4.3 IV-charts and data extraction 42
4.3.1 Finding the density using MATLAB 49

5 Experimental results **53**
5.1 Plasma potential results 54
5.1.1 RF-power variation 54
5.1.2 Pressure variation 54
5.1.3 Magnetic field variation 56
5.2 Ion density results 58
5.2.1 RF-power variation 58
5.2.2 Pressure variation 61
5.2.3 Magnetic field variation 66
5.3 Ion beam energy results 69

6 Discussions **75**
6.1 Ion beam flux 75
6.2 Density peak at low magnetic fields 82

7 Conclusion **89**

Appendices **91**

A Tables of the plasma potential results **93**

B Tables of the ion density results **101**

C Tables of the ion beam energy results **109**

D Tables of the RF-power data **115**

8 Bibliography **117**

List of Figures

2.1 A simple overview of the Njord device and its systems 5

2.2 The double saddle antenna (From [1]) 10

2.3 Simulated axial magnetic fields in the center at different magnetic coil currents I_{Coils}. 13

2.4 The increase of axial magnetic field strength at the center of Njord through the increase of the magnetic coil current I_{Coils}. 14

2.5 Simulated total axial magnetic field at different radial positions in Njord. 15

2.6 The cross section of the coupling between the aluminium casing and the dome. 16

3.1 Magnetic multipole configuration showing the magnetic field lines and the ion trajectories (Lieberman & Lichtenberg, 2005 [2]). 19

3.2 Set-up of the mathematical model 20

3.3 A profile of the magnetic field cusp created by three magnets. The positive/negative values represents the direction on which the magnets are pointing 22

3.4 Surface of the field amplitude. 23

3.5 The band with the magnets which creates a cusp field. . . . 24

3.6 The placement of the band around the source port. 26

3.7 The set-up for measuring the magnetic field strength of the cusp. Here it's measuring directly on the magnet. 27

3.8 Graph of the fitted functions directly on the magnets. 31

3.9 The simulated total axial magnetic field as in Fig. 2.5 with the added magnetic field from the cusps. 33

4.1 A typical RFEA probe with its dimentions. 37

4.2 A simple overview which shows the set-up for the RFEA's components and the biased grid configuration. 38

4.3 Output to discriminator. 40

4.4 Signal amplifier from the collector. 41

4.5 Plot of $I_i(V_B)$ (a) and the distribution function derived from it (b). 45

4.6 Plot of $I_i(V_B)$ and noise in front of V_P. 46

4.7 Plot of $I_i(V_B)$ (a) and the double-peak distribution function from its derivative (b). 50

4.8 Filtering of a set of derived data at RF power P_{in} : $400W$, gas flow Q : 2 SCCM and magnetic coil current I_{Coils} : $5A$ with filter size 9. 51

4.9 The function of MATLAB's trapz function with its restrictions. 52

5.1 Center plasma potential V_P as a function of RF-power at pressure P_{cap} : 0.65μ Bar (Flow $Q = 2$ SCCM), magnetic coil current $I_{Coils} = 5$ A and with and without magnet band. 55

5.2 Radial plasma potential V_P RF-power profiles at pressure P_{cap} : 0.65μ Bar (Flow $Q = 2$ SCCM) and magnetic coil current $I_{Coils} = 5$ A, without (a) and with (b) magnet band. 56

5.3 Center plasma potential V_P versus pressure at RF-power = 400 W and $I_{Coils} = 5$ A. 57

5.4 Radial plasma potential V_P profiles versus pressure at RF-power = 400W and magnetic coil current I_{Coils} = 5 A), without (a) and with (b) the magnet band. 58

5.5 Center plasma potential V_P versus magnetic coil current at RF-power : 400 W at pressure $P_{Cap} = 0.85$ μBar (Flow Q = 3 SCCM) at position r = 180 cm. 59

5.6 Radial plasma potential profiles V_P versus magnetic coil current at RF-power = 400 W, pressure $P_{Cap} = 0.85$ μBar (Flow Q = 3 SCCM), with and without the magnet band. 60

5.7 Center ion density n_i versus RF-power at pressure P_{cap} = 0.65μBar (Flow Q = 2 SCCM) and magnetic coil current $I_{Coils} = 5A$ with and without magnetic band. 61

5.8 Radial ion density n_i profiles versus RF-power of 400 W and 800 W at pressure P_{cap} = 0.65μBar (Flow Q = 2 SCCM) and magnetic coil current I_{Coils} = 5A, with and without magnetic band. 62

5.9 Radial density ratio n_r profiles versus RF-power at pressure P_{cap} = 0.65μBar (Flow Q = 2 SCCM) and magnetic coil current I_{Coils} = 5A at RF-power range $[100 - 400]$ W (a) and $[500 - 800]$ W (b). 63

5.10 Center ion density n_i pressure variation at RF-power = 400 W, $I_{Coils} = 5$ A, with and without the magnetic band. 64

5.11 Center ion density ratio n_r versus pressure with RF-power = 400 W and magnetic coil currents $I_{Coils} = 0$ A and 5 A. . 65

5.12 Radial ion density n_i profile versus pressure at RF-power = 400W, magnetic coil current I_{Coils} = 5 A, without (a) and with (b) the magnetic band. 65

5.13 Center ion density n_i versus magnetic coil current I_{Coils} at RF-power = 400W and pressure P_{Cap} = 0.85 μBar (Flow $Q = 3$ SCCM), with and without magnetic band. 67
5.14 Center ion density ratio n_r versus magnetic coil current I_{Coils} at RF-power = 400W and pressure $P_{Cap} = 0.85$ μBar (Flow $Q = 3$ SCCM). 68
5.15 Center ion beam energy E_{Beam} versus RF-power at pressure P_{Cap} = 0.65 μBar (Flow Q = 2 SCCM) and the magnetic coil current $I_{Coils} = 5$ A. 70
5.16 Radial ion beam energy E_{Beam} profiles versus RF-power at pressure P_{Cap} = 0.65 μBar (Flow Q = 2 SCCM) and magnetic coil current I_{Coils} = 5 A, without and with the magnetic band. 71
5.17 Radial ion beam energy E_{Beam} profiles versus pressure at magnetic coil current $I_{Coils} = 5$ A and RF-power range 400 W, without (a) and with (b) the magnetic band. 72
5.18 Center ion beam energy E_{Beam} versus magnetic coil current I_{Coils} at RF-power = 400 W, pressure P_{Cap} = 0.85 μBar (Flow Q = 3 SCCM), with and without the magnet band. . 73

6.1 Center ion beam velocity ratio v_{Br} versus RF-power at magnetic coil current I_{Coils} and pressure $P_{Cap} = 0.65$ μBar (Flow Q = 2 SCCM). 77
6.2 Center ion beam flux ratio ϕ_{Br} versus RF-power at magnetic coil current I_{Coils} = 5 A and pressure P_{Cap} = 0.65 μBar (Flow Q = 2 SCCM). 78
6.3 Center ion velocity ratio v_r versus pressure at RF-power = 400 W and magnetic coil current $I_{Coils} = 5$ A. 79
6.4 Center ion beam flux ratio ϕ_{Br} versus pressure at RF-power = 400 W and magnetic coil current $I_{Coils} = 5$ A. 80

6.5 Center ion beam velocity ratio v_{Br} versus magnetic coil current I_{Coils} at RF-power = 400 W and pressure $P_{Cap} = 0.85$ μBar (Flow Q = 3 SCCM). 81
6.6 Center ion beam flux ratio ϕ_{Br} versus magnetic coil current I_{Coils} at RF-power = 400 W and pressure $P_{Cap} = 0.85$ μBar (Flow Q = 3 SCCM). 82
6.7 Density peak profiles for different RF powers (K. Barada, [3]) 83
6.8 Ion density n_i versus RF-power and argon pressure ([4] 1993b). 86
6.9 Ion density n_i, electron temperature T_e and plasma potential V_P versus argon pressure in a RF-power = 500 W discharge with magnetic multipole confinement ([4] 1993b). 87

List of Tables

3.1 The average values of the measured magnetic field strength directly on the magnets and perpendicularly between the magnets 28

3.2 The results for the evaluated coefficients 31

4.1 Set-up for the experiments. 41

A.1 Radial plasma potential V_P profiles in [V] versus RF-power in [W] at pressure P_{cap} = 0.65 μBar (Flow Q = 2 SCCM) and magnetic coil current I_{Coils} = 5 A at RF-power range [100 − 400] W, with and without magnet band (S. Golay filter width: 15). 94

A.2 Radial plasma potential V_P profiles in [V] versus RF-power in [W] at pressure P_{cap} = 0.65 μBar (Flow Q = 2 SCCM) and magnetic coil current I_{Coils} = 5 A at RF-power range [500 − 800] W, with and without magnet band (S. Golay filter width: 15). 95

A.3 Radial plasma potential V_P profiles in [V] versus RF-power in [W] at pressure P_{cap} = 0.65 μBar (Flow Q = 2 SCCM) and magnetic coil current I_{Coils} = 0 A at RF-power range [100 − 400] W, with and without magnet band (S. Golay filter width: 9). 96

A.4 Radial plasma potential V_P profiles in [V] versus pressures at RF-power = 400 W and magnetic coil current $I_{Coils} = 5$ A, with and without magnet band (S. Golay filter width: 15). 97

A.5 Radial plasma potential V_P profiles in [V] versus pressures at RF-power = 400 W and magnetic coil current $I_{Coils} = 0$ A, with and without magnet band (S. Golay filter width: 15). 98

A.6 Center plasma potential V_P in [V] versus magnetic coil current I_{Coils} at RF-power = 400 W, pressure $P_{Cap} = 0.85$ μBar (Flow Q = 3 SCCM), with and without magnet band. 99

B.1 Radial ion density n_i profiles in m^{-3} versus RF-power at pressure $P_{Cap} = 0.65$ μBar (Flow Q = 2 SCCM) and magnetic coil current $I_{Coils} = 5$ A at RF-power range $[100 - 400]$ W, with and without magnet band (S. Golay filter width : 15). 102

B.2 Radial ion density n_i profiles in m^{-3} versus RF-power at pressure $P_{Cap} = 0.65$ μBar (Flow Q = 2 SCCM) and magnetic coil current $I_{Coils} = 5$ A at RF-power range $[500 - 800]$ W, with and without magnet band (S. Golay filter width : 15). 103

B.3 Radial ion density n_i profiles in m^{-3} versus pressure at RF-power = 400 W and magnetic coil current $I_{Coils} = 5$ A, with and without magnet band (S. Golay filter: 15) 104

B.4 Radial ion density n_i profiles in m^{-3} versus pressure at RF-power = 400 W and magnetic coil current $I_{Coils} = 0$ A, with and without magnet band (S. Golay filter: 15) 105

B.5 Radial ion density ratio n_r profiles versus pressure at RF-power = 400 W with magnetic coil current $I_{Coils} = 5$ A and $I_{Coils} = 0$ A. 106

B.6 Center ion density n_i versus magnetic coil current I_{Coils} at RF-power = 400 W an pressure P_{Cap} = 0.85 μBar (Q = 3 SCCM). 107

B.7 Center ion density ratio n_r versus of magnetic coil current I_{Coils} at RF-power 400 W, pressure P_{Cap} = 0.65 μBar (Flow Q = 2 SCCM). 107

C.1 Radial ion beam E_{Beam} profiles in [J] versus RF-power at pressure P_{Cap} = 0.65 μBar (Flow Q = 2 SCCM) and magnetic coil current I_{Coils} = 5 A, with and without magnet band. 110

C.2 Center ion beam energy E_{Beam} in [J] versus RF-Power at pressure P_{Cap} = 0.65 μBar (Q = 2 SCCM) and magnetic coil current I_{Coils} = 5 A, with and without magnet band. . . 110

C.3 Radial ion beam E_{Beam} profiles in [J] versus pressures at RF-power = 400 W and magnetic coil current I_{Coils} = 5 A, with and without magnet band. 111

C.4 Center ion beam energy E_{Beam} in [J] versus magnetic coil currents I_{Coils} at RF-power 400 W, pressure P_{Cap} = 0.85 μBar (Flow Q = 3 SCCM), with and without magnet band. 111

C.5 Center ion beam density ratio n_{Br} and ion beam velocity ratio v_{Br} versus RF-powers at pressure P_{Cap} = 0.65μ Bar (Flow Q = 2 SCCM) and magnetic coil current I_{Coils} = 5 A. 112

C.6 Center ion beam density ratio n_{Br} and ion beam velocity ratio v_{Br} versus pressures at RF-Power = 400 W and magnetic coil current I_{Coils} = 5 A. 112

C.7 Center ion beam density ratio n_{Br} and ion beam velocity ratio v_{Br} versus magnetic coil current I_{Coils} in [A] at RF-Power = 400 W and pressure P_{Cap} = 0.85 μBar (Flow Q = 3 SCCM). 113

D.1 RF-Power data at pressure $P_{Cap} = 0.65$ μBar (Flow Q = 2 SCCM), magnetic coil current $I_{Coils} = 5$ A at RF-power range $[100 - 800]$ W. 115
D.2 RF-Power data pressure profiles at RF-power = 400 W and magnetic coil current $I_{Coils} = 5$ A. 116
D.3 RF-Power data pressure profiles at RF-power = 400 W and magnetic coil current $I_{Coils} = 0$ A. 116
D.4 RF-Power data magnetic coil current profiles at RF-power = 400, pressure $P_{Cap} = 0.85$ μBar (Flow Q = 3 SCCM). . . 116

Abstract

The work described in this thesis was carried out to investigate how additional permanent magnets (PM) could affect the confinement and ion beam generation in a plasma which expands from a helicon source. PMs added to a plasma source systems has been shown to provide an increased plasma confinement, but is not widely used. This inexpensive and cheap method of using PMs which does not require any external power supply can be attached basically anywhere on any plasma source, and is especially effective when placed around a cylindrical source.

The effect of the added PMs was investigated experimentally by using a Retarding Field Energy Analyzer (RFEA) probe with and without the PMs. The ion current obtained from the plasma by biasing the RFEA at different potentials was analyzed as a function of the potential, and the ion distribution function was extracted. The different plasma characteristics was extracted from the distribution functions, and the results from the characteristics with and without the PMs were compared.

Highly mobile electrons and/or high-energetic ions which would be lost to the walls of the port can be reflected back towards the plasma interior by the magnetic cusp field from the PMs placed around the port. The PMs create a very strong magnetic field around the borders of the system of interest which decreases rapidly away from the magnets, providing little

change to the original system but results in a better plasma confinement because of the reduced plasma loss to the port wall. By adding PMs around a the port wall of a cylindrical plasma source with an expanding axial magnetic field, results have shown that the plasma density can in some cases be doubled. Another interesting effect introduced by the PMs is that the generation of ion beams in a helicon plasma source provided ions with a slight velocity reduction compared to the beam without PMs, but because of the increased ion beam density the flux of the ion beam is increased by a factor of up to 1.5. This might be useful for ion thrusters and beam propulsion systems based on a similar principle for beam generation which are being developed for satellites and space probes. Placement of PMs around the source exhaust-ports could thus provide an increased thrust.

Chapter 1

Introduction

Charged particle beam generation and plasma confinement are two interesting topics in plasma physics, used both for scientific research, technological advancements and in every day applications. Perhaps one of the most important confinement topic lie in the final development of fusion reactors, which are close of making it possible to give a sustainable energy source in the form of fusion energy [5]. In medical surgery, scalpels that use a cold plasma beam can cut through tissues in a careful manner while the heat decontaminates the exposed tissues and reduces bleeding with very little thermal damage, making the surgical scars more clean and heal more quickly compared to conventional methods [6, 7]. By generating a beam of ions, scientists and rocket engineers have managed to build space probes that can perform deep space or interplanetary missions to the planets in our solar system using ion thrusters as their method of propulsion. One such probe is the Dawn spacecraft, launched by NASA in 2007, which explored the asteroid belt and the dwarf planet Ceres orbiting between Mars and Jupiter, reaching velocities up to 10 km/s [8, 9]. Closer to earth, ion thrusters are commonly used by satellites to adjust their position in order to stay in their correct orbits, enabling communications around the earth [9–11].

The use of plasma as a method of propulsion has shown a number of interesting characteristics of a plasma source system. High-density plasmas made by a helicon Radio Frequency (RF) powered discharge (a type of RF-wave which will be explained in more detail later) in an expanding axial magnetic field has been shown to contain a strong current-free Double-Layer (DL). A DL is usually described as a region within two local equally, but oppositely charged, space charge layers in a plasma which are positioned close to each other [12]. This gives rise to an electric field $E(x)$ which depends on the distance x between the regions, which can be seen as a stationary localized drop in its potential $\phi(x)$, also dependent on the distance. This drop defines the electric field in the form of

$$E(x) = -\nabla\phi(x) \tag{1.1}$$

The electric field is much stronger on the inside of the DL than outside, meaning that the integration of the positive and negative charges nearly causes a cancellation. This means that even if the plasma is characterized in a quasi-neutral state, local charge separations can violate this, which can be described by the charge density $\rho(x)$ through the Poisson equation [13]

$$\phi(x) = \varepsilon_0 \nabla E(x) = e[n_i(x) - n_e(x)] \tag{1.2}$$

where ε_0 is the vacuum permittivity, e is the elemental charge and n_i and n_e are the ion density and electron density, respectively. DLs can be found in any plasma where a strong flux of charge carriers are present, which is necessary for DLs to exist, and they can be both stationary or moving, collisional or collision-less, with a current or current-free. The different types of DLs have all different characteristics, but one of the interesting abilities is a plasma with a high-potential area where incoming electrons with an energy lower than the DL are reflected. This causes ions from

the high-potential side to "see" a drop in the potential, which causes them to accelerate and form a beam of ions on the low-potential side of the DL. A larger potential drop will cause the ions to accelerate even more, increasing the flux of the positive beam. This flux of ions, which can be uniform over a large area, is the main mechanism for ion thrusters, and in combination with other methods of affecting the ion beam, such as an expanding magnetic field running parallel with it, can increase the flux even further.

Double layers have been observed in the plasma device Njord, which will be described in detail later. Measurements of the ion beam has been done [14, 15], and methods to increase the effect of the ion beam have been suggested. One of them is to add an external magnetic field around the port wall connecting the plasma source to the larger plasma chamber in order to decrease the loss of plasma to the port wall and increase the flux. This thesis will study the effect of the double-layer helicon plasma source under the influence of such an external magnetic field source. The applied magnetic field will be made by a set of permanent magnets which is placed around the exit of the source in the form of a magnet band, creating a magnetic cusp field configuration around the edge of the plasma. By comparing the plasma characteristics with the band on and off, one can extract data of how the cusp field affects the ion density and beam formation.

This thesis will include the following topics :

Chapter(2) gives an overview of the plasma device Njord along with its set-up and functions.

Chapter(3) explains the theory of the multipole confinement and the experimental set-up and calculations to determine its characteristics.

Chapter(4) explains the theories of the different plasma variables and

the methods of measure them in the plasma along with the set-up of the experiments.

Chapter(5) goes through the results from the experiments and shows the different plasma characteristics with and without the magnet band on.

Chapter(6) gives a discussion on how the permanent magnets behaves and how it has affected the plasma and beam characteristics.

Chapter(7) gives a small overview of the importance the magnet band has on plasma confinement and beam characteristics.

One small note : An unknown problem causes the first five references used in this thesis to be cited in the wrong order throughout the text. Different methods of putting the citations in a correct order was performed, but did not solve the problem.

Chapter 2

The Njord device

The plasma chamber used for the experiments is the device Njord, a stainless steel cylinder as showed in Fig. 2.1.

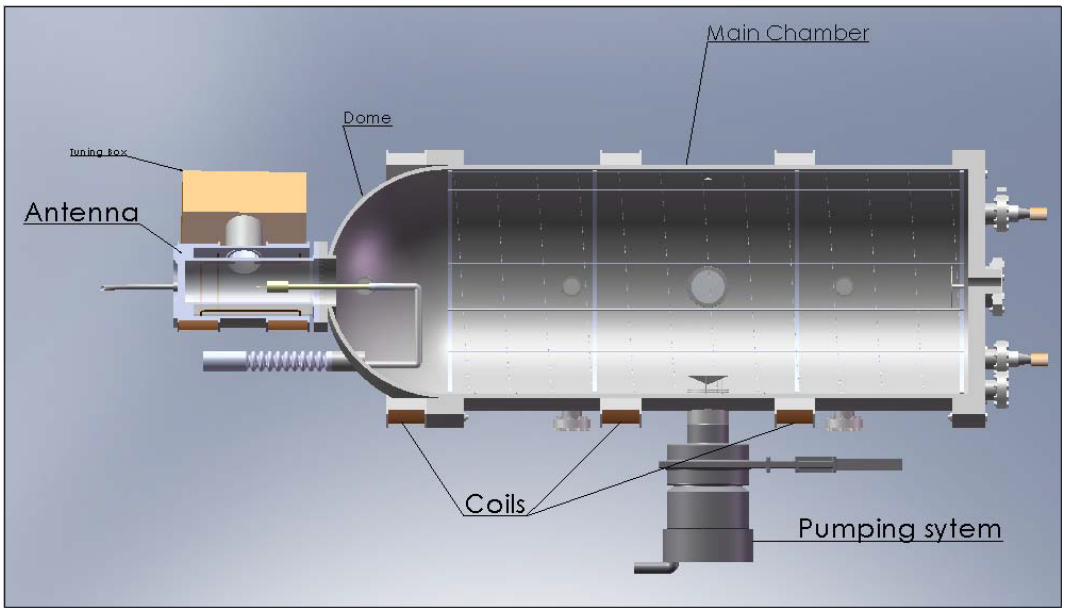

Figure 2.1: A simple overview of the Njord device and its systems

It is a versatile device for studying different plasma parameters and properties, particularly heating and instabilities in plasma flows and beam formations with relevance to near-earth space plasmas. This can be done by changing different control parameters via computer software or manual

controls. The plasma is generated by exciting gas (Argon) by applying inductively coupled high amplitude radio frequency (RF) waves with a frequency of 13.56 MHz through a helicon saddle antenna system, powered by a TRUMPF Hüttinger TruPlasma RF1002 RF generator. The device can create an ion beam by setting up an electric double layer (DL) with the helicon saddle antenna system where the gas is inserted and excited, and transport it by an induced magnetic field using coils. The device can also be prepared for a double plasma (DP) configuration by filaments attached on the wall running through the other end with an anode chamber opposite of the helicon source. The anode chamber can be biased with a voltage independent from the wall in the main chamber, which can form a beam of electrons or ions which can be channelled through a gridded hole between the two chambers. This option was not used during this work.

2.1 Sections of Njord

The Njord device can be split into three different sections which are coupled together, the source chamber, the dome, and the main chamber.

The source chamber is a pyrex glass cylinder with a length of 30 cm and a radius of 6.9 cm, closed at one end by an aluminium plate and mounted to the dome at the other end. The glass cylinder is encased by a aluminium cylinder of the same length and a radius of 10 cm. Argon gas is inserted into the end of the glass tube and excited by the helicon antenna which is mounted around the tube, inside the aluminium casing. Two sets of coils are mounted around the outside on the aluminium casing, and each coil is connected to a Delta Elektronika SM70-AR-24 power supply which creates a magnetic field inside the tube over 200 Gauss which expands into the

dome and guide the ionized gas into the main chamber.

The dome connects the inlet chamber and the main chamber, starting from a port of 10 cm radius at the inlet and ends at a 30 cm radius at the main chamber. Four 40CF conflat ports are placed on the side of the dome where a probe through-feed can be inserted into the chamber in order to acquire data.

The main chamber is the last section, with a radius of 30 cm and a length of 120 cm. Three sets of coils are fastened on the main chamber and can be used to improve confinement of the plasma towards the end where an anode chamber is installed. Two vacuum gauges are mounted side by side underneath the vacuum chamber, 30 cm from the pump port. One is a Boc-Edwards D147-01-000 wide-range (WR) gauge with a pressure range of $P_{WR} : [10^3 - 10^{-9}]$ mBar or $P_{WR} : [10^45 - 10^{-7}]$ Pa. The second one is a MKS Baratron gauge and is intended for the intermediate pressure range used for plasma operation with a pressure range of 133 Pa with a valid accuracy down to $P_{Cap} = 7 \times 10^{-3}$ Pa. A Stanford Research Systems Residual Gas Analyser (RGA) is a part of the vacuum diagnostics equipment for analysing mZ^{-1} ratios which is used for monitoring leaks and contaminations. This was not used during the work.

In the middle of the main chamber there is a chamber port with a radius of 7.5cm which is coupled to a two-pump system consisting of a Boc Edwards E2M28 rotary pump and a Leybolt 361C turbomolecular pump. The Edwards rotary pump has a stated pumping speed of 0.45 m^3/s, while the turbopump has a stated pumping speed of 0.56 m^3/s for N_2. The pumping system can bring the internal pressure down below to a base pressure around 10^{-4} Pa.

For a complete overview of Njord and the controllers, please read "Characterization of a magnetized plasma in cylindrical geometry" by Giulio Tribulato [1].

2.2 Generating plasma : Helicon source

The plasma in Njord is created by helicon propagation waves, and is a common method for plasma production [16]. A helicon wave is defined as a low-frequency electromagnetic wave with frequencies lower than electron cyclotron frequencies which can excist in ionized plasmas along with a magnetic field, first observed by Harding and Thonemann [17]. Later, Boswell [18] would use helicon waves through a new type of antenna, now known as a Boswell-antenna, in order to create plasmas through helicon discharge, a method of exciting the plasma through helicon waves through RF-heating, also known as a Inductively Coupled Plasma (ICP) [19]. This allows for the antenna be mounted outside of a discharge tube, isolating the plasma form any physical contact with the device as well as keeping it in a vacuum. One of the advantages of this set-up is that an axial magnetic field can create a helicon mode with a higher ionization efficiency which increases the plasma density larger than other RF-sources with comparable power outputs.

Another way of defining helicons is that they are propagating whistler wave modes rotating within an axially magnetized plasma column of finite radius [2]. The modes consist of an electric field E and a magnetic field B with a radial r-variation, axial kz-variation and usually an azimuthal $a\varphi$ variation, where k is the wave number of z and a and φ is the azimuthal

mode number and azimuthal angle, respectively. E and B usually propagates within a low-frequency, low magnetic high-density regime, with the frequency ω characterized as

$$\omega_{LH} \leq\leq \omega \leq\leq \omega_{ce} \tag{2.1}$$

$$\omega_{LH}^2 \approx \frac{1}{\omega_{ip}^{-2} + \omega_{ec}^{-2}} \tag{2.2}$$

$$\omega_{ep}^2 >> \omega\omega_{ec} \tag{2.3}$$

where ω_{LH} is the Lower-Hybrid frequency, ω_{ec} is the electron cyclotron frequency and ω_{ip} and ω_{ic} the ion plasma frequency and ion cyclotron frequency, respectively. In order to excite the plasma, the energy from the waves are either transferred to the electrons by collisional energy transfer, or a frequency ω is set which resonate with the electrons in the gas in order for the electrons to absorb the power from the waves. The waves will heat up the electrons which gyrates around the ions until they reach enough kinetic energy to escape their orbits, leaving positively charged ions behind. For argon gas, this resonance frequency is at $f = 13.56MHz$.

The helicon waves comes from an RF-driven antenna system which couples to the transverse structure mode, where the mode propagates along the column, releasing RF-power generated waves which are absorbed by the electrons. The waves which excites the plasma in Njord (and in many other types of RF-helicon plasma sources) comes from a double saddle antenna, illustrated in Fig. 2.2.

The antenna is powered by a RF generator, and the power output is controlled by a computer software where it can be set at a specific value up to a maximum of 2000 W. It is also able to measure the actual RF-power which goes in the plasma and the reflected RF-power, denoted P_{In}

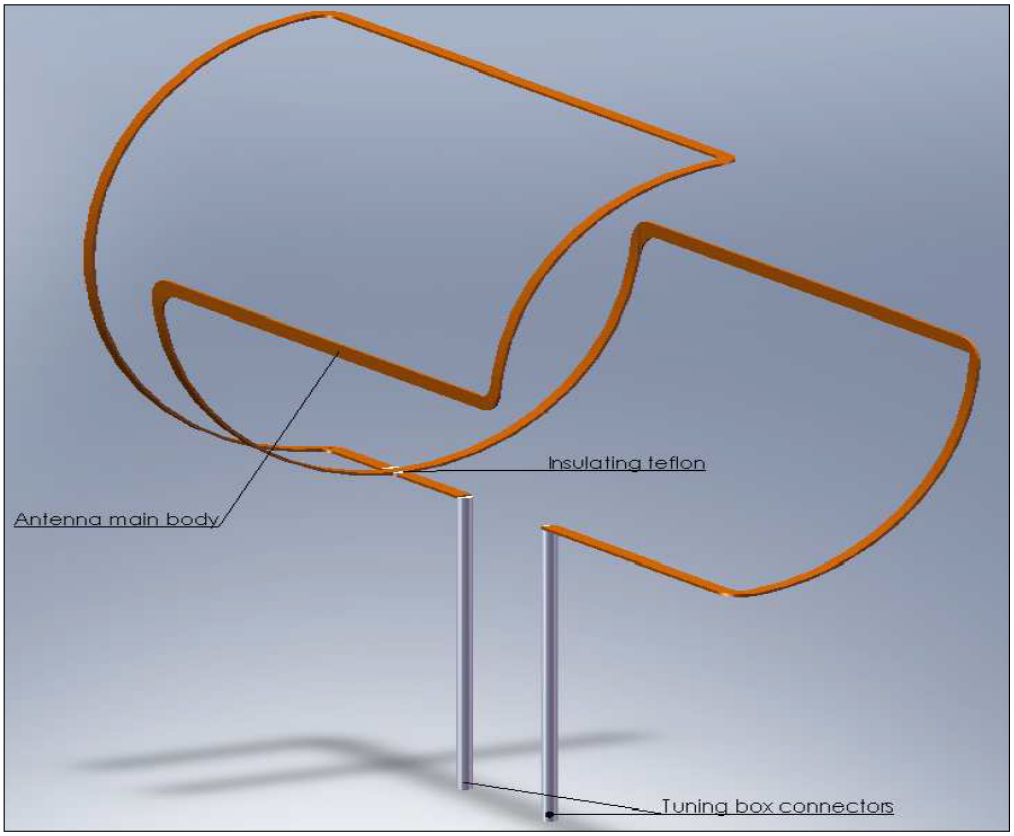

Figure 2.2: The double saddle antenna (From [1])

and P_{Ref}, respectively. The computer also measures the Voltage Standing Wave Ratio (VSWR), which measure the impedance matching of electrical loads to the characteristic impedance of a transmission line or a waveguide [20]. The VSWR is defined through the use of the voltage component of a standing wave (in this case the RF-waves from the RF generator) in a uniform transmission line consisting of a forward moving wave V_F and a reflected wave V_{Ref}, both with complex amplitudes. Reflection occur when the transmission line is terminated by a load/resistance which is different than the characteristic impedance. Using this one can define the reflection coefficient

$$\Gamma = \frac{|V_{Min}|}{|V_{Max}|} \tag{2.4}$$

which describes both the magnitude and the phase shift of the reflection. A reflection of $\Gamma = 1$ means that the line is an open circuit with a complete positive reflection. At $\Gamma = -1$ the line is short-circuited, giving a complete negative reflection. At $\Gamma = 0$ the line is perfectly matched with no reflection. If the line is not perfectly matched, the forward and reflected waves V_F and V_{Ref} will start to interact with each other, either constructively or cancelling each other. At a constructive interaction V_F and V_{Ref} are in phase, giving a maximum value of the wave

$$|V_{Max}| = |V_F| + |V_{Ref}| \tag{2.5}$$

When they are cancelling each other, they will create a minimum value of

$$|V_{Min}| = |V_F| - |V_{Ref}| \tag{2.6}$$

As Γ increases the ratio of V_{Max} to V_{Min} increases, and the mismatch of a line can be defined as the VSWR, defined as

$$VSWR = \frac{|V_{Max}|}{|V_{Min}} = \frac{1 + |\Gamma|}{1 - |\Gamma|} \tag{2.7}$$

The VSWR is defined in the range of $[1 \leq VSWR \leq \infty]$, where $\Gamma = 1$ is a matched load. However, if the reflected waves are small such that the reflection coefficient is $\Gamma \leq 1\%$, it will still read the VSWR as equal to one, as the transmission is practically in match.

2.3 Magnetic field configuration

The Njord device uses a magnetic field induced from a set of two coils mounted on the source chamber, creating an axial magnetic field. In addition, three larger coils are mounted on the main chamber to optimally

confine and transport the plasma downstream. These three chamber coils were not used in the experiments since the main concern here lies at the exit of the source.

The two coils, denoted as the source coils, have a radii of 12 cm, a length of 9.5 cm, a depth layer of 2 cm and are placed 21 cm from each other. The coils are made up with a copper wire with a diameter of 1.8 cm which is winded 370 times around the antenna housing. The magnetic field is induced by a coil current $I_{Coils} : [0 - 6]$ A. When the coil current is at 6 A the power must be switched off at regular intervals in order to prevent the coils from overheating, but at $I_{Coils} = 5$ A it can be left continuously on without any overheating.

In order to find out how the axial magnetic field behaves, a simulation-program developed by the staff at the Aurora Lab at the University of Tromsø with the programming tool Interactive Data Language (IDL) was used to calculate the magnetic field. This program can simulate different magnetic field configurations at various coil currents I_{Coils} in both axial and radial directions. Fig. 2.3 shows a simulation of a magnetic field at different I_{Coils} -values.

The resolution of the simulation is somewhat rough, as the output is calculated on a 30×30 pointgrid regardless of the axial and radial extent of the simulation window. The radial$\times$ axial resolution is set at $[0, 20]cm \times [0, 60]cm$ respectively, meaning that the radial position is set at the center of the cylinder and goes radially outward by 20 cm while the axial position starts at the outer end approximately 3 cm away from the first source coil and goes 60 cm inside the chamber to where the first source coils is placed approximately. Although the resolution is not very high, it gives a good

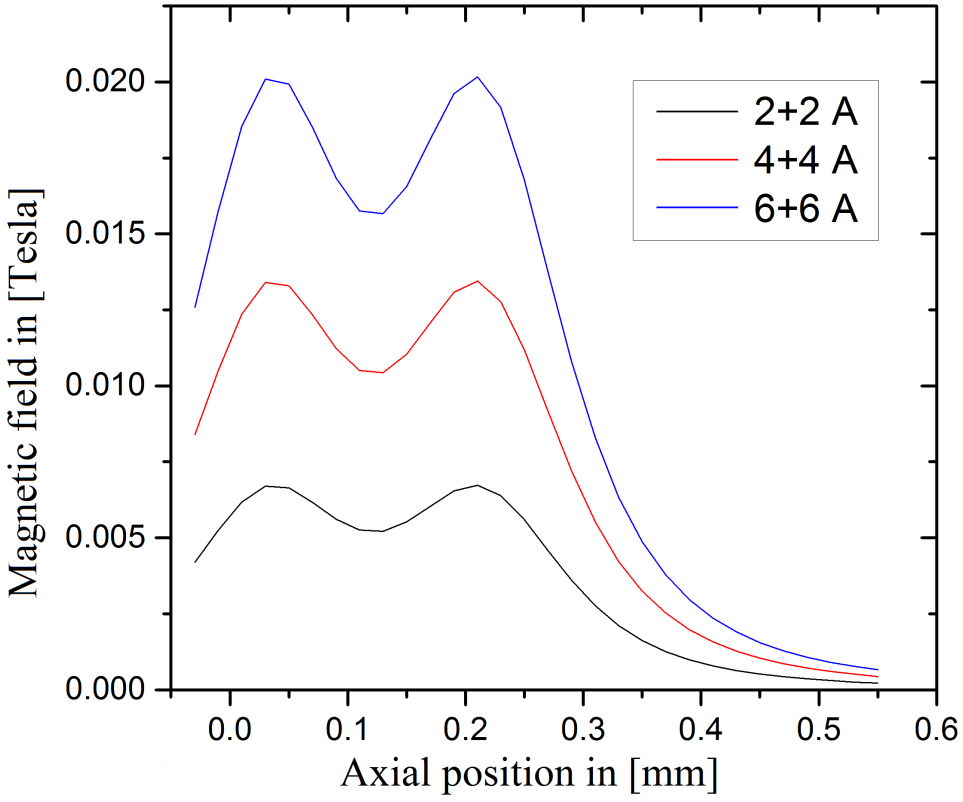

Figure 2.3: Simulated axial magnetic fields in the center at different magnetic coil currents I_{Coils}.

illustration of how the axial magnetic field develops.

Using the program the magnetic field and the field strength can be estimated at various coil currents at various locations. This is important in order to give an estimation of how the magnetic field behaves at the exit of the source. One of the first estimations was to find how the field strength in the radial center of Njord varies at different coil currents. The magnetic field strength at the center of Njord was found by choosing a coil current I_{Coils} range of $[1-6]$ A through the simulation and read the field strength from the pointgrid which represents the center of Njord. The results are shown in Fig. 2.4.

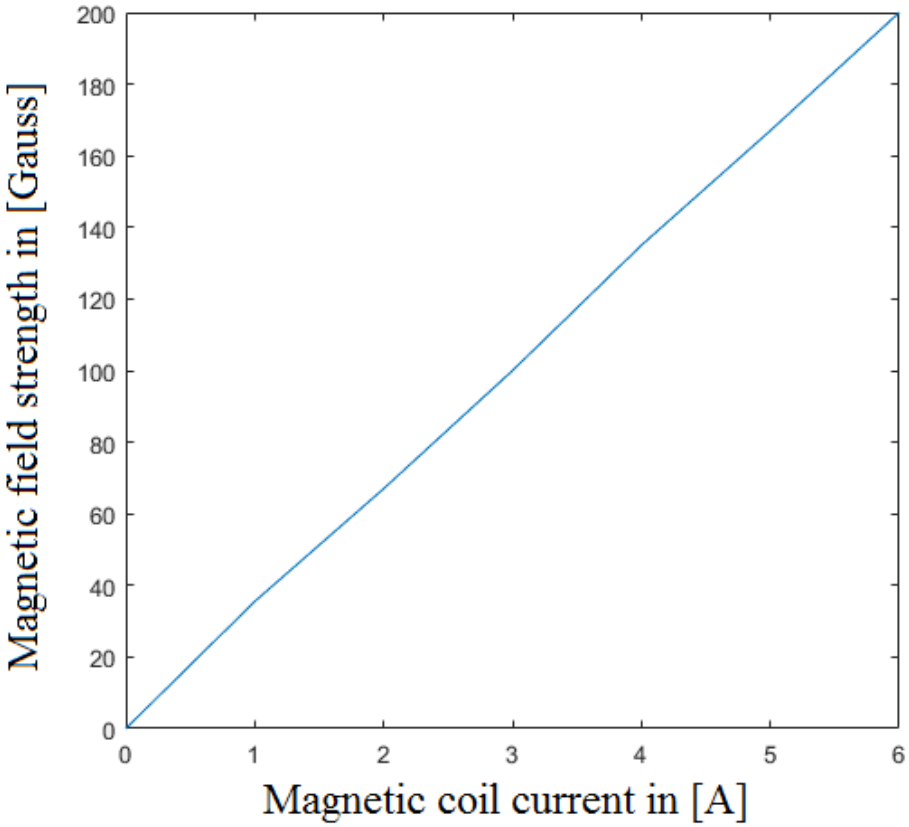

Figure 2.4: The increase of axial magnetic field strength at the center of Njord through the increase of the magnetic coil current I_{Coils}.

As the results shown, the magnetic field strength can in practical be described as a linear function of the magnetic coil current $B(I_{Coils})$, at least in the I_{Coils} -range what has been stimulated. This is useful if one wishes to estimate the magnetic field at different positions around the source.

Another simulation was done at $I_{Coils} = 5$ A at key radial positions to study how the magnetic field behaves after the coils and outwards up to approximately 6 cm from the source chamber. The key radial positions are the center (0 cm), the pyrex tube (6.9 cm), the aluminium casing (10 cm) the placement of the coils (11.5 cm) and a radial position called Magnet band (10.35 cm), which will be explained later. The results are shown in

Fig. 2.5.

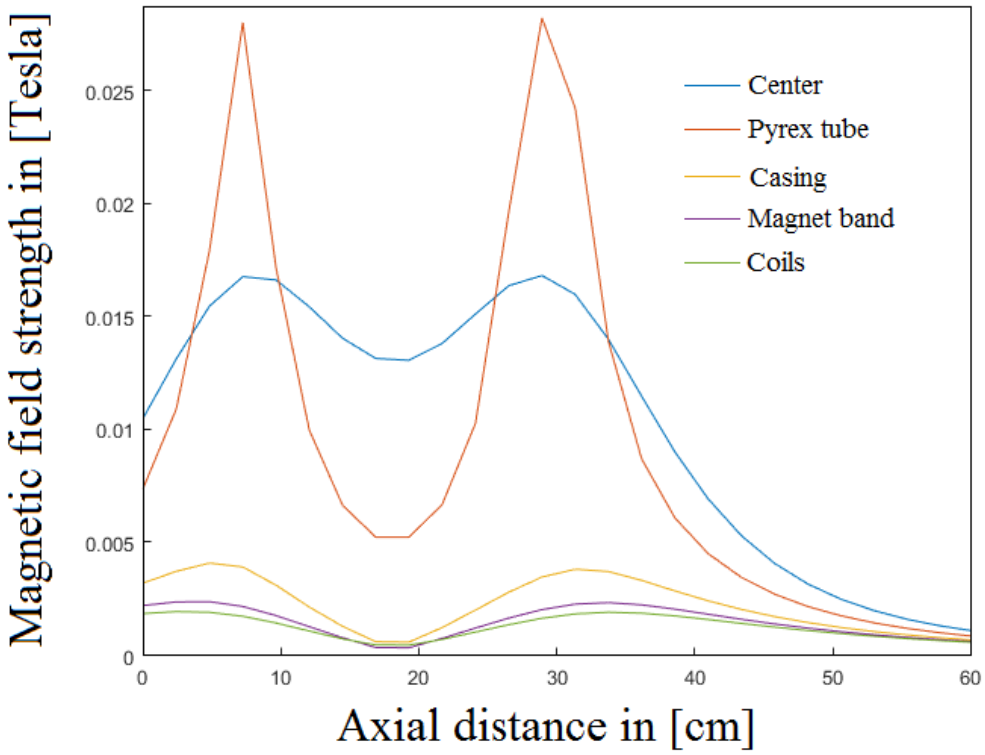

Figure 2.5: Simulated total axial magnetic field at different radial positions in Njord.

As the figure shows, the magnetic field reduces quickly at the end of the coils, and at a distance of approximately 43 cm, the magnetic field strength is very reduced due to the expanding field. Due to the expanding field there is a suspicion that plasma is hitting the walls at the port of the dome, causing plasma losses and reduced density inside Njord. One of the places there is a suspicion of plasma loss due to collisions with the wall is somewhere in the coupling between the aluminium casing of the source chamber and the dome, shown in Fig. 2.6, marked as a gridded area.

In order to prevent plasma loss, a device was made which fits in this area, repelling charged particles away from the walls. One way of repelling charges is by using a magnetic field, and since there is not a lot of space in

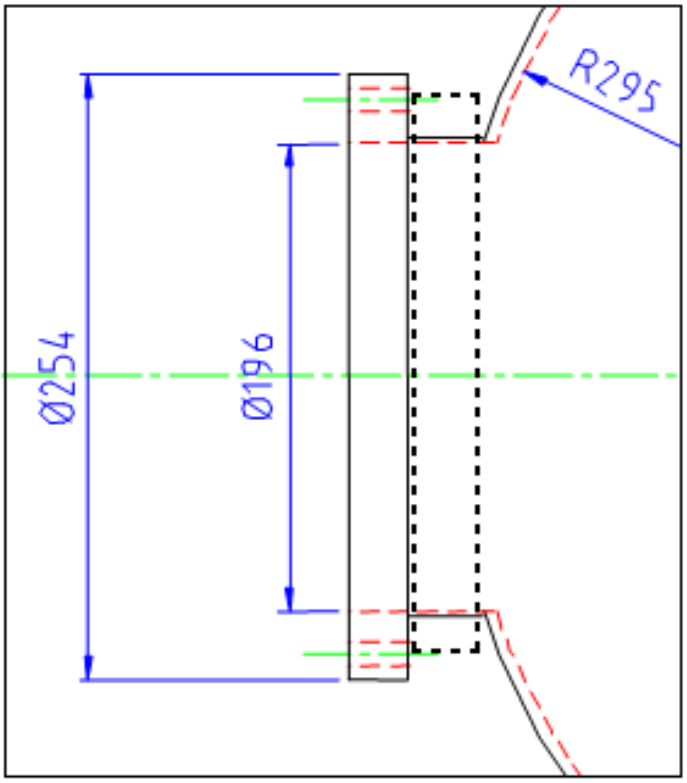

Figure 2.6: The cross section of the coupling between the aluminium casing and the dome.

this area, small permanent magnets are a good tool to achieve this magnetic field around it. The set-up for this device and its behaviour is described in the next chapter.

Chapter 3

Magnetic multipole confinement

Plasma confinement can be done in different ways, mostly through the use magnetic fields. The most common form of magnetic fields are induced fields through external coils around a plasma chamber which provides an axial magnetic field to limit cross-field transport of plasma to the walls. The most prominent cases for such confinements are Tokamak reactors for fusion research in order for the development of an energy source [5]. Small magnetic dipoles in the form of permanent magnets (PM) placed along the wall the plasma chamber has been applied to less extent, but have some good properties which can make ground for using magnets as a method of confinement [21]. Neodymium magnets which are readily available are capable of producing strong magnetic fields, even small magnets, which gives them big advantages in smaller devices and restricted areas. They can also be applied basically everywhere where a magnetic field is required since they don't need any power supply in order to work. Results from experiments involving PMs in a multipole configuration have shown different effects on low-pressure plasmas.

Leung [22] discovered that the plasma confinement was very dependent on the geometry of a multipole, but affected the electrons the most. High

energy electrons (higher than DC V_{sheath}) were more efficiently confined, and can be used as an ionization-source for a discharge if the Mean Free Path (MFP) of these electrons are large compared to the discharge size. Also, the plasma confinement has been improved, both in radial plasma uniformity and in low-temperature bulk plasma in a discharge. Takahashi [23–25] has experimented with PMs in an array around an expanding plasma, and has detected accelerated ions at supersonic speeds with the increase of the magnetic field strength by measuring the ion energy distribution at the exit. Chen [26] used a PM as a DC-magnetic source for a small helicon source inside a large chamber in order to find a better antenna coupling, which was found with a density higher than expected. He also experimented with a eight-tubed array of PMs around a helicon source, which both simplified the helicon sources and provided a much higher density profile [27].

The results shows that multipole confinement can be a very good tool in areas where plasma confinement is important. In order to understand the principle of a multipole confinement, one must understand how the field forms. A magnetic multipole usually consists of a row of permanent magnets placed side by side, where they alternate between the direction of the magnetic field by changing the direction of the north and south pole. Fig. 3.1 shows a configuration of a multipole consisting of 20 magnetic sources in a cylindrical geometry.

The row of magnetic fields from each magnet forms a cusp configuration where the magnetic field strength is at its maximum at the magnets and decays outwards from the cusps. This creates an area or volume which is mostly free of any magnetic fields except for the edges of said area/volume, which can reduce or remove the loss of plasma, increasing the density inside

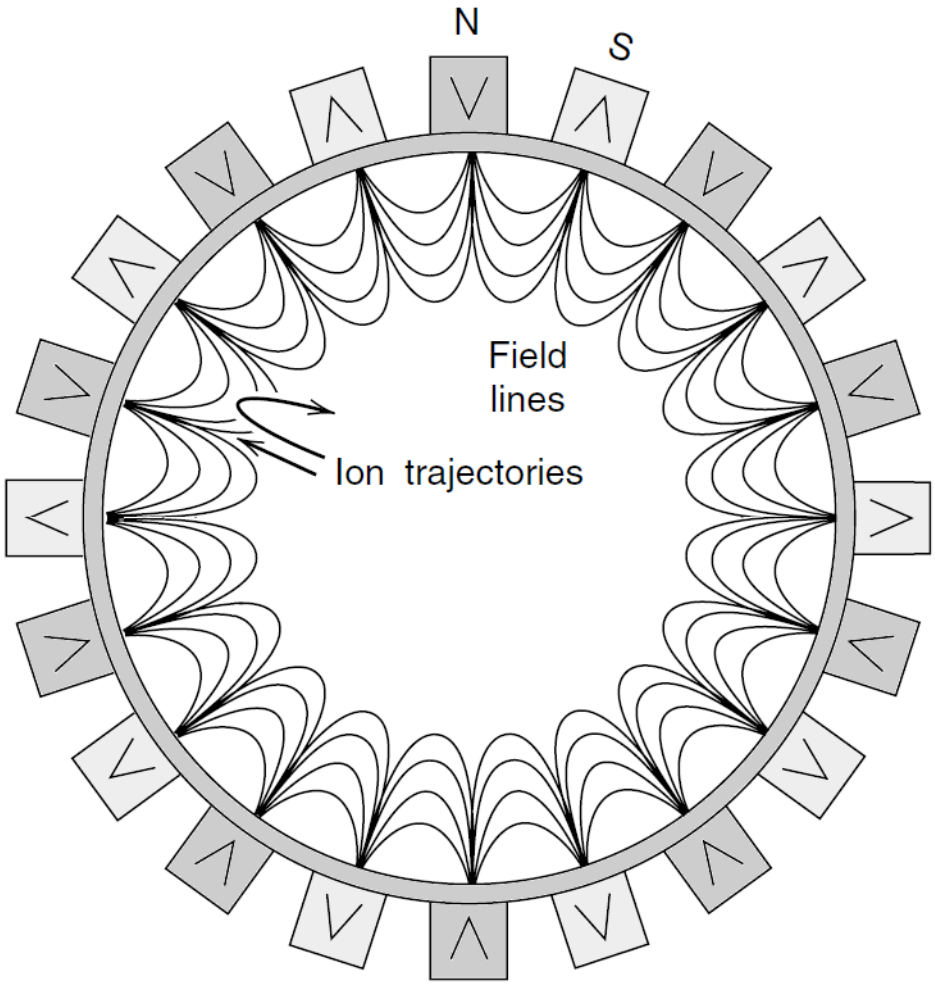

Figure 3.1: Magnetic multipole configuration showing the magnetic field lines and the ion trajectories (Lieberman & Lichtenberg, 2005 [2]).

it [2].

3.1 Mathematical model of a multipole

There are different methods to structure a mathematical model which describes a multipole system, especially in cylindrical geometry. However, one can give a simple structure by using a Cartesian system which describes a

row of magnets with a width w in a straight line with distance d between them, where $d > w$. This system is pictured in Fig. 3.2.

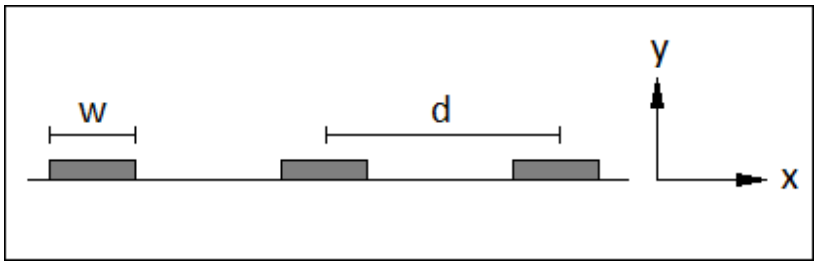

Figure 3.2: Set-up of the mathematical model

If the x-direction represents the line where the magnets lie and the y-direction is the direction away from the magnets, then the magnetic field can be described in the form of

$$\mathbf{B}(x, y) = B_0 \, \mathbf{f}(x) \, e^{-ky}, \tag{3.1}$$

where B_0 is the magnetic field strength at the magnets, $\mathbf{f}(x)$ describes the the magnetic field in the x-direction and the last term describes an exponential decay away from the magnets in the y-direction with the decay constant k. Since the y-dependent term only reduces exponentially in the positive y-direction, the two terms becomes linearly independent of each other, and thus Maxwell's laws of a constant magnetic field needs only be applied to $\mathbf{f}$ as long as $y \geq 0$. This means that $\mathbf{B}$ satisfies Laplace's equation for $y \geq 0$

$$\nabla^2 \mathbf{B} = B_0 \big[\nabla^2 \mathbf{f}(x) g(y) + \mathbf{f}(x) \nabla^2 g(y) \big], \quad g(y) = e^{-ky} \tag{3.2}$$

For the x-dependency, the equation gives a second order ordinary linear homogeneous equation (ODE)

$$\nabla^2 \mathbf{f}(x) = 0, \quad y \geq 0, \tag{3.3}$$

which gives the general solution

$$\mathbf{f}(x) = A \ \sin(\alpha x) \ \hat{\mathbf{x}} + B \ \cos(\alpha x) \ \hat{\mathbf{y}}, \tag{3.4}$$

where A and B are the amplitudes, α is the angular frequency (which in this term describes how the field oscillates between the magnets) and $\hat{\mathbf{x}}$ and $\hat{\mathbf{y}}$ are the unit vectors in the x-direction and the y-direction, respectively. Equating this back into $\mathbf{B}$, the system can be evaluated further by splitting it up into two separate equations in the form of

$$\mathbf{B}(x, y) = B_0 \Big[f_1(x, y) \ \hat{\mathbf{x}} + f_2(x, y) \ \hat{\mathbf{y}} \Big] \tag{3.5}$$

where

$$f_1(x, y) \ \hat{\mathbf{x}} = A \sin(\alpha x) e^{-ky} \hat{\mathbf{x}}$$
$$f_2(x, y) \ \hat{\mathbf{y}} + B \cos(\alpha x) e^{-ky} \ \hat{\mathbf{y}}$$

Since $\mathbf{B}$ satisfies the Laplacian, then it must satisfy $\nabla \cdot \mathbf{B} = 0$ and $\nabla \times \mathbf{B} = 0$. The cross-product gives for the z-component the following :

$$\frac{df_2}{dx} - \frac{df_1}{dy} = 0 \tag{3.6}$$

Evaluating this statement gives that $B = -A$, and by putting $A = 1$ gives :

$$\mathbf{B}(x,y) = B_0\big[\ \sin(\alpha x)\ \hat{\mathbf{x}} - \cos(\alpha x)\ \hat{\mathbf{y}}\ \big]e^{-ky} \tag{3.7}$$

The behaviour which Eq.(3.7) describes is depicted in Fig. 3.3, which describes the magnetic field cusp configuration of three permanent magnets.

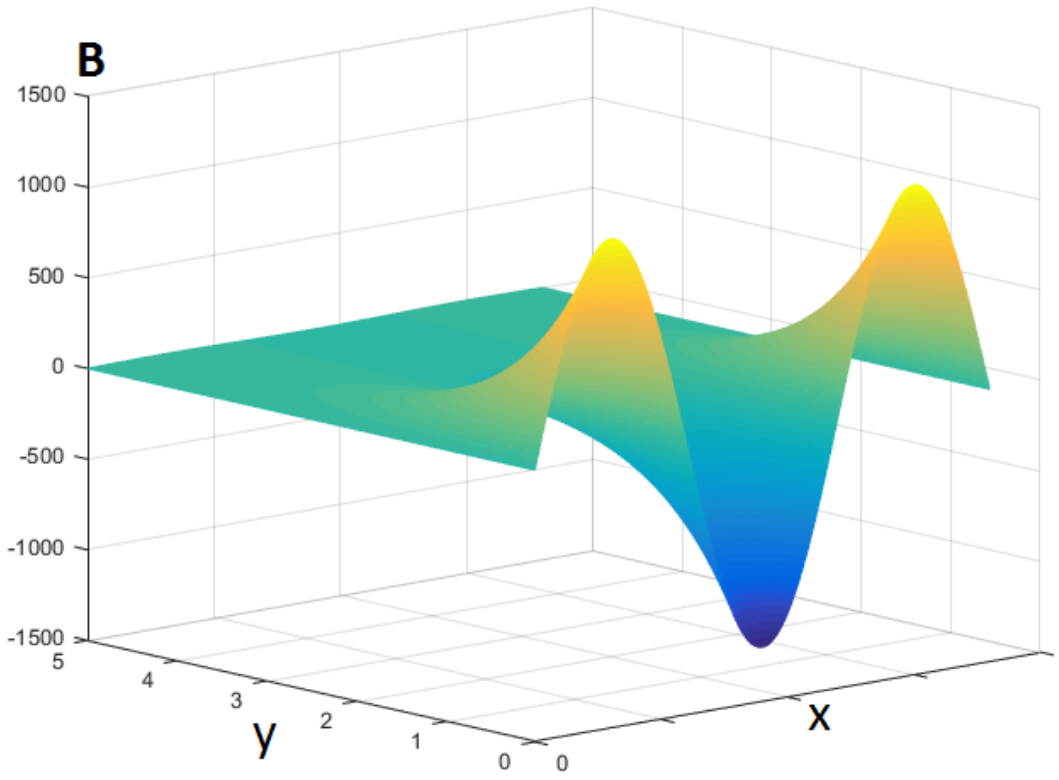

Figure 3.3: A profile of the magnetic field cusp created by three magnets. The positive/negative values represents the direction on which the magnets are pointing

The last remaining coefficients α and k are usually determined by the Boundary Value Conditions (BVCs) which the model is based on and/or experimented and evaluated on. Usually the model will use $\alpha = k = \frac{\pi}{d}$ because of the relation of the distance d and the width w of the magnets as discussed earlier. This can be extended further by evaluating the field

amplitude B using Pythagoras on $\mathbf{B}$ which gives :

$$B = \sqrt{\mathbf{B}^2} = B_0 e^{-ky} \tag{3.8}$$

This model gives a field amplitude which decays exponentially into the discharge column in the y-direction completely independent of x. This means that the field strength of the amplitude B can be described as a smooth surface along the y-direction. This model is pictured if Fig. 3.4 [28]. This description depends strongly on the relation between d and w. If $d >> w$ the model will start to break down as the magnetic field will only reach areas near the magnets, leaving large regions between them completely unaffected by any magnetic field.

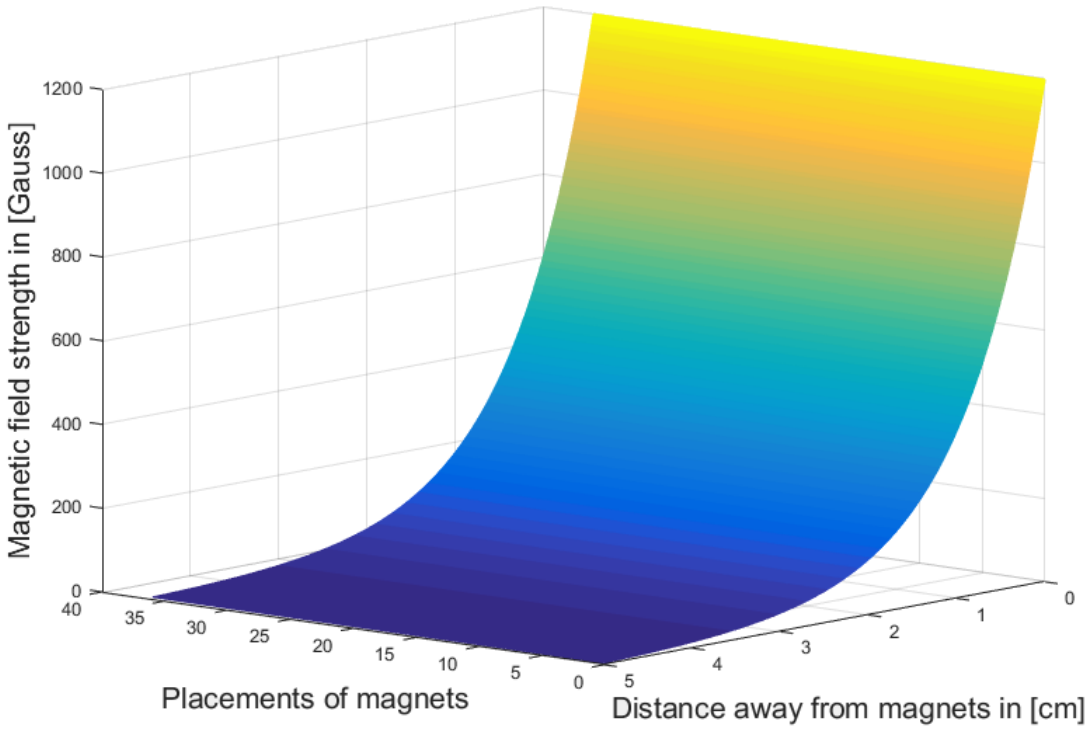

Figure 3.4: Surface of the field amplitude.

3.2 Construction of the magnetic cusp field band

In order to test the ability of confining and reducing the amount of plasma which are being dispersed out from the exit and into the port walls, a band which could hold a set of magnets in order to create a magnetic cusp was made. The band which was used to create the magnetic cusp is depicted in Fig. 3.5.

Figure 3.5: The band with the magnets which creates a cusp field.

The construction consists of a 72 cm long stainless steel assembly band and 18 neodymium magnets (Grade N42, Ring, 7/8"x(#8Countersink)x 1/8"), where each magnet is fastened by stainless bolts. In order to attatch the magnetic band to the case in a cylindrical shape, 6 ceramic extension pads are fastened on the band. It is placed around the source port of the dome, and the distance between the exit of the source chamber (the end of the pyrex glass tube) and the middle of the band is approx. 5.5 cm. Figure(3.6) shows how the band is placed at the end of the source.

3.3 Characterization of the magnetic cusp

The magnetic field configuration of the band was found experimentally by measuring the magnetic field strength away from the magnets using a Brockhaus Messtechnik 410 Gaussmeter and a transverse probe. This will give an indication on how the field is lining up and how far the field reaches in the chamber.

In order to measure the field strength in its cylindrical shape, a large piece of paper was used as a placement tool in order to position the probe correctly. Figure(3.7) shows the set-up of the experiment. A circle with the radii equal of the source chamber (approximately 10.35 cm) was drawn as the fixed position the magnet band would be placed, then 10 other circles from a radii of 1 cm to 10 cm was drawn on it as intervals. 18 radial lines where drawn on the paper from the outer radii to the center, representing the placements of the magnets, and 18 more were drawn in order to represent the placement between the magnets. Using the intersections where the radial lines and the circle meets as the position points for the probe, the magnetic field strength was measured both directly on the magnets and perpendicular between them until the Gauss-meter did not manage to

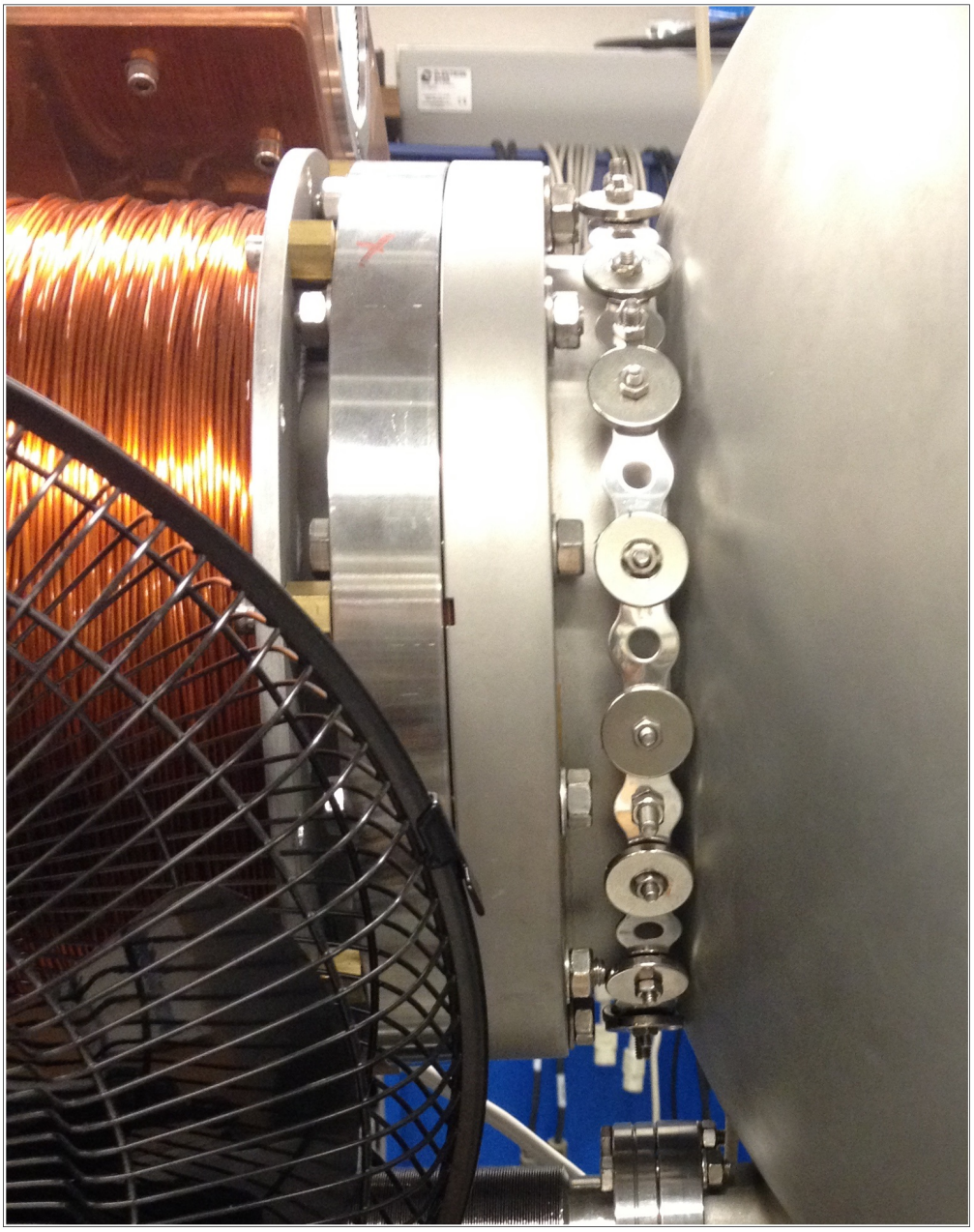

Figure 3.6: The placement of the band around the source port.

measure the field any longer.

After six rounds by measuring the field strength directly on and perpendicular between the magnets, an average value was estimated and used as a base for finding the field strength at the magnets and its decay constant. The results are shown in Table 3.3.

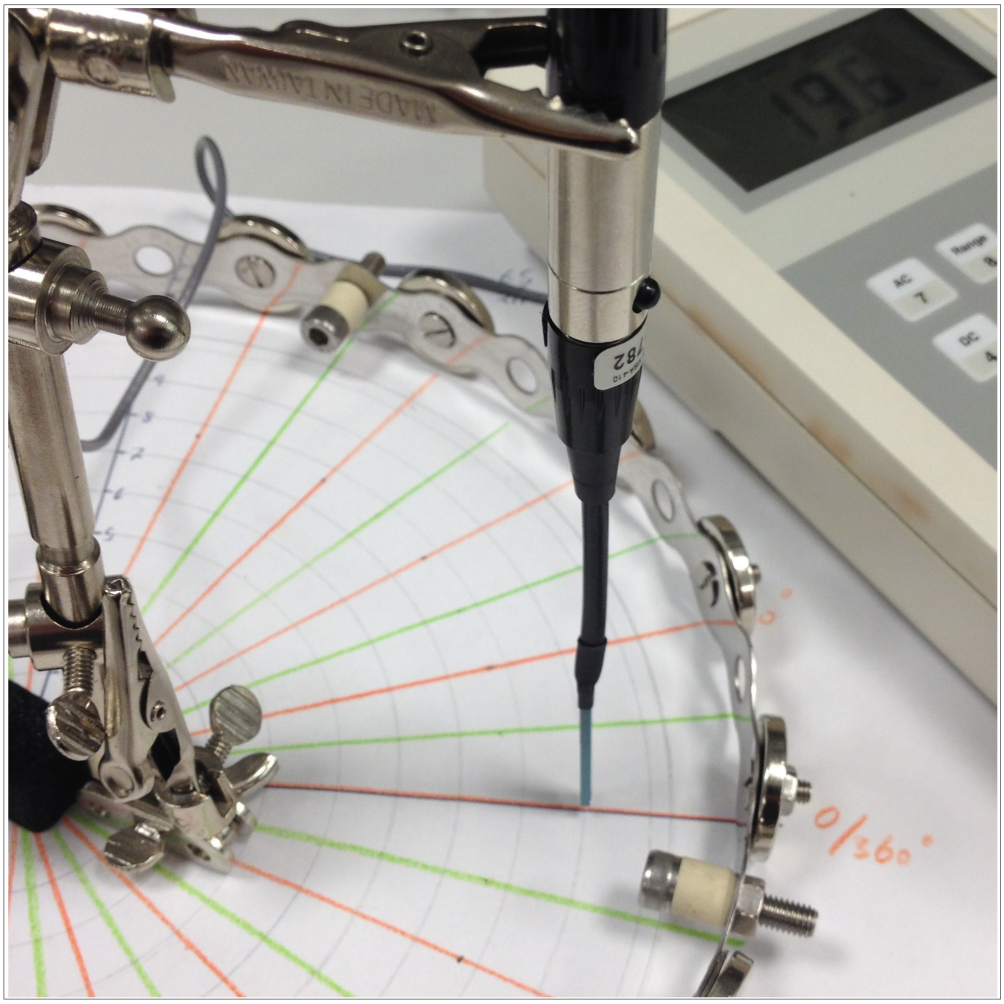

Figure 3.7: The set-up for measuring the magnetic field strength of the cusp. Here it's measuring directly on the magnet.

Using these results, a numerical solution for the field amplitude on the magnets B_0 and the decay constant k was estimated using Eq.(3.8) and two different tools. One method was the mathematical tool MATLAB, and the other with data linearization.

3.3.1 Estimation with MATLAB

Using the average values from Table 3.3 the two coefficients B_0 and k were found using the function fit(x,y,'fitType'), which is a built-in function

Table 3.1: The average values of the measured magnetic field strength directly on the magnets and perpendicularly between the magnets

r [cm]	On magnets (0°)	Between magnets (90°)
$r_1 \approx 10.65$	323	210
10	220	150
9	77	66
8	27.9	24.5
7	9	8.2
6	2.5	2.3
5	0.5	0.7

in the software program MATLAB. This function uses built-in parameter fittings in order to fit a curve to a set of data (x, y) which will estimate the coefficients of the curve to a type of function one wishes the data to be based on. This will give a numerically estimated value of the coefficients of the function with a 95 % confidence bounds. Using this function the data was estimated with two types of functions, an exponential function (Exp1) and a first degree polynomial (poly1) using the natural logarithm on the data set. The results are given in Table 3.2 in the next section along with the results from the data linearization.

3.3.2 Estimation with Data linearization

In order to find k and B_0 numerically, eq 3.8 is used and defined as a function of y since it is independent of x as discussed earlier, giving

$$B(y) = B_0 \, e^{-ky} \tag{3.9}$$

Since the model is based by a set of data measured at the distance y away from the magnets, it can be described as a discrete value for each measurement. This means that Eq.(3.9) can be set up as

$$B(y_n) = B_n = B_0 e^{-ky_n} \ , \quad n = 1, 2, 3, ...$$

Finding an explicit form straight away is not possible since the model describes a non-linear system. In order to solve the system the model must be linearized with the natural logarithm

$$\log B_n = b_n = \ln B_0 - ky_n \tag{3.10}$$

Since $\log(B_0)$ is constant, it can be written as c and thus keeping the model linear

$$b_n = c - ky_n \tag{3.11}$$

This gives a linear model with the two unknown coefficients, k and c, which can be estimated with a set of measured values for B_n for a set of distances y_n.

$$\begin{bmatrix} b_1 \\ b_2 \\ \vdots \\ b_n \end{bmatrix} = \begin{bmatrix} c - ky_1 \\ c - ky_2 \\ \vdots \\ c - ky_n \end{bmatrix}$$

This gives us a linear system in the form of the matrix equation $A\mathbf{x} = \mathbf{b}$, where

$$A = \begin{bmatrix} 1 & -y_1 \\ 1 & -y_2 \\ \vdots & \\ 1 & -y_n \end{bmatrix}, \quad \mathbf{x} = \begin{bmatrix} c \\ \\ k \end{bmatrix}, \quad \mathbf{b} = \begin{bmatrix} b_1 \\ b_2 \\ \vdots \\ b_n \end{bmatrix}$$

In order to solve $\mathbf{x}$, the normal equation $A^T A\mathbf{x} = A^T\mathbf{b}$ must be evaluated, where A^T is the transpose of matrix A. Using linear algebra, this gives

$$A^T A\mathbf{x} = M\mathbf{x}, \quad A^T\mathbf{b} = N \quad \rightarrow M\mathbf{x} = N \tag{3.12}$$

where

$$M = \begin{bmatrix} M_{11} & M_{12} \\ M_{21} & M_{22} \end{bmatrix} \quad , N = \begin{bmatrix} N_1 \\ N_2 \end{bmatrix}$$

Using row reduction on Eq.(3.12) in order to reduce the 2×2 matrix M into an identity-matrix I will give a direct solution to the coefficients c and k, where $c = ln(B_0)$. The solution from the data linearization is given in Table 3.2.

The results

Using MATLAB and data linearization, the set of coefficients for Eq.(3.8), was found. The results are shown in Table 3.2. If these coefficients are inserted in Eq.(3.8 and plotted, one can see which one gives the best representation for the data-set. This is shown in Fig. 3.8.

As Fig. 3.8 shows the coefficients which provides the closest fit for the measured units are provided by the exponential fit, even if the other two

Table 3.2: The results for the evaluated coefficients

Estimated values of the coefficients				
	On magnets (0°)		Between magnets (90°)	
	B_0	k	B_0	k
poly1	1435	-1.175	826	-1.061
Exp1	1087	-1.058	585	-0.8968
Data lin.	1200	-1.10	586	-0.8968

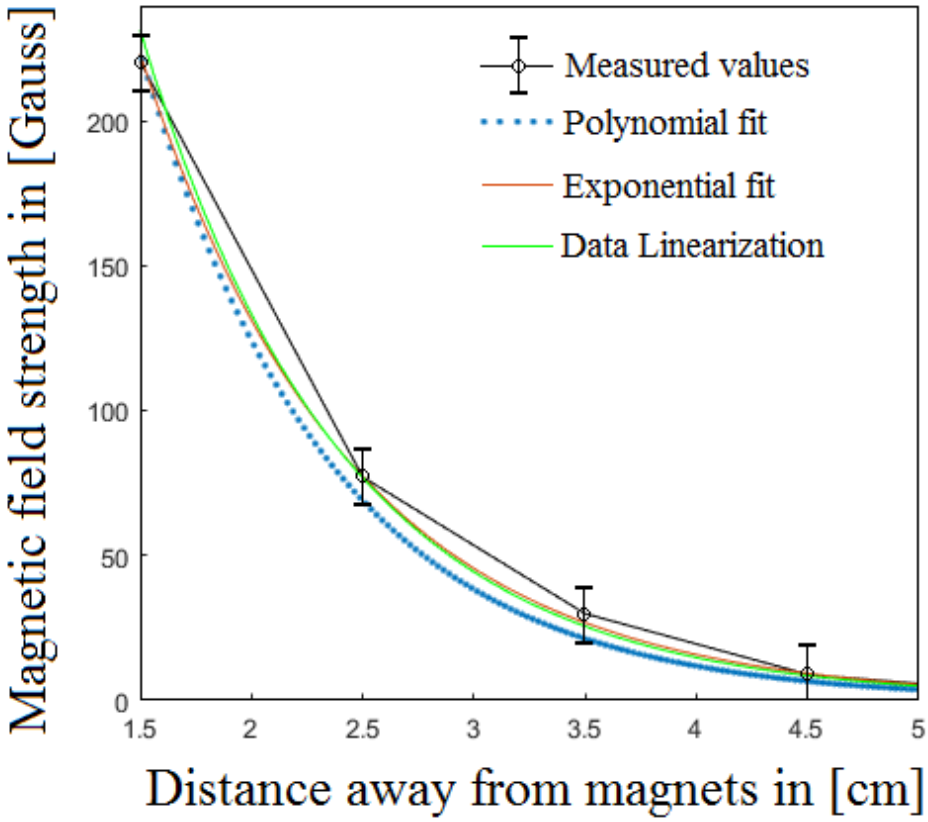

Figure 3.8: Graph of the fitted functions directly on the magnets.

provides an acceptable set of coefficients as well. However, this result is not completely without its faults. Direct measurements with the gauss-meter shows that the magnetic field of the magnets on the band is not consistent. Measurements with the probe directly on them has shown that

the field strength B_0 varies between $[1150 - 1500]$ Gauss. It is known that the alignment of the magnetic moment to the electrons in magnets slowly disalign, leading to loss of magnetic field strength over time. The model could be improved if the magnets had the same strength in order to get more consistent measurements, but it would not make a very large difference compared to what the model shows now. The decay constant k is at its most 10% different between the exponential fit and the polynomial fit, and all the models shows that the field strength is noticeable up to nearly 6 cm away from the magnets, meaning that the magnetic field reaches over halfway of the radius of the chamber. The magnets are also approx. 4.5 cm away radially from the opening of the source chamber, meaning that the plasma which exits the glass tube at the edges will be subjected to a magnetic field strength of approximately 10 Gauss when it reaches the point where the band is placed (5.5 cm away from the opening). This shows that the band is affecting the exit of the source and will provide a good application for the plasma as it expands towards the main chamber.

3.4 Effect of permanent magnets

As discovered in Section 3.3, the added magnetic cusp field configuration gives a noticeable added magnetic field strength in the radial direction towards the center of the probe. In order to illustrate this effect the original simulation described in Section 2.3 was altered by adding the magnetic field strength from the magnets to the total magnetic field strength to the source coils. As mentioned in the same section, the resolution is a bit low in order to give a fully accurate representation, but it does show the effect the cusp field gives, as shown in Fig. 3.9.

As Fig. 3.9 shows, the effect from the magnetic band provides a large

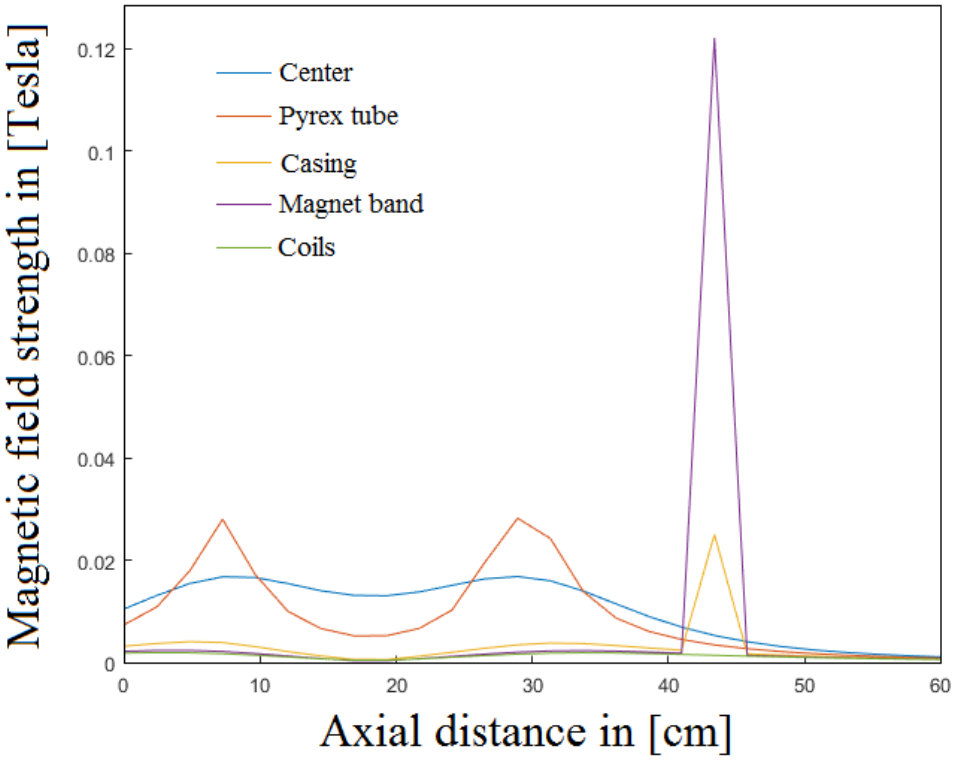

Figure 3.9: The simulated total axial magnetic field as in Fig. 2.5 with the added magnetic field from the cusps.

increase in the total magnetic field at the position of the band. Straight at the placement of the magnetic band the magnetic cusp field is much stronger than the axial magnetic field, which will greatly redirect plasma away from the edges, but vanishes quickly towards the center of the cylinder and is basically gone after the radii of the pyrex tube. This is exactly what the cusp field should do, it proved a strong magnetic field around the edge of the cylinder, but leaves the axial magnetic field at the source unaffected. The effect this has on the plasma characteristics, especially ion density, is an important topic. This was studied by performing experiments with and without the magnetic band at different set-ups in the Njord device. This is discussed in the next chapter.

Chapter 4

Plasma diagnostics and analysis

In order to understand the behaviour in low-temperature plasmas like the ones created in Njord, one needs to obtain information of its parameters. There are different methods of doing so, and one of them is by inserting an electrostatic probe directly inside the plasma. Such probes function by drawing a current from the plasma towards a small metal surface biased with a potential. This method of studying plasma characteristics was developed by Irving Langmuir and H. M. Mott-Smith in the mid-twenties, and the first probe to be developed by them is the now known Langmuir-probe [2]. The currents they draw will mostly consist of electrons because they are far more mobile than the heavier ions, resulting in the electron current I_e dominating the ion current I_i with an electron to ion current ratio of $I_e I_i^{-1} \approx \sqrt{m_i m_e^{-1}}$, which can make it difficult to study the ions and their properties. Since the interest in this work lies with the ions, a probe known as an Retarding Field Energy Analyzer (RFEA) which rejects electrons from entering the probe had to be used.

4.1 The Retarding Field Energy Analyzer

An electrostatic Retarding Field Energy Analyzer (RFEA) probe, often known as an Ion Energy Analyzer (IEA), is the most common probe to be used in order to estimate ion kinematics and beam properties [29, 30]. RFEAs are fairly large in size compared to other probes and thus disturb the plasma flowing around it, causing turbulence and space charge effects which can disturb the plasma potential and the ion current and reduce the energy resolution of the probe, which will be discussed later. Results have shown however, that they can provide reliable sets of some plasma characteristics [31–33], which is beneficial since RFEA probes are easy and cheap to make compared to other diagnostics, such as Laser Induced Fluorescence (LIF) [34, 35]. One of the main advantages with these probes for studying ions is that they repel nearly all electrons that arrive at the probe, allowing information of the ion velocity distribution to be obtained. The main limitation with RFEAs is that they can not distinguish between particle species or positive and negative charges, and due to the reduced energy resolution it is not possible to obtain a reliable estimate of the ion temperature in the plasma which is produced in Njord.

An RFEA probe consists of a series of thin metal grids, all of them biased by various potentials which can be used to separate electrons and ions with a certain energy level. Figure(4.2) gives a simple overview on how ions and electrons are separated by the grids in the RFEA and the corresponding grid configuration. The plasma flows towards the front (F) of the probe and encounters a gridded aperture in the front which lets some of the plasma pass through. The plasma that pass the aperture will encounter a large negative potential from the first grid which act as a repeller (R_1) where the remaining electrons will be reflected. The discriminator (D) repels an increasing part of ions by a bias potential (V_B) which is increasing

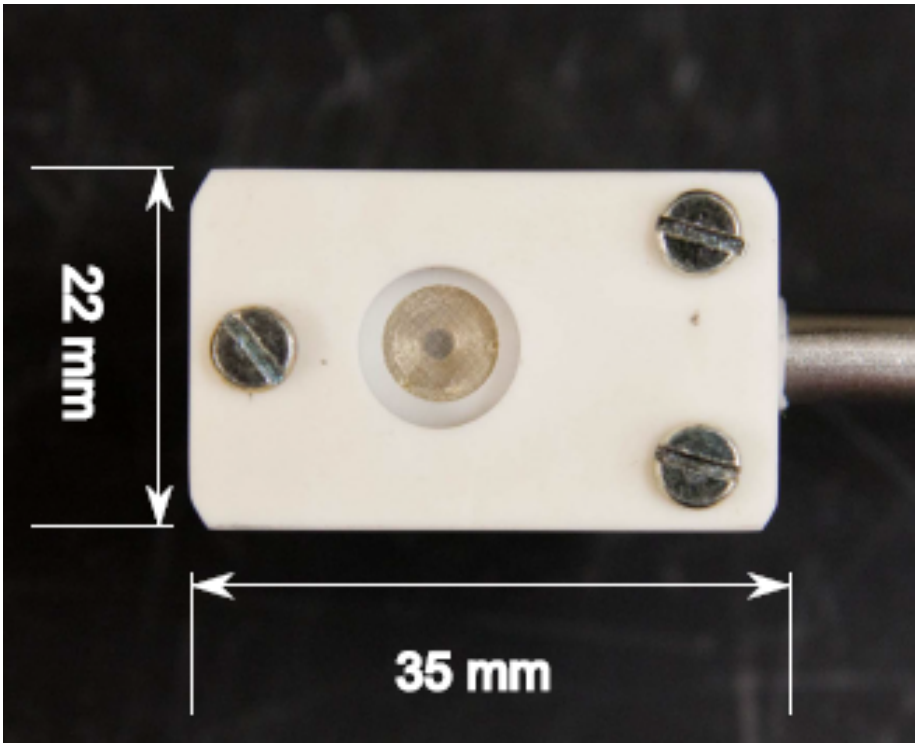

Figure 4.1: A typical RFEA probe with its dimentions.

from a large negative value to potentials above the plasma potential (V_P). This will only allow ions with sufficient kinetic energy to pass through, and by using the known potential of the discriminator the kinetic energy can be estimated. The secondary repeller (R_2) will allow the remaining plasma to pass through, but will prevent secondary electrons sputtered from the collector surface (C) to escape backwards. R_2 is biased negatively with respect to the C bias, which is set to collect the ions passing through D.

While this set-up is the most common, the RFEA can still measure ion dynamics without R_2, but runs the risk of having an electron current from sputtered electrons escaping the collector. This can affect the distribution function which can be extracted from the measurement and can cause inaccurate plasma parameters. The position of D and R_1 can be exchanged such that the two repellers are placed in front of C, but will function the same

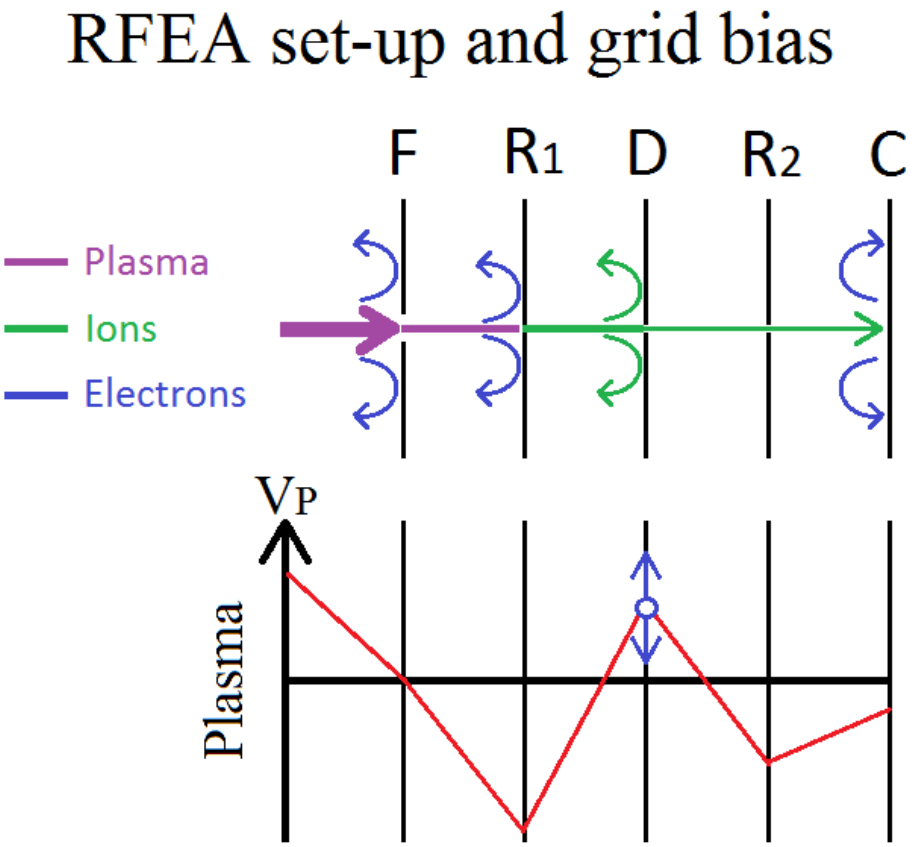

Figure 4.2: A simple overview which shows the set-up for the RFEA's components and the biased grid configuration.

way as the original structure described in Fig. 4.2 [30]. This configuration has in some cases proved beneficial in order to reduce noise. By turning off or remove the secondary repeller R_2 and switching the polarity on all grids the RFEA can be inverted to measure electron energies [36]. Lastly, the mesh in the grids can consist of different materials with a different transmission coefficient. The RFEA probe used in Njord consists of a ceramic housing with a floating aperture grid in the front. All of the four grids is made of a stainless steel mesh with a transmission factor of 44%. The meshes are spot-welded to 0.3mm thick brass spacers with 0.3mm ceramic spacers between them, giving a distance of 0.6mm between the grids. The

front grid is electrically connected to the housing, which is on a floating potential. The grids are biased negatively except for D, which is swept in a large bias range which is set manually.

4.2 Experimental set-up and diagnostics

The probe was installed on a 50cm long stainless steel rod with four insulated copper wires installed inside, where each is coupled to the RFEA's grids. The steel rod with the probe enters the chamber at the dome through a lateral flange and is installed on the electric step motor which controls the position of the probe. The repellers are connected individually to a Delta Elektronika ES0300-0.45 power supply, where R_1 is biased at -80V while R_2 is biased at $-30V$. The values for R_1 and R_2 are based on earlier experiments which have provided good data, but they can be adjusted if necessary and/or for other preferences. The discriminator is connected to a battery pack consisting of a series of $9V$ batteries which can be switched on or off individually, and continues to an isolated amplifier which amplifies the sweep set by a computer control to a probe potential ranging from -70V to 70V at multiple ramp steps. The isolated amplifier circuit is depicted in Fig. 4.3. The signal is then sent to a BNC-2090 connector block from National Instruments connected to a computer which can monitor and control the amplifier.

The collector is coupled to a battery pack consisting of several 9V batteries as well, used to bias the collector at -27V with respect to ground. The battery pack is then connected to a signal amplifier, which amplifies the collector current by a factor of 100 and measured across an exchangeable resistor to ground. Figure(4.4) shows the amplifier circuit. The signal

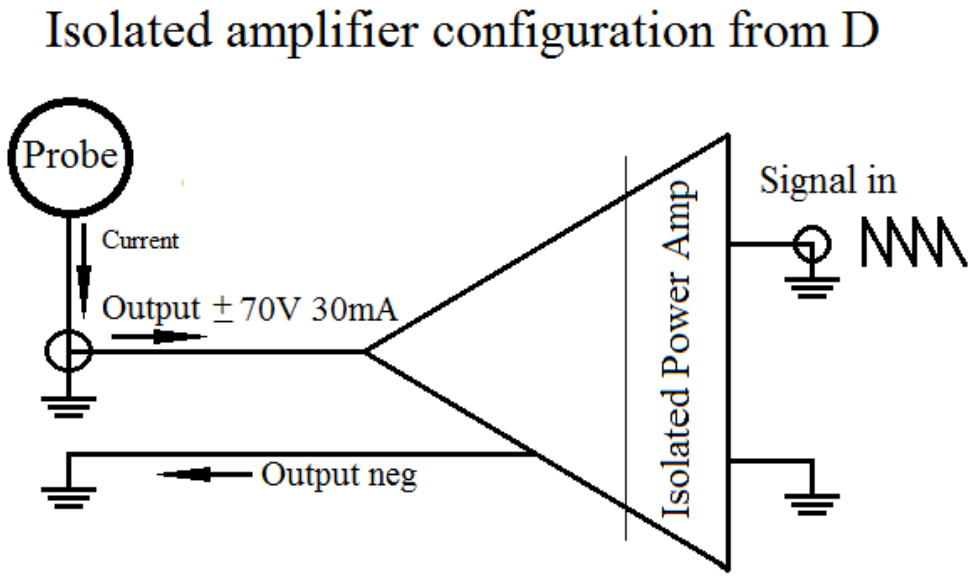

Figure 4.3: Output to discriminator.

is then sent to the same connector block and computer as D where the signal is digitalized with a 16-bit DAQ from National Instruments and stored together with the bias voltage to a file created by the software LabVIEW. Depending on how much current which is collected at C, the exchangeable resistor is chosen either at $33.6k\Omega$ or $100k\Omega$.

For the set-up of an experiment, nearly all parameter values for the entire system can be chosen through the computer and a LabVIEW program specifically written for Njord by the staff of the Aurora Lab at the University of Tromsø. From here the electrical step motor can position the probe at different radial positions, where it starts at $0mm$ (near the inner wall of the dome) and moves up to $240mm$ inwards (center of Njord at approx. $180cm$) at size-lengths as small as $1mm$. The program can also set up the probe bias sweep range, where $\pm$70V is the maximum. The number of ramp-steps for the voltage-sweep range can be set up above 1000 steps, and the number of samples pr. bias step for averaging can also be set to

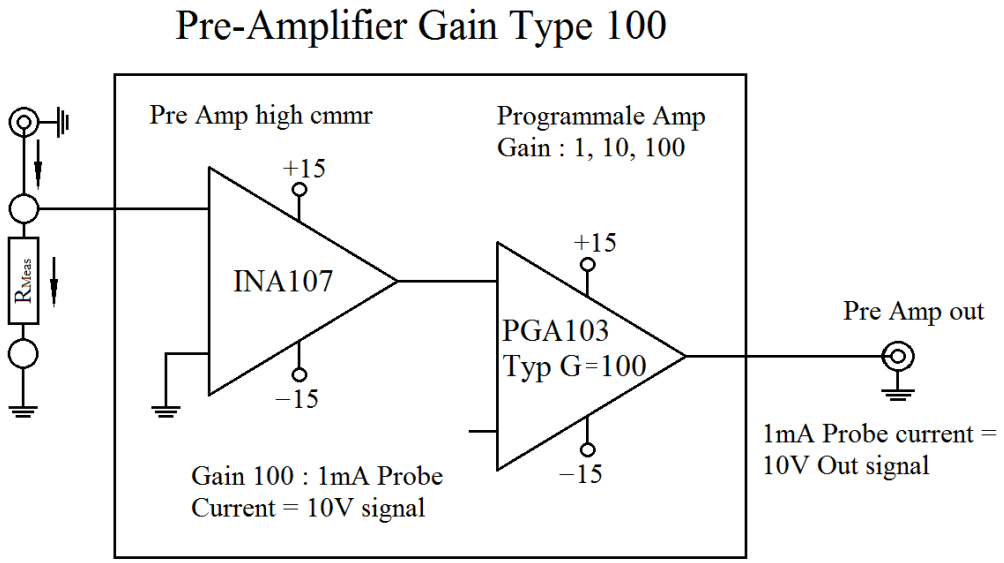

Figure 4.4: Signal amplifier from the collector.

above 1000 in order to reduce noise. The set-up for all parameters for the experiments is listed in Fig. 4.2.

Table 4.1: Set-up for the experiments.

RFEA grid configuration	Flow control	Probe settings
R_1 : 80 V	Q: [2.0 - 4.0] SCCM	Movement : 200mm
R_2 : 30 V	P_{Cap}: $[0.65 - 1.05]$ μBar	Step size : 10mm
D: 45 V	P_{WR}: $[4.7 - 10] * 10^{-4}$ mBar	Ramp steps : 300
C: 27 V		Means : 200
Sweep range : $\pm$60 V		
R_{amp}: $36.10k\Omega$		

The RFEA grid configuration and the probe settings was kept at the same values throughout all the experiments except for the settings of the flow control due to pressure testing. The pressure P_{Cap} from the Baratron gauge and the P_{WR} Boc-Edwards WR gauge was monitored for the pressure

tests, but is more suited for P_{Cap}-readings. The gauge is very sensitive, and can often view different pressure values throughout an experiment even if the flow is constant. However, they are usually monitored at $P_{Cap} = 0.65\mu$ Bar at flow $Q = 2.0$ SCCM, $P_{Cap} = [0.82 - 0.85]$ μBar at $Q = 3.0$ SCCM and $P_{Cap} = [1.0 - 1.05]$ μBar at $Q = 4.0$ SCCM, and is considered as the standard pressures for each flow value. Experiments involving center scans is done by shutting down the step-motor when the RFEA is centered, which is set at Movement 180mm on the LabVIEW-program. Also, the power of the RF-waves and the forward power P_{In}, the reflected power P_{Ref} and the VSWR was recorded by a software which is integrated to the RF-generator from a computer. The RF-power was tuned by the tuning system on the antenna in order to keep reflected power at a minimum (line match). The list for all of the recorded RF-power data is found in Appendix D.

4.3 IV-charts and data extraction

The distribution of a species of particles f_s can be described by the position $\mathbf{x}$, its velocity $\mathbf{v}$ and its time dependence t, which can be formed as a velocity distribution function $f_s(\mathbf{x}, \mathbf{v}, t)$. By integrating the function of a phase space $d\mathbf{x}d\mathbf{v}$ the number of particles N_s can be found, but it is more convenient to derive the density function using the distribution function

$$n_s = \int_v f_s(\mathbf{x}, \mathbf{v}) d\mathbf{v} \tag{4.1}$$

which also defines the zeroth-order velocity moment of the distribution. The distribution is assumed to be in a steady-state, rendering it independent of time t. If the plasma species were in thermal equilibrium and particle species in all velocities were travelling in only one direction, the distribution function would take form of a Maxwellian distribution. How-

ever this is not always the case in an experimental plasma, as indicated in Fig. 4.5 and Fig. 4.7.

A way of obtaining the distribution function is by using the current which is collected at the front of the aperture [19,29]. This can be done by multiplying Eq.(4.1) with the charge of ions e, velocity v and a constant A which is dependent on the front-plate aperture and define the collected current I_c as a function of the bias potential V_B of the discriminator

$$Aevn_i = I_c(v) = Ae \int v f_i(v) dv \tag{4.2}$$

By considering the direction of the velocity towards the probe, the minimal velocity v_{min} which is required in order to pass the bias potential can be estimated to

$$I_c(v_{min}) = Ae \int_{v_{min}}^{\infty} v f_i(v) dv \tag{4.3}$$

Using energy conservation, the minimum velocity can be estimated by setting the kinetic energy E_k equal to the energy of the probe bias potential

$$E_k = \frac{1}{2} m_i v_{min}^2 = eV_B \tag{4.4}$$

which gives

$$v_{min} = \Big(\frac{2eV_B}{m_i}\Big)^{\frac{1}{2}} \tag{4.5}$$

where m_i is ion mass and e is the elemental charge. Substituting this into Eq.(4.3) gives

$$I_c(\Big(\frac{2eV_B}{m_i}\Big)^{\frac{1}{2}}) = \frac{Ae^2}{m_i} \int_{V_B}^{\infty} f(\Big[\frac{2eV_B}{m_i}\Big]^{\frac{1}{2}}) dV \tag{4.6}$$

where $edV_B = m_i v dv$. By assuming that f is solvable and there exist a solution F for the integral, then Eq.(4.6) can be written as

$$I_c(V_B) = \frac{Ae^2}{m_i}\int_{V_B}^{\infty} f(\left[\frac{2eV_B}{m_i}\right]^{\frac{1}{2}})dV = \frac{Ae^2}{m_i}\left[F(\infty) - F(\left[\frac{2eV_B}{m_i}\right]^{\frac{1}{2}})\right] \quad (4.7)$$

In order for a solution to exist, it is assumed that $F(\infty) \to 0$ such that Eq.(4.7) can be differentiated with regards to V_B, giving

$$\frac{dI_c(V_B)}{dV_B} = \frac{Ae^2}{m_i} f(\left[\frac{2eV_B}{m_i}\right]^{\frac{1}{2}}) \quad (4.8)$$

which can be solved for the distribution function with the use of the bias potential

$$f(v) = \frac{m_i}{Ae^2}\frac{dI_c(V_B)}{dV_B} \quad (4.9)$$

Using these results derived from the density function, the distribution function can be found by differentiating the ion current which enters the RFEA with respect to its bias potential. Using this both the ion density n_i and the plasma potential V_P can be estimated. They can usually be estimated easily through the plot of both the ion current and the distribution with respect to the bias potential in an IV-plot as depicted in Fig.4.5.

This is one of the results from a scan done inside the Njord chamber by the RFEA, and shows how the ion current develops at the collector as the discriminator sweeps from a negative potential towards a large one (IV-chart) and the distribution function from the derivative of the current (dIV-chart). Usually, I_i is shown as a positive current in most studies, but the probe reading program which analyzes the data is programmed to show the current that goes in the RFEA as a negative one in order to directly obtain a positive distribution function. A quick way of estimating V_P is to find where IV-plot has the steepest gradient, usually done by finding the position of the maximum point on the dIV-plot on V_B. A quick estimate of the density can be obtained in two ways. By using Eq.(4.1), the density

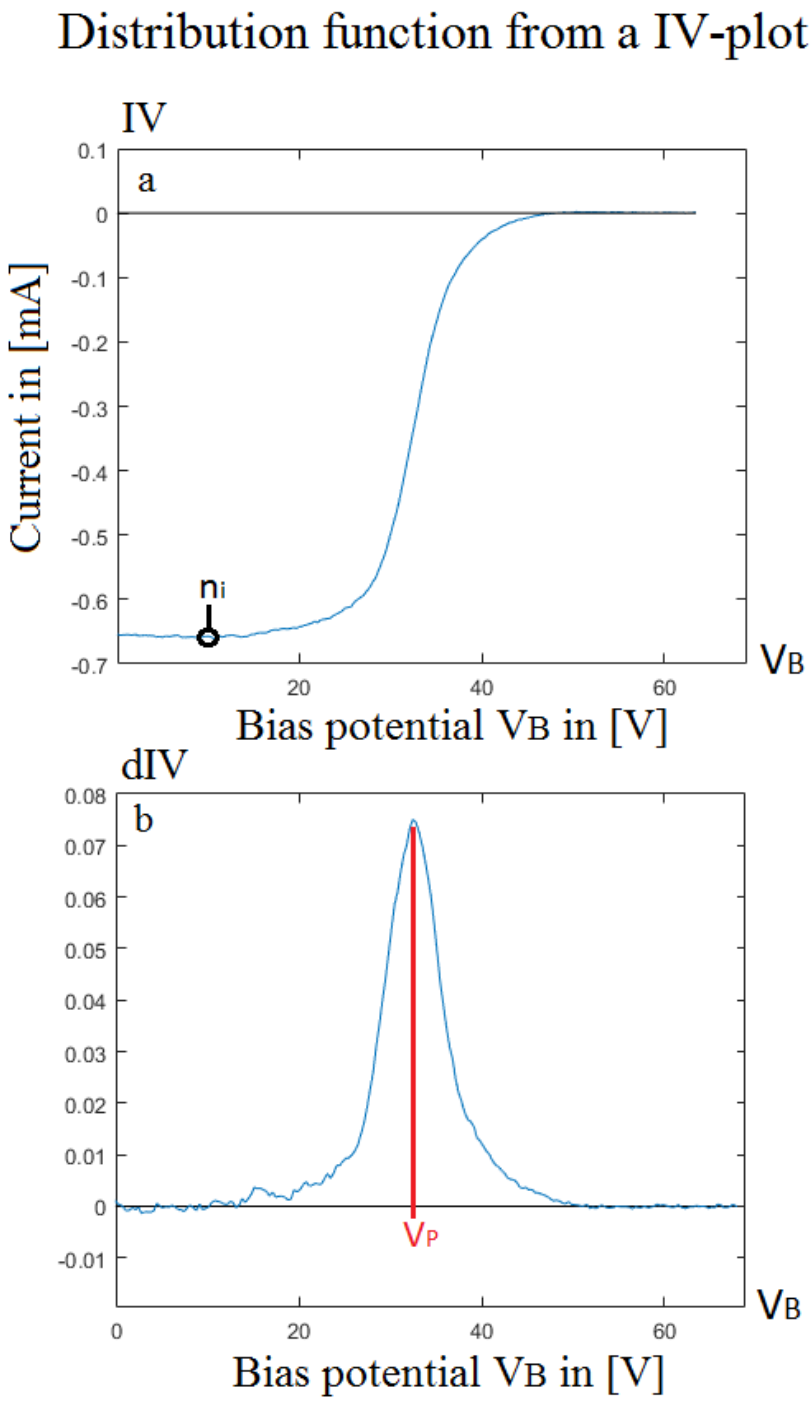

Figure 4.5: Plot of $I_i(V_B)$ (a) and the distribution function derived from it (b).

can be found by integrating dIV with respect to V_B which will give the area beneath the graph, or one can read directly on the IV-curve where the current is constant,ie the ion saturation current, which is found where V_B is negatively biased with respect to V_P. This is not always possible, as noise or probe effects at low V_B-values can make the signal too noisy to give a quick estimate of the density. Figure(4.6) is one such example where the noise is to large in order to give a direct reading. This is one reason why it is usually best to differentiate the curve with respect to V_B and integrate in order to find the area under the curve.

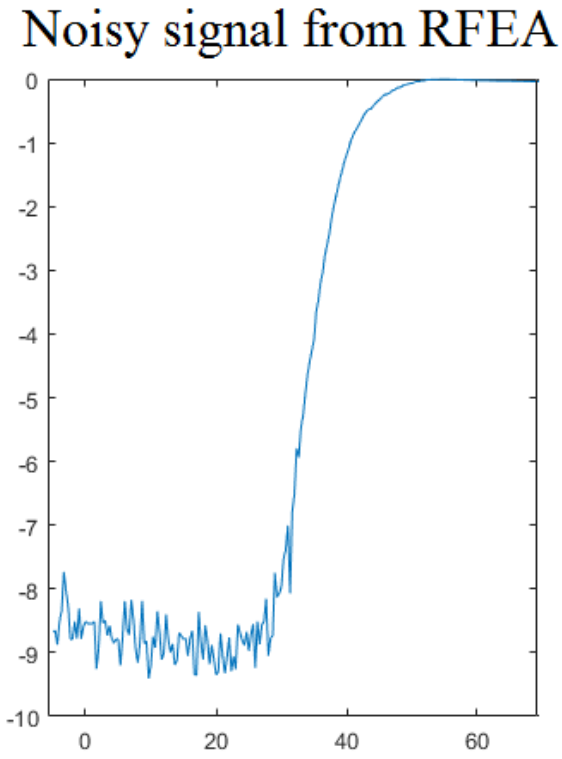

Figure 4.6: Plot of $I_i(V_B)$ and noise in front of V_P.

If the ion temperature T_i were wished to be obtained, one could fit the dIV-curve into a Maxwellian velocity distribution

$$f(v) = A \ \exp\left(\frac{m_i v^2}{2k_B T_i}\right) \tag{4.10}$$

which the dIV-plot in Fig. 4.5 resembles. Inserting this into Eq.(4.9) and manipulate it with the natural logarithm in order to find an expression for T_i gives

$$T_i = \frac{e}{k_B} \log \left(\frac{dI(V_B)}{dV_B} \right)^{-1} \tag{4.11}$$

However, as mentioned before this will not be valid in most data acquired by the RFEA due to the energy resolution for the probe. Since a build-up of space charges within the probe can alter the directions of ions the dimensions of the probe must be adjusted in order to resolve the ion energies [37]. Usually the distance between the grids, especially between the discriminator and the repellers, bust be set at approximately 4 Debye lengths λ_D [30], which can be achieved by using an aperture and grids with a reduced transparency in order to reduce the density inside the probe which increases λ_D [32]. The random ion-ion collisions which can change the trajectory of the ions at the collector is one simple factor where the energy recolution can be reduced [2]. The angle of incoming ions towards the collector of the probe also affects the energy resolution, as the efficient acceptance angle depends on if the ions reaches the collector. Using numerical particle-in-cell simulations has also shown that the acceptance ange contributes to a low energy tail [38], showing that a decreasing acceptance angle results in a decreasing low energy tail in the Ion Density Function (IDF). The distribution seems to be unaffected by the changes in the acceptance angle, although a change in aperture will affect the flow of ions entering the probe. The low energy tail can be explained by ions which enters the aperture at a large inclination angle, meaning that a significant part of the ion momentum is in the tangential component of the velocity. There is also the possibility of electrostatic lensing effects inside the probe due to the grids grids and the aperture [39] In the end the distribution distribution is too wide [], resulting in artificially high temperature estimates

from the distribution. The distributions in the sheath of the particle-in-cell simulations usually shows that the full-with-half-maximum (fwhm) drops first to about half of the original distribution before they slowly increase toward the probe. This slow increase in fwhm in the inner part of the sheath seems to depend on the total voltage across the sheath, indicating that there is some effect of weak electrostatic ion-ion collisions in the sheath altering the trajectory of the ions. Oscillations in a RF plasma can also affect the energy resolution. By defining the the energy broadening of the peak in the plasma in the form of the peak in the form of [40]

$$\Delta E = \frac{2eV_{RF}}{\sqrt{1 + (\frac{1}{2}\omega t_{av})^2}} \tag{4.12}$$

where V_{RF} is the RF-amplitude, ω is the angular RF-frequency and t_{av} is the average time an ion takes to fall through the sheath, defined as

$$t_{av} \approx \frac{1.2}{\omega_{pi}} \Big(\frac{2eV_{Sheath}}{K_B T_e} \Big)^{-\frac{1}{4}} \tag{4.13}$$

where ω_{pi} is the ion plasma frequency and V_{Sheath} is the sheath potential. Using data parameters from Njord from earlier results ($\omega_{pi} = 3.6{*}10^7 rad/s$, $V_{Sheath} = 45V$, $K_B T_e = 6eV$) the average flight time through the sheath is equated at $t_{av} = 6.5 * 10^{-8} s$. Combining this with the 13.56MHz RF-frequency ($\omega = 85.2 * 10^6 rad/s$) gives an energy broadening of

$$\frac{\Delta E}{2eV_{RF}} = 0.34$$

This means that the RF-broadening will be at 34% of the RF-peak-to-peak voltage.

These are some of the different factors which reduces the energy resolution for an RFEA probe, making it too inaccurate to fit any Maxwellian distribution for ion-temperature estimates.

If a beam formation is present, the distribution function will look something like the dIV-curve in Fig. 4.7, and the Maxwellian velocity distribution would not be an accurate fit to the distribution.

As Fig. 4.7 shows, a different distribution function dIV with beam is given, showing the double-peak distribution which is the well known signature of a beam-formation in a plasma. The first peak at the lower V_B still represents V_P, while the second one represents the beam potential V_{Beam}. Using these two potentials, the kinetic beam energy E_{Beam} can be estimated by subtracting V_P from V_{Beam}. This can again be used in order to find the beam velocity using energy conservation

$$\begin{aligned} E_k = \frac{1}{2} m_i v^2 &= e(V_{Beam} - V_P) \\ V_{Beam} - V_P &= E_{Beam} \\ \rightarrow v &= \sqrt{\frac{2e}{m_i}(V_{Beam} - V_P)}, \end{aligned} \tag{4.14}$$

The ion beam density can be directly estimated at the $I_i(V_B)$ plot where the largest gradient starts to be reduced. Alternative, it can be measured by estimating the area beneath the secondary peak, marked as the gray area in Fig. 4.7, b.

4.3.1 Finding the density using MATLAB

Estimating the plasma density with MATLAB was done by using the data of the plasma distribution provided by the probe. The derivative of the distribution with respect to the bias potential was first found, and then the area beneath the graph was estimated. Before the area underneath the

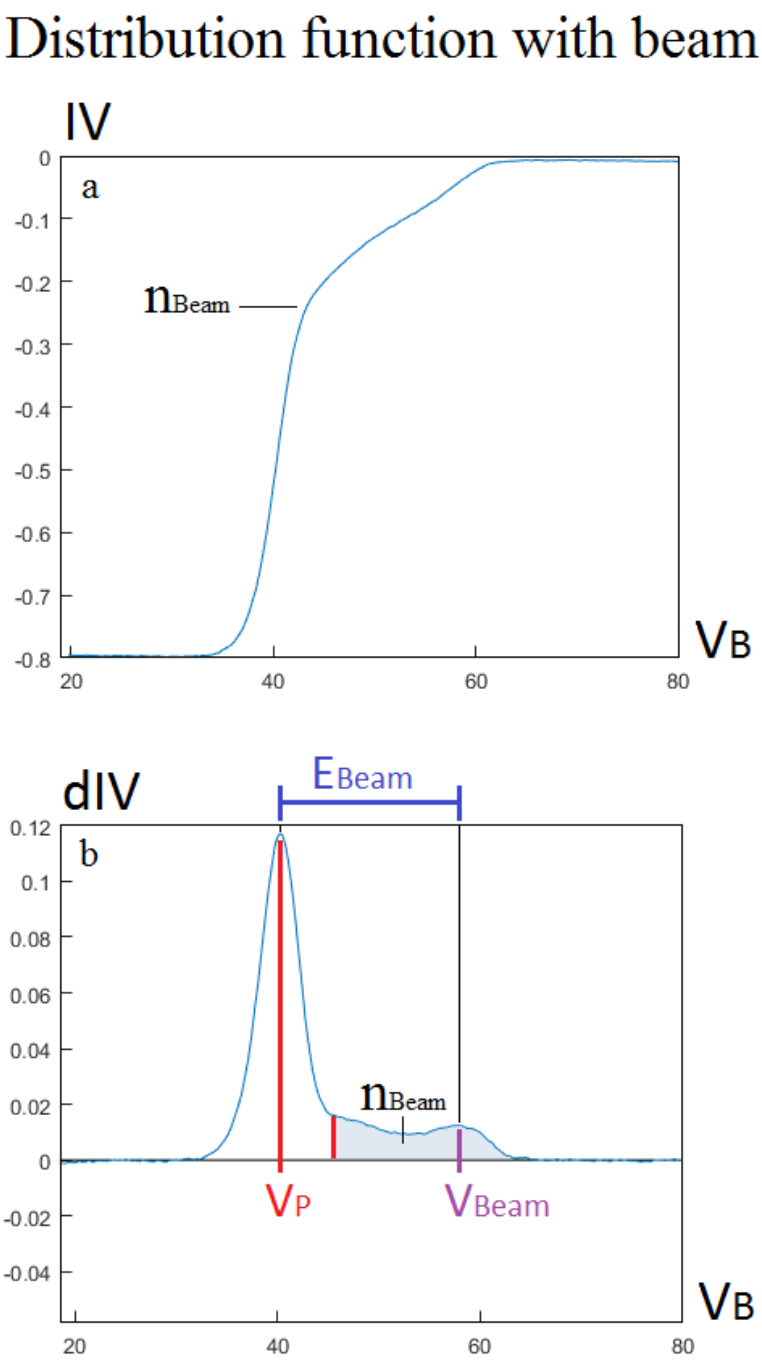

Figure 4.7: Plot of $I_i(V_B)$ (a) and the double-peak distribution function from its derivative (b).

derivative was found however, the derivative from the raw data needed to be smoothed due to noise in the signal. The noise comes from the build-up

of space charges between the grids which can distort the effective bias and reduce the energy resolution. The noise was smoothed out by applying a Savitzky-Golay filter with the MATLAB function sgolayfilt(X,Y,d). The filter works by fitting individual sub-sets of adjacent data points with a low-degree polynomial with the linear Least Squares Method (LSM). The function sgolayfilt(X,Y,d) smooths the data Y out on X with a filter size d, where d must be odd and larger than the polynomial size. Figure(4.8) shows an example of a differentiated raw data (blue line) compared to the filtered one (orange) with a filter size of $d = 9$, which gave good smoothing for nearly all the data with some exceptions.

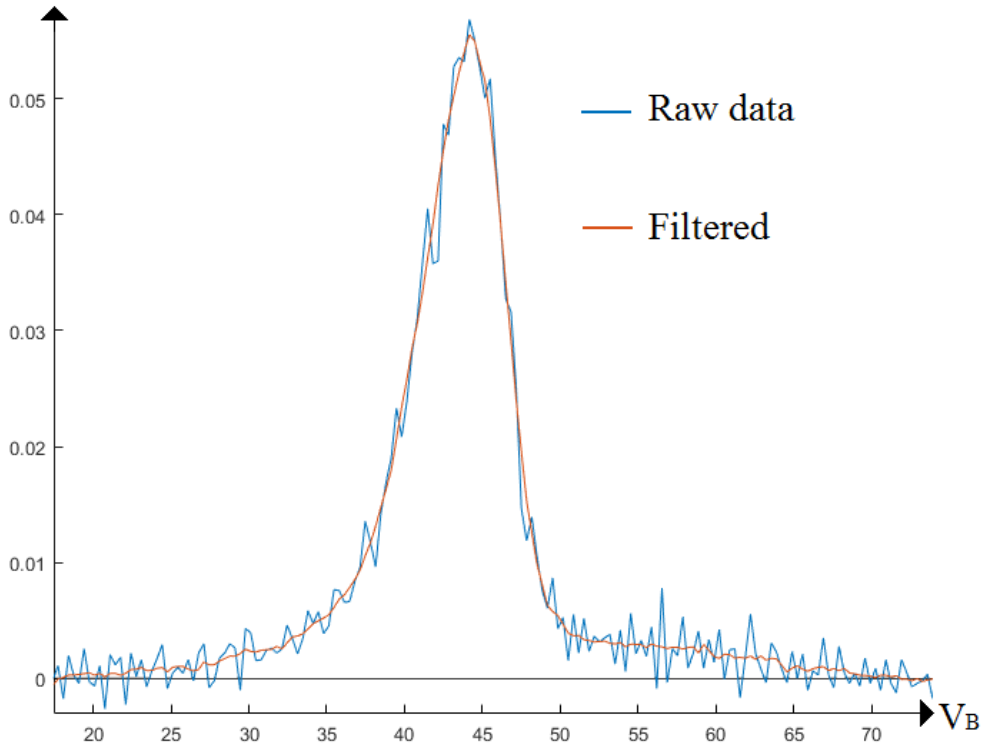

Figure 4.8: Filtering of a set of derived data at RF power P_{in} : $400W$, gas flow Q : 2 SCCM and magnetic coil current I_{Coils} : $5A$ with filter size 9.

The area under the smoothed graph was estimated using the built-in function trapz, short for Trapezoidal Numerical Integration (TNI). The

function trapz(X,Y) integrates a set of data Y with spacing increments X numerically using the Trapezoidal method, or the Trapezoidal rule, which approximates a region under the graph of a function by breaking the area down into trapezoids. If the integration is evenly spaced with $N+1$ points the TNI approximates the integral to :

$$\int_a^b f(x)dx = \frac{b-a}{2N}\sum_{n=1}^{N}\left[f(x_n)+f(x_{n+1}\right]$$

Due to the set-up of the RFEA program on Njord and its measurement of the current, the integration had to be restricted to the positive area of the differentiated distribution. The negative valued parts which is due to the noise can affect the overall area, and will also add the area underneath Y=0 which is undesirable. In order to get around this, the data Y on the bias X had to be restricted to the points a and b where the differentiated distribution is defined in the form of trapz(X(a:b),Y(a:b)). Figure(4.9) gives a simple view of how the function with its restriction works.

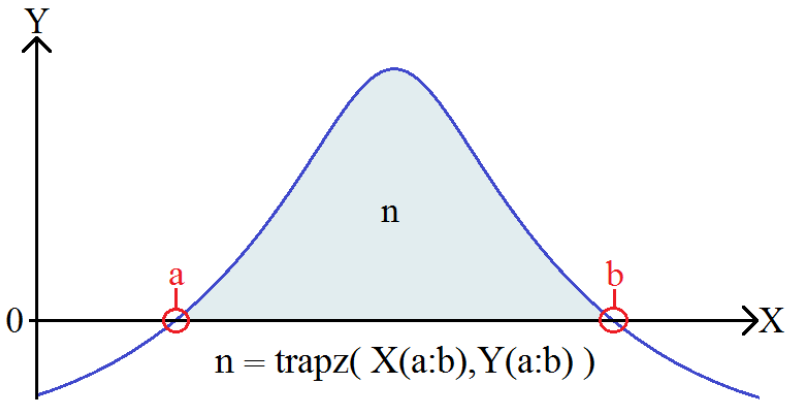

Figure 4.9: The function of MATLAB's trapz function with its restrictions.

This concludes all the data extraction tools which will be used to analyze the data which will be provided from experimentations on the Njord device in order to find the effect a magnetic multipole confinement has on the plasma.

Chapter 5

Experimental results

The effects that the permanent magnets on the magnet band had on the plasma and its characteristics was found by performing experiments on the plasma with the RFEA probe and the data extraction methods described in Section 4.3. By investigating the change in the plasma characteristics and profiles one can get a clear overview of how the magnetic cusps affected the plasma. The parametric scans were carried out with variations in RF-power, gas pressures and source magnetic field strength, with and without the magnet band. From the data provided from these scans, the plasma potential V_P and the ion density n_i and beam energy E_{Beam} were estimated.

Due to the nature of experimental testing and data extraction, uncertainties or systematic errors can occur, which in turn can affect the results. This can come from human errors, wrong set-up and/or defect equipment. There is also the risk of misreading and calculation errors and/or badly performed operations. If the data which is analyzed is inaccurate or very noisy, the data must either be manually adjusted for systematic errors. filtered for noise reduction or discarded.

The results will be shown in plots which will give an indication of how

the magnetic cusps at the source wall will affect the overall plasma characteristics. For all figures, tables and lists, all scans and profiles with the magnet band on will be marked as "With MagCusp".

5.1 Plasma potential results

5.1.1 RF-power variation

The plasma potential V_P was obtained with the method described in Section 4.3 using MATLAB. The first scans involves the RF-power in the range $[100-800]$W. The results are shown in Fig. 5.1. A list of the values can be found in List A.1 and A.2 in Appendix A. The list of forward and reflected power is listed in Table D.1.

As shown, there is not much difference in the center of Njord at the different RF-powers, so the magnet band seems to affect V_P and the center characteristics very little. Scans of radial profiles however have a more noticeable difference, as shown in Fig. 5.2. The radial center of Njord is positioned at the radial position $r = 180$ cm for all plots from here on.

Here, the effect from the magnetic band is more noticeable for the V_P profile. With the magnetic band on, V_P falls off more rapidly over the radii towards the edge of the source. A decrease in V_P can can indicate some changes in the characteristics of the plasma depending on the plasma parameters, which will be discussed later in the estimation of the ion density

5.1.2 Pressure variation

The V_P characteristics at different pressures with and without the magnet band was done by setting the flow to values Q = 2 SCCM (0.65 μBar), Q = 3 SCCM (0.85 μBar) and Q = 4 SCCM (1.05 μBar). The flow is not increased any further since beam formations are difficult to spot at higher

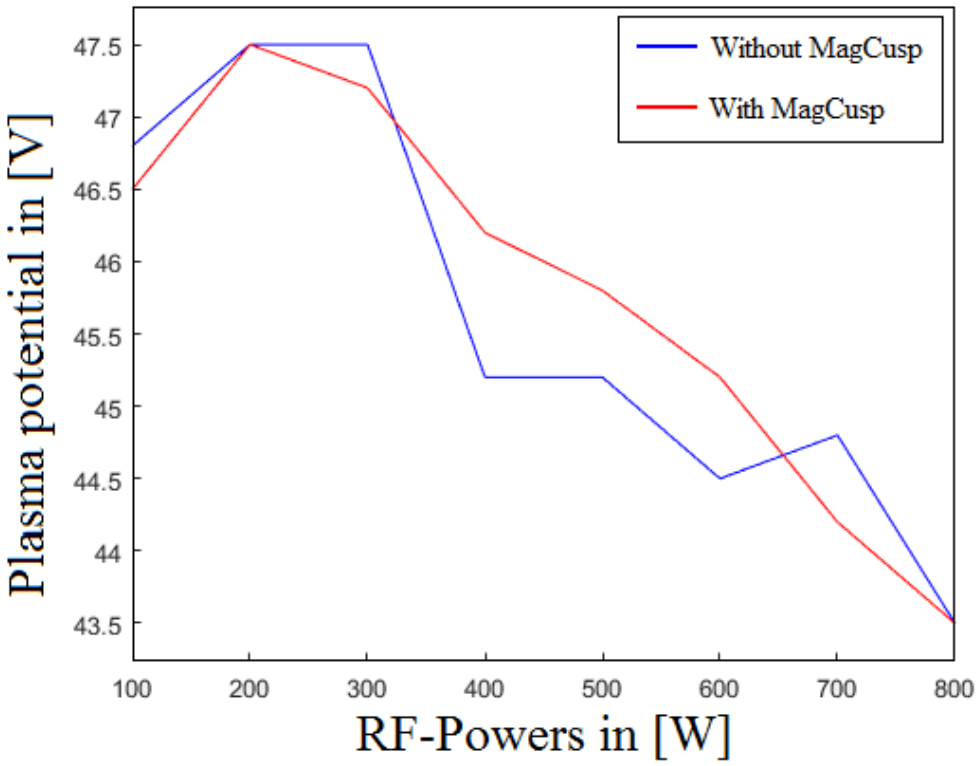

Figure 5.1: Center plasma potential V_P as a function of RF-power at pressure P_{cap} : 0.65μ Bar (Flow $Q = 2$ SCCM), magnetic coil current $I_{Coils} = 5$ A and with and without magnet band.

pressure values. The forward and reflected power data can be found in Table D.2.

Similar to the results for the RF-powers, the difference in V_P with and without the magnet band is minor, and from the plot fairly constant along the change in pressure. This is to be expected, as more argon gas enters the chamber as the pressure rises, meaning that the density is increasing, causing V_P to drop. The same results were found in the radial profiles of V_P versus pressure with the same parameters, which is depicted in Fig. 5.4.

Similarly to the RF-power case, the difference in V_P with and without the magnet band is more noticeable at the edge of the plasma. Again this

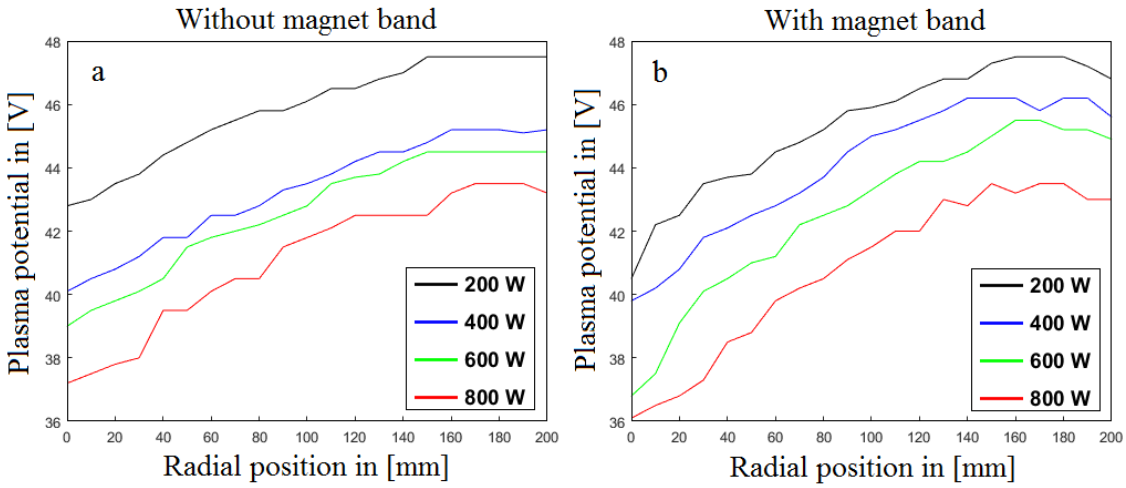

Figure 5.2: Radial plasma potential V_P RF-power profiles at pressure P_{cap} : 0.65μ Bar (Flow Q = 2 SCCM) and magnetic coil current I_{Coils} = 5 A, without (a) and with (b) magnet band.

will indicate a change in plasma characteristics, which will be discussed later with the ion density results.

5.1.3 Magnetic field variation

Finding how the axial magnetic field strength affects the plasma potential was done by adjusting the magnetic coil current I_{Coils} with a current range of $[0-6]$ A. The magnetic field strength dependency of I_{Coils} was depicted in Fig. 2.4. The results are shown in Fig. 5.5, and the forward and reflected power data is found in Table D.4.

As the figure shows, the V_p characteristics have a big dip at the lower magnetic fields. It also shows that V_P is larger at I_{Coils} = 1 A and 2 A with the magnet band, which is the opposite of the results so far. It is clear that there is a change in the plasma mode at these low-magnetic fields, which makes V_P drop by over $10V$. This will be discussed in more detail later in Section 5.2.3. The radial profile scans at the different I_{Coils} - values show

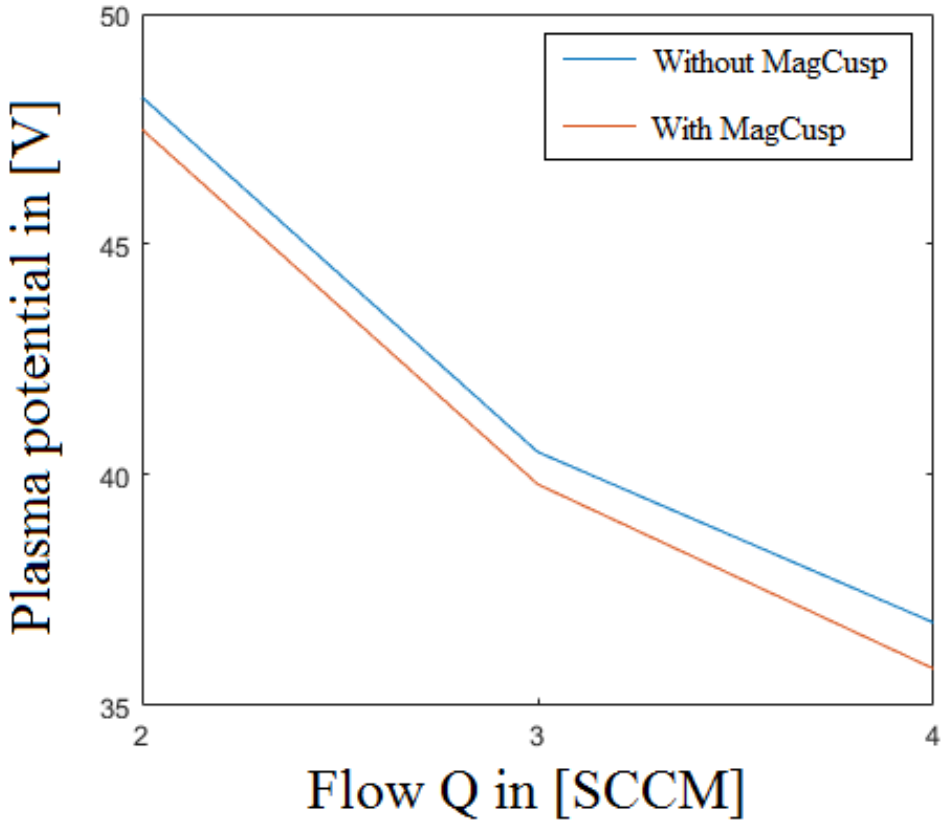

Figure 5.3: Center plasma potential V_P versus pressure at RF-power = 400 W and $I_{Coils} = 5$ A.

similar results as earlier, showed in Fig. 5.6.

As shown, V_P is lower when the plasma is not under any influence of an axial magnetic field compared to with one. Also, the difference with and without the magnet band at the plasma edge is smaller without any axial magnetic field, suggesting that the coil current affects the V_P characteristics noticeably more than the magnet band. There were not performed any radial scans at the other I_{Coils} -values, but the radial profiles will most likely follow a similar pattern as the previous profiles did. Again, the drop in V_P will be discussed with the ion density results.

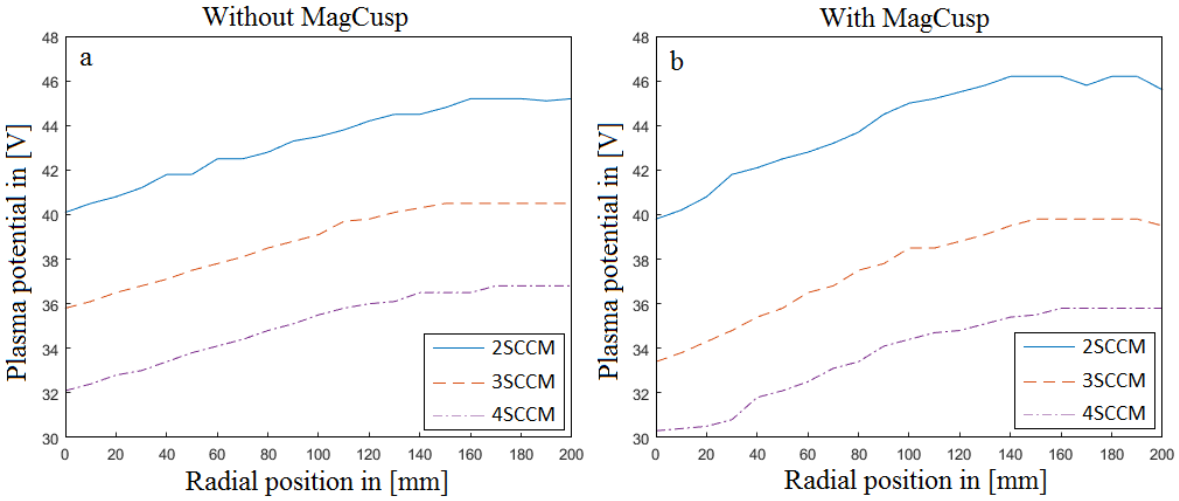

Figure 5.4: Radial plasma potential V_P profiles versus pressure at RF-power = 400W and magnetic coil current $I_{Coils} = 5$ A), without (a) and with (b) the magnet band.

5.2 Ion density results

5.2.1 RF-power variation

By using the method described in Section 4.3.1, the density at the center of the plasma was estimated as a function of RF-power. The first results are shown in Fig. 5.7.

Figure (5.7) shows how the effect of the band increases along with an increasing RF-power, nearly doubling the ion density after 600 W. This shows that the cusp field is capable of effectively confining ions. By doing radial scans of the plasma, the confinement of the entire radii is shown in Fig. 5.8.

As the plot shows, the overall density has increased in the entire radial region. This shows that the magnetic band has a large effect of the plasma confinement in a cylindrical plasma source. As one can see, the density in-

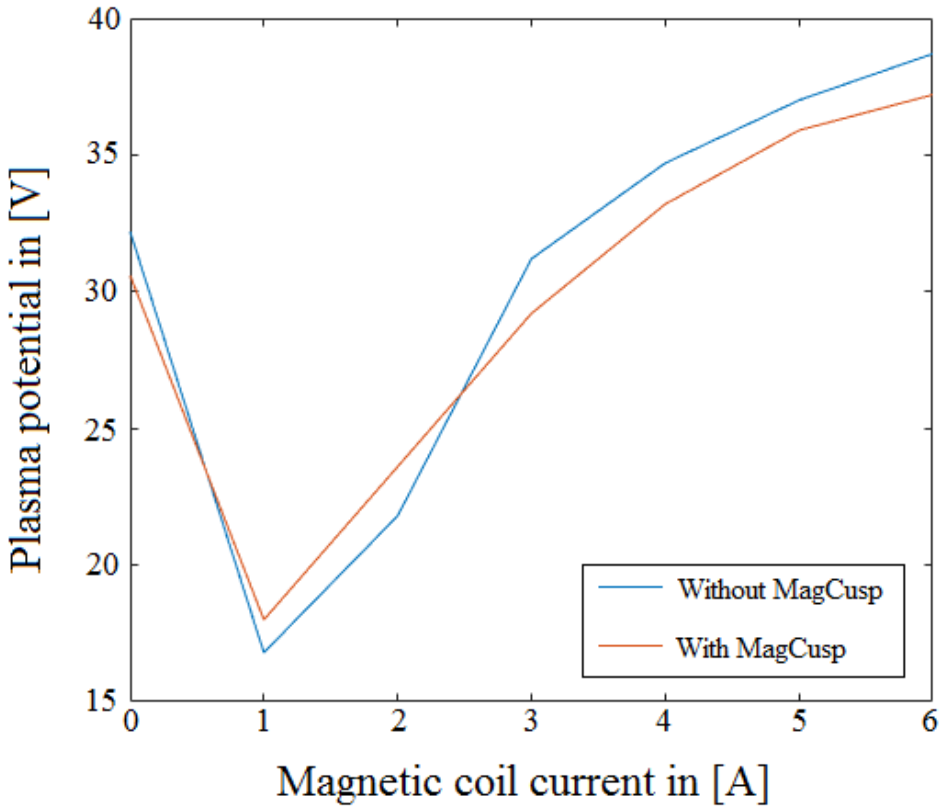

Figure 5.5: Center plasma potential V_P versus magnetic coil current at RF-power : 400 W at pressure $P_{Cap} = 0.85$ μBar (Flow Q = 3 SCCM) at position r = 180 cm.

creases towards a factor of two at higher RF-powers, which can either mean that more plasma is created due to higher RF-powers, or the confinement from the magnet band is more effective at these RF-powers. One way of estimating how much more effective the confinement is with he magnetic band, a ratio between the density with and without the magnet band can be estimated by introducing the density ratio n_r, defined as

$$n_r = \frac{\text{Plasma density with the magnetic band}}{\text{Plasma density without the magnetic band}} \tag{5.1}$$

The parameter n_r will tell how the confinement develops with different RF-powers, pressure and magnetic coil current I_{Coils}, and where the

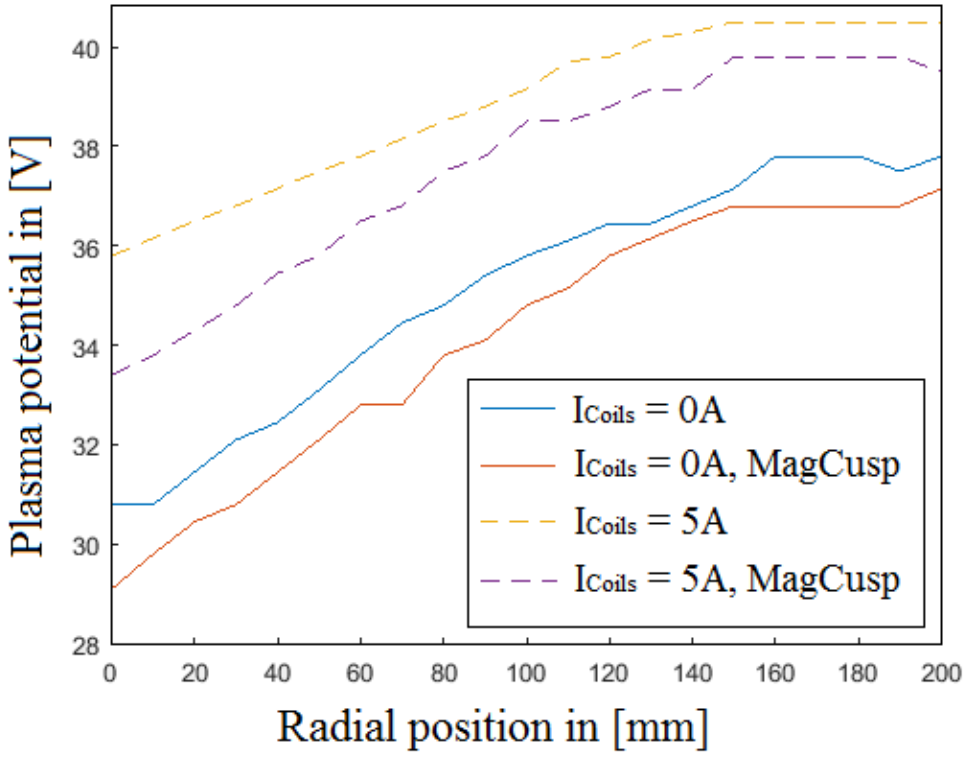

Figure 5.6: Radial plasma potential profiles V_P versus magnetic coil current at RF-power = 400 W, pressure $P_{Cap} = 0.85$ μBar (Flow Q = 3 SCCM), with and without the magnet band.

confinement improves. Using the definition, a set of radial n_r profiles at a RF-powe range of $[100 - 800]$ W are shown in Fig.5.9.

The parameter n_r, the relation will tell how more the confinement becomes at different RF-power profiles, as well as pressure and I_{Coils} profiles. The RF-power profiles are shown in Fig. 5.9, which comes from the same experiment for the V_P-profiles but with a RF-power range of $[100 - 800]$W.

As the profiles show, the magnet band doubled the plasma density at the center with the higher RF-powers, but does provide an increase at the plasma edge as well. The n_r profiles at 100W and 200W however shows that the density ratio at the edge of the plasma ($[0 - 10]$ mm) is slightly

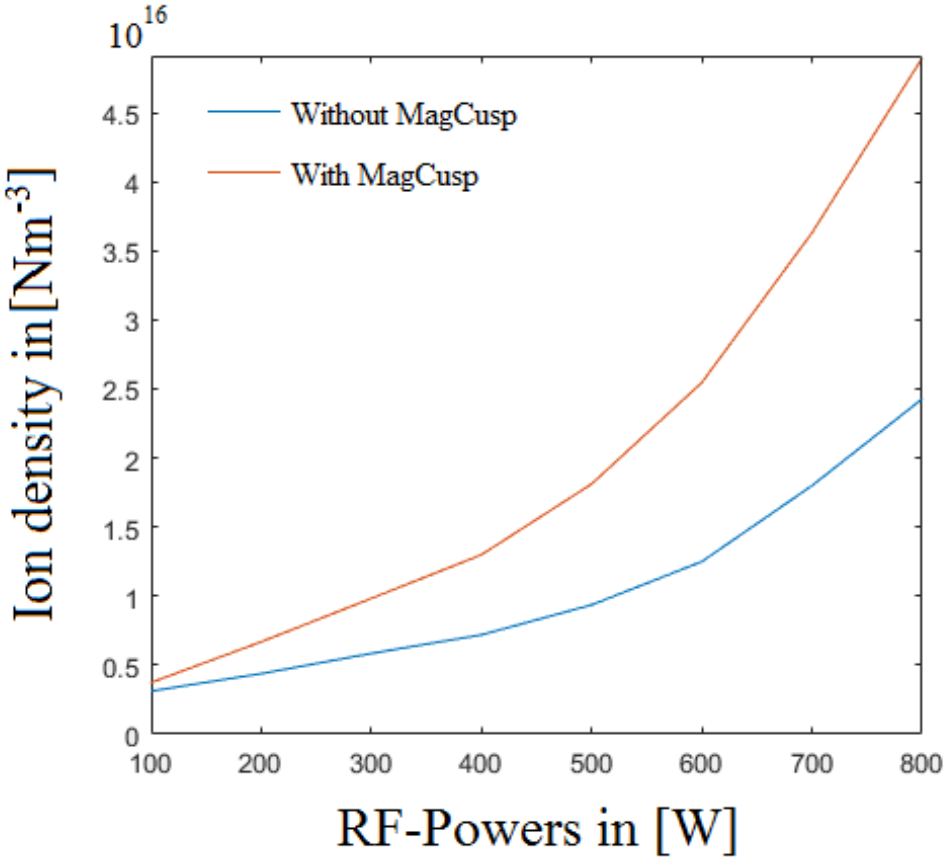

Figure 5.7: Center ion density n_i versus RF-power at pressure $P_{cap} = 0.65\mu$Bar (Flow Q = 2 SCCM) and magnetic coil current $I_{Coils} = 5A$ with and without magnetic band.

reduced, but this might be due to the low RF-power which creates very little plasma. It does seem that at the RF-power range of $[600 - 800]$ W, there is not much further increase in ion density, which suggests that the maximum effect of the magnetic band lies somewhere around 600 W as the ratio seems to converge around a factor of two.

5.2.2 Pressure variation

The variation in pressure will show how effective the magnet band manages to distribute the ions, both at the center at radially. Because the pressure

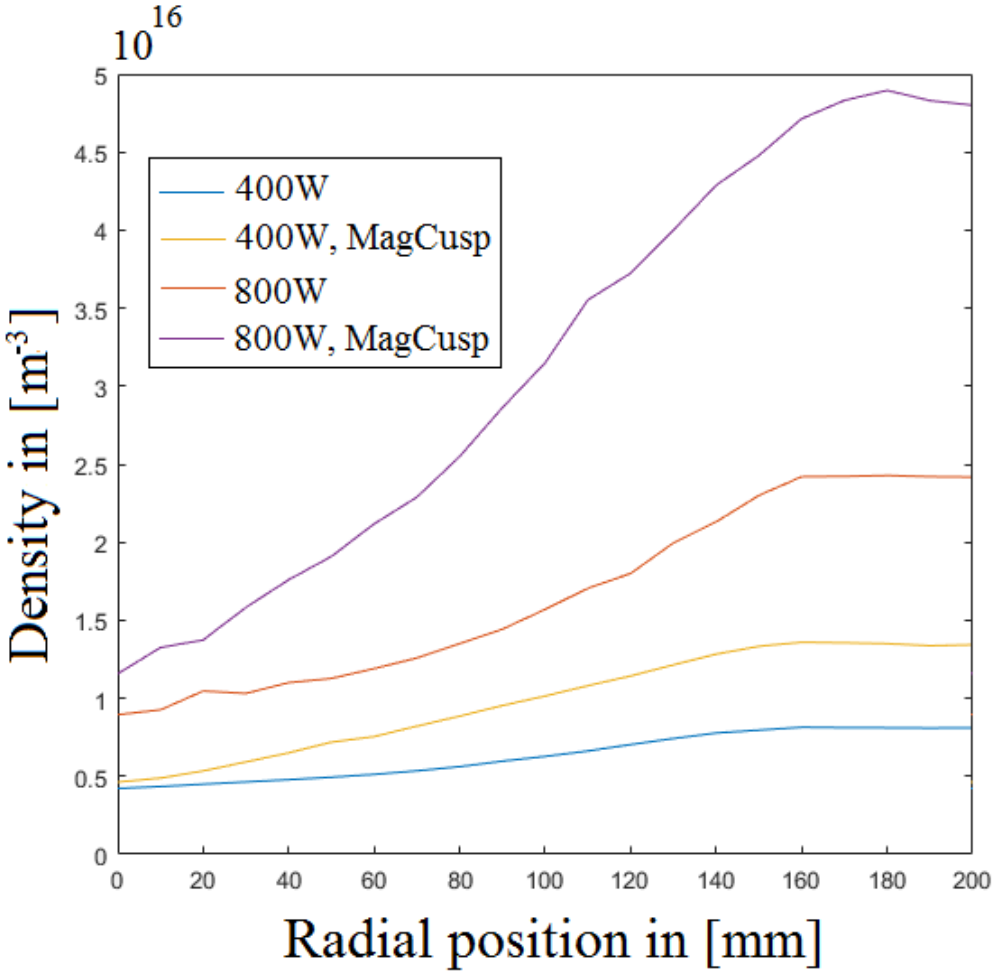

Figure 5.8: Radial ion density n_i profiles versus RF-power of 400 W and 800 W at pressure $P_{cap} = 0.65\mu$Bar (Flow $Q = 2$ SCCM) and magnetic coil current $I_{Coils} = 5A$, with and without magnetic band.

is determined by the amount of flow of argon gas which is put in the source chamber, it is reasonable to expect that the plasma density will increase at larger pressure values. This can be explained through the ideal gas law $PV = nR_sT$, where P is the pressure, V is the volume of the gas, n is the density, R_s is the specific ideal gas law and T is the temperature. Since V is equal to the volume of the source chamber, V is constant, and because the ionization is based on electron heating, the temperature of the ions changes very little. This means that an increase in P means that the

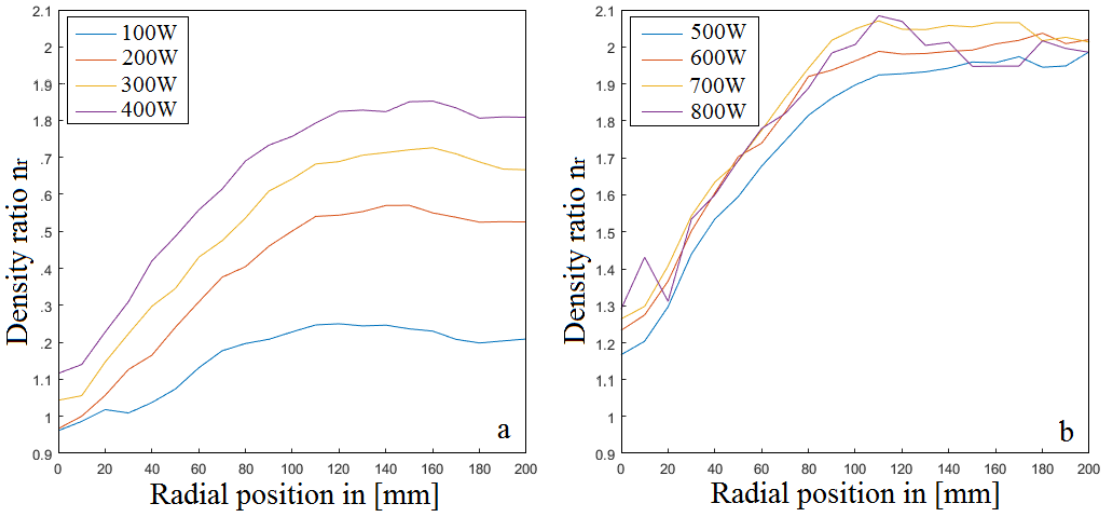

Figure 5.9: Radial density ratio n_r profiles versus RF-power at pressure $P_{cap} = 0.65\mu$Bar (Flow $Q = 2$ SCCM) and magnetic coil current $I_{Coils} = 5A$ at RF-power range $[100 - 400]$ W (a) and $[500 - 800]$ W (b).

density increases. From the pressure data for V_P, the ion densities are put at three different pressures determined by the flows Q = 2.0 SCCM (0.65 μBar), Q = 3.0 SCCM (0.85 μBar) and Q = 4.0 SCCM (1.05 μBar). The results from a scan at the flow range $Q = [2.0 - 4.0]$ SCCM is shown in Fig. 5.10, and the forward and reflected power data is found in Table D.2.

As shown, the cusp field from the magnet band causes the center ion density to increase by 66.5 % at Q = 2.0 SCCM, 88.6 % at 3 SCCM and 90.6 % at 4 SCCM. This is also with a magnetic coil current of $I_{Coils} = 5$ A, so the effect is most likely enhanced in the presence of an axial magnetic field. This is shown by examining the ion density ratio n_r at $I_{Coils} = 0$ A and $I_{Coils} = 5$ A at the same pressure range with the exception of flow $Q = 2$ SCCM at $I_{Coils} = 0$ A due to poor data quality. The results are shown in Fig. 5.11, and the forward and reflected power data is found in both Table D.2 and Table D.3.

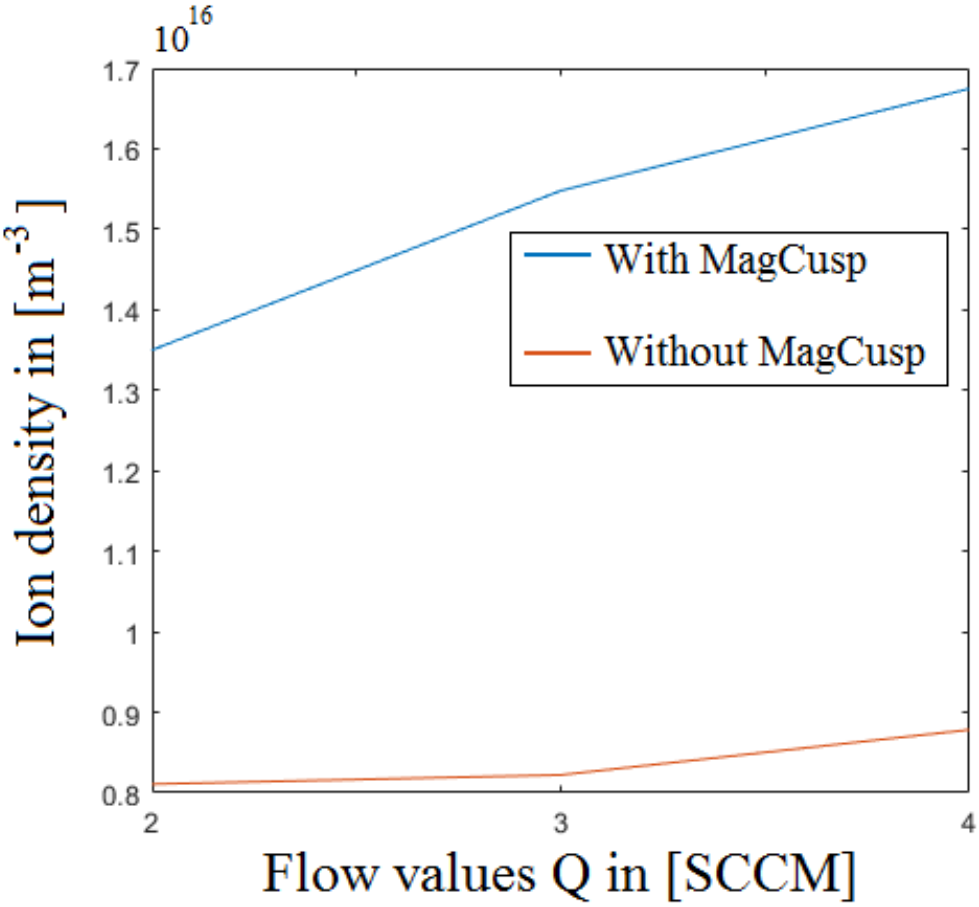

Figure 5.10: Center ion density n_i pressure variation at RF-power = 400 W, $I_{Coils} = 5$ A, with and without the magnetic band.

At $I_{Coils} = 5$ A the magnetic cusp fields from the magnet band improves the ion density at the center up to a factor of 1.9. At $I_{Coils} = 0$ A, there is very little difference between the flows 3 SCCM and 4 SCCM, with an approximate increase of the center ion density around 27 %, while at $I_{Coils} = 5$ A the density is increased by 90 %. This shows that the magnet band enhances the confinement with the influence of an axial magnetic field. Studying the radial pressure profiles, which is shown in Fig. 5.12, the increase of the edge of the plasma can be investigated.

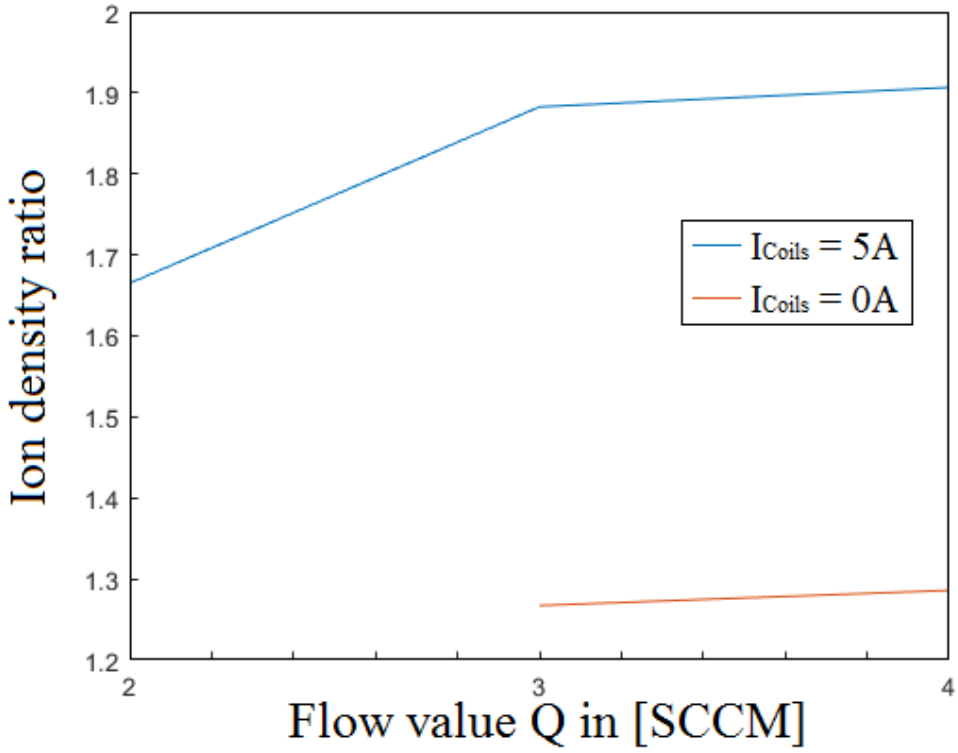

Figure 5.11: Center ion density ratio n_r versus pressure with RF-power = 400 W and magnetic coil currents $I_{Coils} = 0$ A and 5 A.

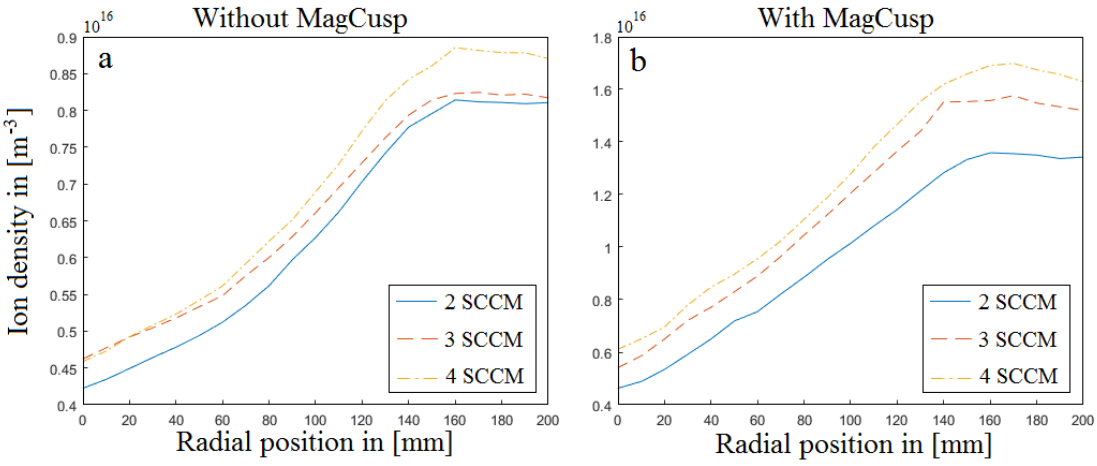

Figure 5.12: Radial ion density n_i profile versus pressure at RF-power = 400W, magnetic coil current I_{Coils} = 5 A, without (a) and with (b) the magnetic band.

The results shows that the ion density is increased by the edge of the chamber (r = 0 mm) by 9.6 % at Q = 2.0 SCCM, 17 % at 3.0 SCCM and 33.2 % at 4 SCCM with the magnetic band on. The overall effect shows that the magnetic band provides a noticeable difference in the ion density at the center, but less at the edge of the plasma. It also shows that the confinement becomes better at higher pressures throughout the entire radial range.

5.2.3 Magnetic field variation

As seen in the characteristics for the center V_P versus magnetic coil current, something changes in the plasma characteristics which causes it to sustain a new type of mode at a low axial magnetic field. Another way of investigate what happens in this regime is to estimate the ion density. The ion density in the center of Njord as a function of I_{Coils} is depicted in Fig. 5.13.

As the results show, a density peak is present at a low axial magnetic field, causing the characteristics of the plasma to change. This is somewhat unexpected, as one would rather expect that a stronger magnetic field would affect the trajectories of charges, causing an increasing number of particles to follow the field. From the other experiments with the magnet band, one would also assume that the magnet band would improve the magnetic confinement and hence increase the density with an increasing axial magnetic field. However, at this regime the density is lower with the magnet band on than off, causing a lower ion density at the center of Njord. One suggestion of this behaviour is a change in the helicon mode, causing a more effective ionization by transferring more energy to the electrons. This could be studied further by performing radial scans at this low magnetic field regime and see how the radial ion profiles behaves. Unfortunately, no such radial scans were performed at these low magnetic fields and thus this

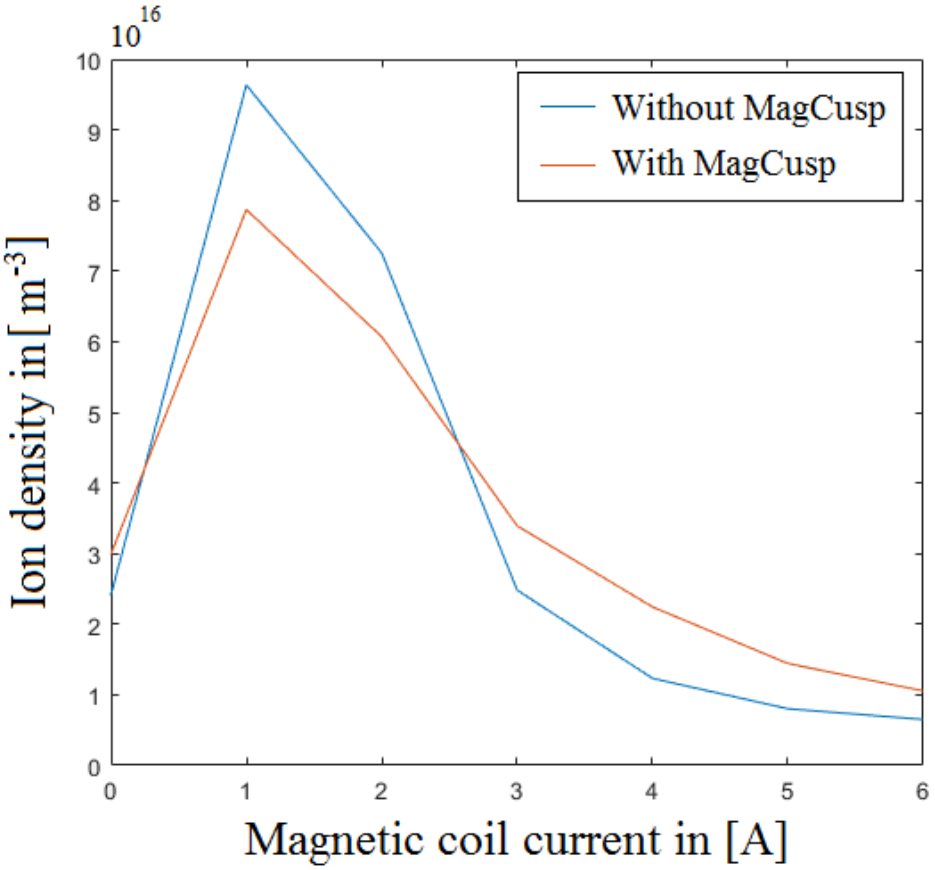

Figure 5.13: Center ion density n_i versus magnetic coil current I_{Coils} at RF-power = 400W and pressure $P_{Cap} = 0.85$ μBar (Flow $Q = 3$ SCCM), with and without magnetic band.

explanation can't be investigated further.

However, this low-magnetic field density peak has been noticed before. Studies of helicon plasma characteristics in a weak axial magnetic field has shown plasma density peaks which forms at field strengths below 100 Gauss [3], and in some cases the density is larger when there is no magnetic field affecting the plasma. The physical reasons why this phenomena occurs will be discussed in the next chapter. However, it is important to note that the magnetic band is changing the characteristics of the plasma at these low magnetic fields as well. This can be observed from the density ratio

n_r, shown in Fig. 5.14.

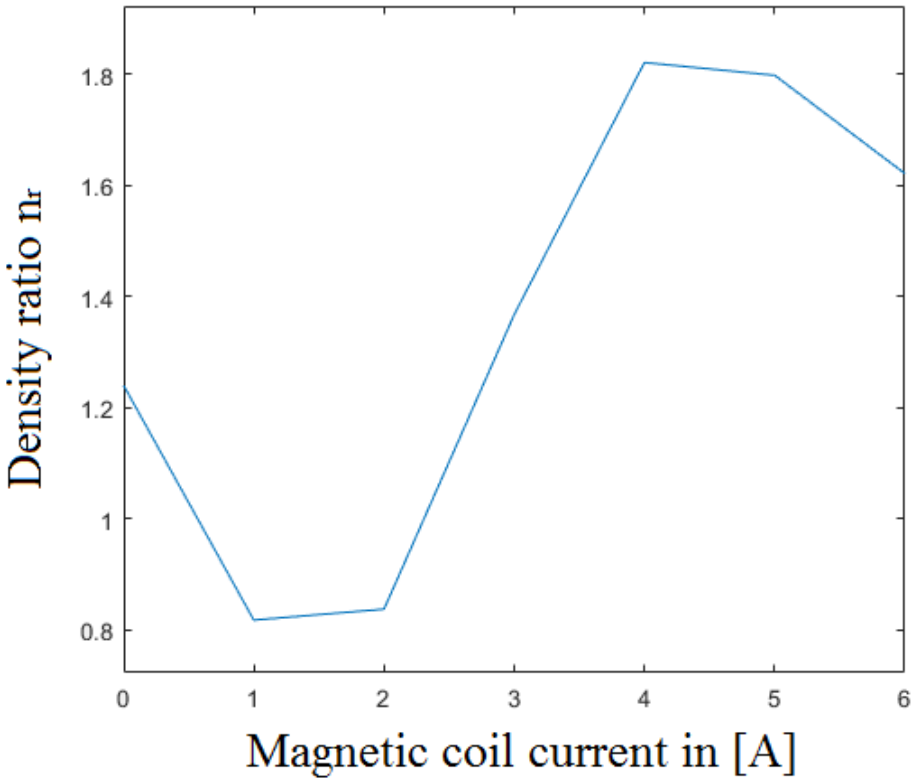

Figure 5.14: Center ion density ratio n_r versus magnetic coil current I_{Coils} at RF-power = 400W and pressure $P_{Cap} = 0.85$ μBar (Flow $Q = 3$ SCCM).

The plot shows that the magnetic cusp field is affecting the plasma density, resulting in a reduction of the overall density at $I_{Coils} = 1$ A at 35 Gauss with approximately 18% and $I_{Coils} = 2$ A at 67 Gauss with approximately 16 %. The density ratio also shows that the plasma characteristics changes somewhere between $I_{Coils} = 2$ A and 3 A, where the magnet band increases the density by approximately 80% at $[135 - 170]$ Gauss before it starts to decrease at the highest coil currents. This might be due to the same effects which causes the density peaks below 100 Gauss, but another explanation might be that as the axial magnetic field strength becomes much stronger, the contribution of the magnetic band becomes less impor-

tant. One can argue that a very strong magnetic field, far above what the Njord device is capable of, the contribution of the magnetic band becomes negligible, resulting in a density ratio of $n_r = 1$. However, this is not possible to explore any further with Njord.

5.3 Ion beam energy results

Exploring the effect the magnet band has on the ion beam energy E_{Beam} is important, as it can be converted to the beam velocity v_{Beam} using kinematic

$$eE_{Beam} = \frac{1}{2} m_i v_{Beam}^2 \tag{5.2}$$

which is useful in to study how the magnet band affects v_{Beam}.

At first, E_{Beam} at the center was investigated at the RF-power range $[100 - 800]$ W with and without the magnet band. The results are shown in Fig. 5.15, and a list of the results can be found in Table C.1.

The ion beam energy reduces with increasing RF-power, but not by a large amount. With the magnetic cusp, E_{Beam} drops approximately 15 %, while without it it drops 19 %, suggesting that E_{Beam} is reduced slightly less at increasing RF-powers with the magnetic band on. However, it is clear that the ion beam energy is larger without it, i.e. about 20 % higher. This is consistent with the results, as these set-ups has shown ion densities around twice as high with the magnetic band on, which corresponds to a lower plasma potential. The width of the beam is shown by the radial ion beam energy profiles, depicted in Fig. 5.16.

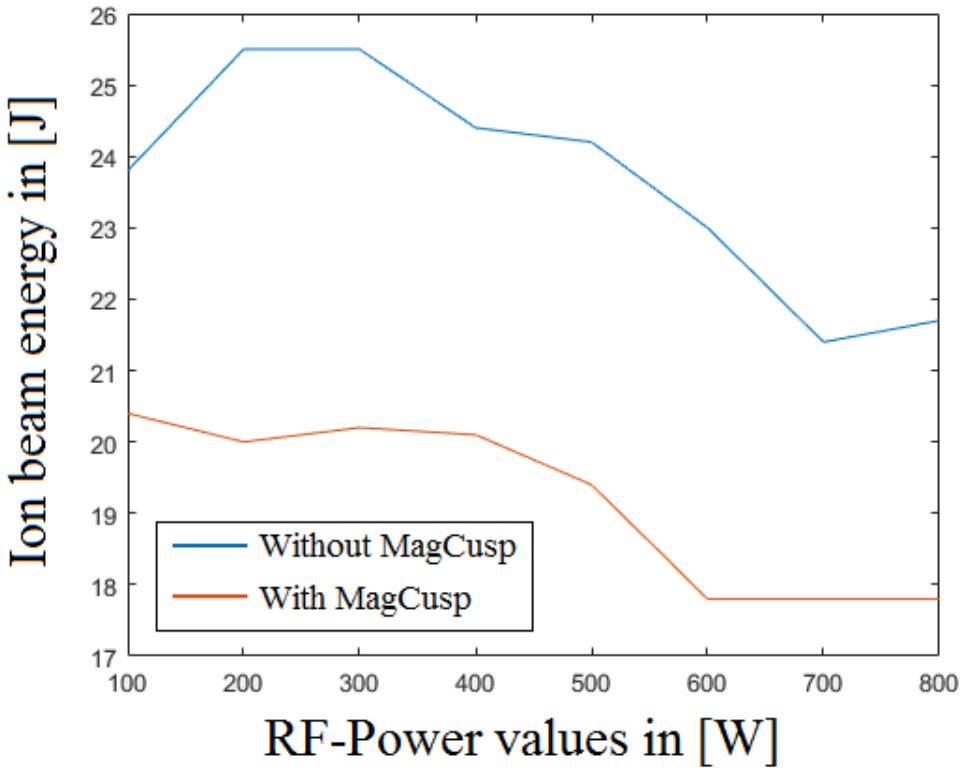

Figure 5.15: Center ion beam energy E_{Beam} versus RF-power at pressure $P_{Cap} = 0.65$ μBar (Flow $Q = 2$ SCCM) and the magnetic coil current $I_{Coils} = 5$ A.

The beam has a constant energy level in the radial direction, and it has a radius of 6 cm, which is within the inner radii of the source chamber. However, it seems like that this radius might increase with the magnet band on at a larger RF-power. This increase in width has been observed more than once during the analyzis of the data from the experiments on Njord, and this might be due to the increased ion density at the center which also distributes itself more radially out from the center.

The radial profiles of the beam energy shows a similar behaviour with changes in the pressure as the RF-power, as shown in Fig. 5.17, and the data for these profiles are listed in Table C.3.

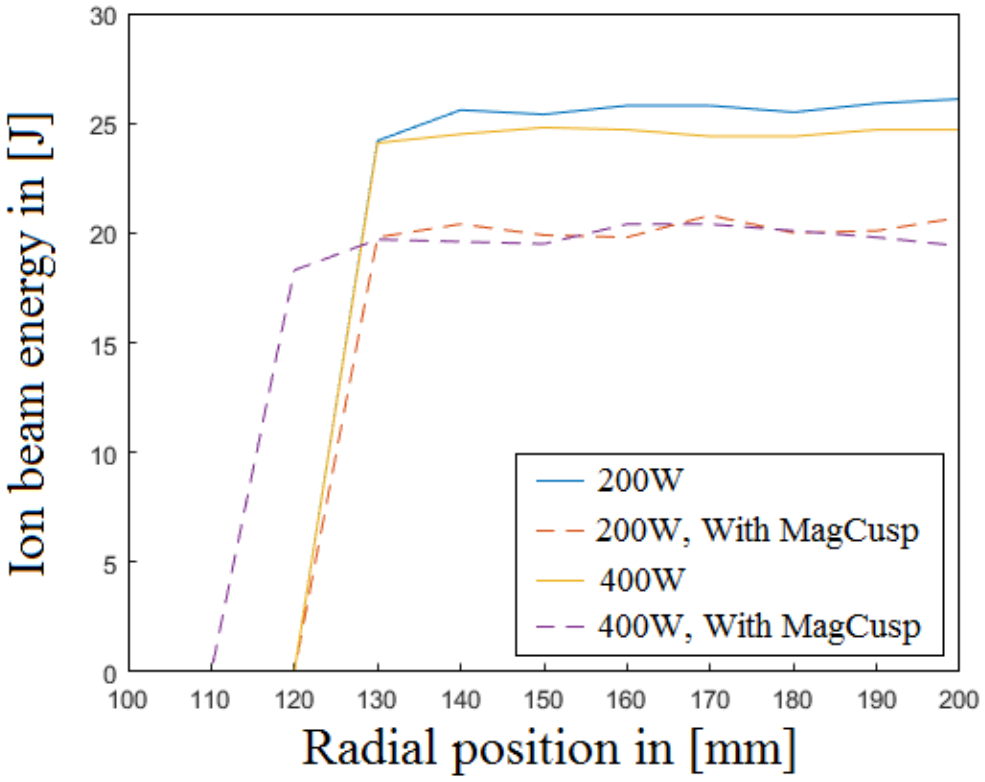

Figure 5.16: Radial ion beam energy E_{Beam} profiles versus RF-power at pressure $P_{Cap} = 0.65$ μBar (Flow $Q = 2$ SCCM) and magnetic coil current $I_{Coils} = 5$ A, without and with the magnetic band.

Here with increased pressure, E_{Beam} drops accordingly, and is still larger without the magnet band. There is also an interesting development at larger pressures ($P_{Cap} = 1.05$ μBar), where the radius of the beam is reduced to 3 cm away from the center. This shows that the increased pressure is reducing E_{Beam} and its distribution, and shows that an ion beam cannot form at much larger pressures in a helicon source, which is in agreement with previous reports [15, 41].

Lastly, the existence of an ion beam formation depends on the axial magnetic field is shown in Fig. 5.18. The data for the results can be found in Table C.4.

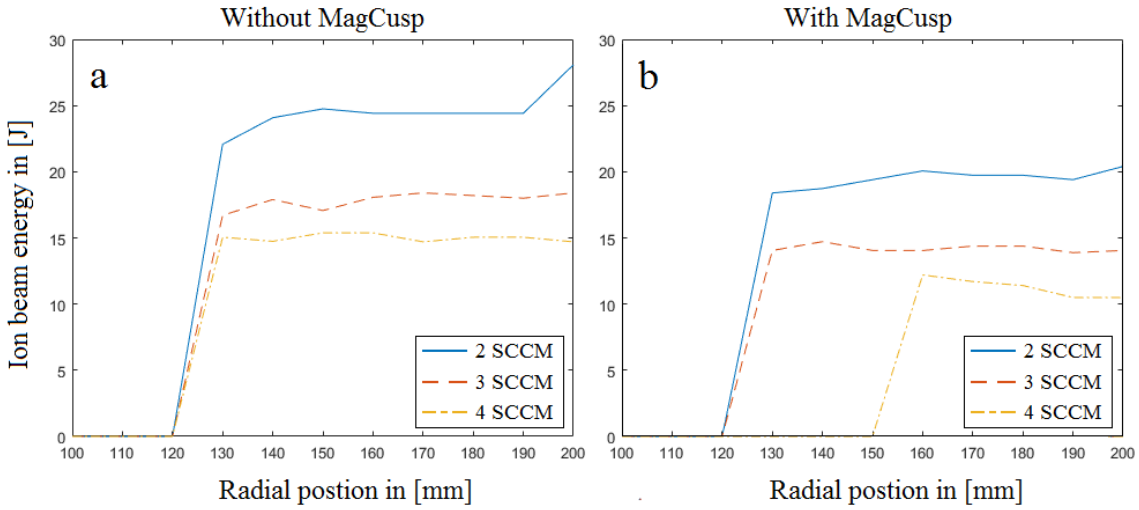

Figure 5.17: Radial ion beam energy E_{Beam} profiles versus pressure at magnetic coil current $I_{Coils} = 5$ A and RF-power range 400 W, without (a) and with (b) the magnetic band.

At low I_{Coils} values, there are no beam formation, which maybe due to the ion density peak and V_P -dip at these same I_{Coils} values as shown in Fig. 5.13. The figure also shows that the magnet band can prevent a beam from forming at $I_{Coils} = 3$ A, where from Fig. 5.14 is seen an increased density of 36.6 %, which suggest that a beam will not form with the magnet band on somewhere between $I_{Coils} = 3$ (100 Gauss) and $I_{Coils} = 4$ (135 Gauss). From $I_{Coils} \geq 4$ A, a beam is formed both with and without the magnet band, and Fig. 5.18 suggests that the difference in E_{Beam} with and without the magnet band becomes smaller. Similarly to the density ratio n_r with an increasing axial magnetic field discussed in Section 5.2.3, it seems that an increasing magnetic field strength will reduce the difference in E_{Beam} with and without the magnet band. In the same way as a large axial magnetic field will make the contribution from the magnet band negligible for the ion density, the difference between E_{Beam} with and without the magnet band will reduce. This is not possible to determine with Njord.

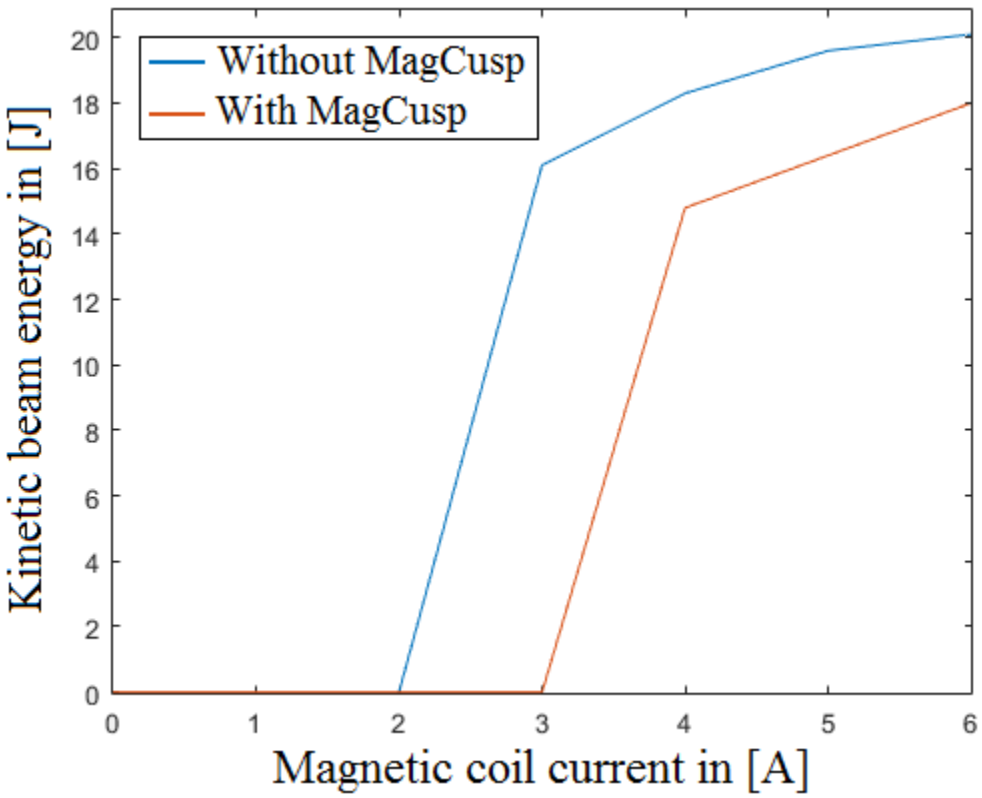

Figure 5.18: Center ion beam energy E_{Beam} versus magnetic coil current I_{Coils} at RF-power = 400 W, pressure P_{Cap} = 0.85 μBar (Flow Q = 3 SCCM), with and without the magnet band.

Chapter 6

Discussions

The results from the experiments have shown that a magnetic multipole cusp field around the port of a helicon plasma source significantly affects the plasma characteristics. The ion beam ratio n_r shows that the ion density is larger than unity with the magnet band over a range of RF-powers, pressure and for axial magnetic fields larger than 100 Gauss. Also, an increased density is evident at the edge of the plasma column, corresponding to the large plasma potential V_P drops, as shown by the radial V_P profiles. The effect on the density and density profiles provide evidence that the magnetic cusp field from the magnet band contributes to an increased plasma confinement in the system. Due to the reduction of plasma losses to the port wall, evaluations of the particle continuity equation is simplified, which can be used to calculate the momentum, energy and the general transport equation for further studies.

6.1 Ion beam flux

Investigations of the ion beam energy has shown a small reduction due to the increased density and the reduced plasma potentials V_P. The effect

of this reduction in energy due to the magnet band can be described by defining the ion beam velocity ratio v_{Br} as

$$v_{Br} = \frac{\text{Ion beam velocity with the magnetic band}}{\text{Ion beam velocity without the magnet band}} \tag{6.1}$$

where the ion beam velocity is estimated from the ion beam energy from Eq.(5.2) using classical kinematics, giving

$$v_{Beam} = \sqrt{\frac{2eE_{Beam}}{m_i}} \tag{6.2}$$

By using the definition from Eq.(5.2), the velocity ratio becomes

$$v_{Br} = \frac{\sqrt{E_{Beam}} \text{ With MagCusp}}{\sqrt{E_{Beam}} \text{ Without MagCusp}} \tag{6.3}$$

By investigating the effect the magnet band has on the density of the beam, one can define the ion beam density ratio n_{Br}. This ratio comes from the same evaluation as n_r, but instead of estimating the entire area underneath the distribution function, one only estimates the area beneath the second peak as shown in Fig. 4.7, (b). Using this definition, the ion beam flux ratio ϕ_{Br} can be described as

$$\phi_{Br} = n_{Br} v_{Br} \tag{6.4}$$

This flux ratio describes how much the beam flux is affected through the use of the magnet band. This effect can be shown by using the estimated values for the n_{Br} densities and v_{Br} velocities at the different parameter values. By using the ion beam density ratio and the ion beam velocity ratio at the center of the plasma column, which can be found in Table C.5, v_{Br} was estimated as a function of RF-power. The result is shown in Fig. 6.1.

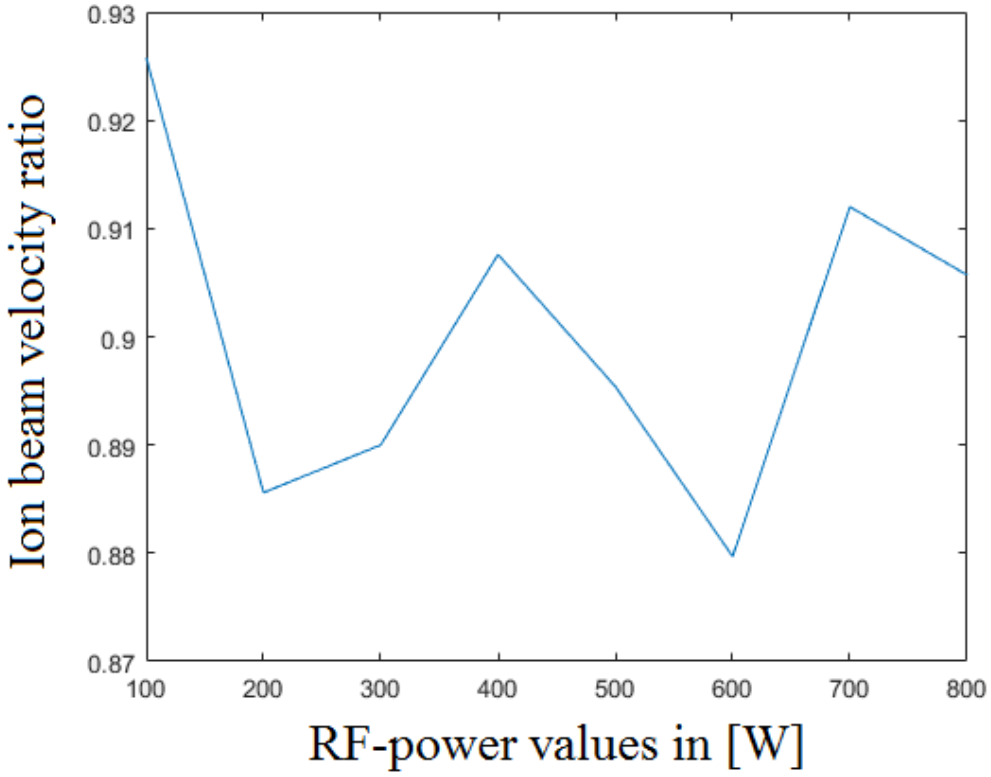

Figure 6.1: Center ion beam velocity ratio v_{Br} versus RF-power at magnetic coil current I_{Coils} and pressure $P_{Cap} = 0.65$ μBar (Flow Q = 2 SCCM).

The data of v_{Br} as a function of RF-power shows that the ratio between the ion beam velocities is varying slightly around 0.9. As the average ratio stays around this value at the entire RF-power range, it might suggest that the ratio of the ion beam energy with and without the magnet band is approximately constant at different RF-powers (at least at $[100 - 800]$ W). Because the v_{Br} ratio seems to be approximately constant, the flux ratio ϕ_{Br} will depende on the behaviour of n_{Br} only. This is shown in Fig. 6.2, and the values are listed in Table C.5.

The flux ratio shows an effective increase at higher RF-power values, with a maximum ratio at 600 W with an increase in the ion beam flux of about 50 % for the chosen pressure and axial magnetic field. In order to find

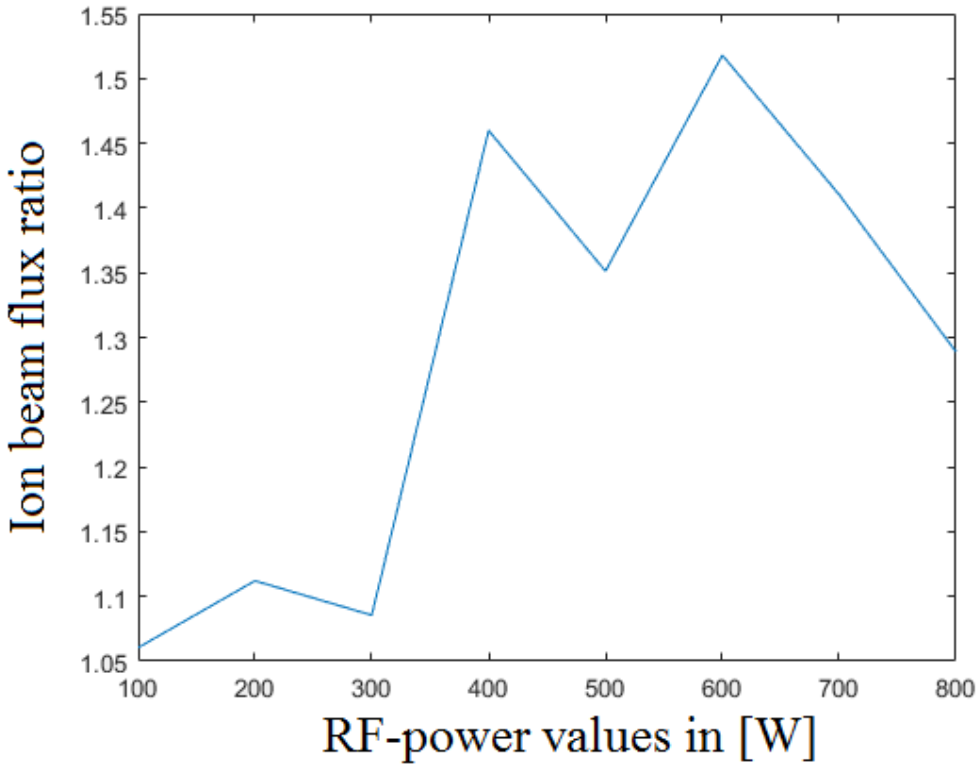

Figure 6.2: Center ion beam flux ratio ϕ_{Br} versus RF-power at magnetic coil current $I_{Coils} = 5$ A and pressure $P_{Cap} = 0.65$ μBar (Flow Q = 2 SCCM).

out what happens at RF-powers beyond 800 W, a new set of experiments needs to be carried out.

Further studies of the ion beam flux ratio also shows that the pressure affect the ion beam velocity ratio v_{Br}, where v_{Br} as a function of pressure is shown in Fig. 6.3.

The plot shows that the ion velocity with the magnet band on reduces the velocity more at higher pressures than without it, and has a very steep drop after 0.85 μBar at flow Q = 3 SCCM. This suggests that the pressure 0.85 μBar is the maximum pressure which can be chosen before the velocity drop affects the flux ratio ϕ_{Br}. This is shown in Fig. 6.4, with the values

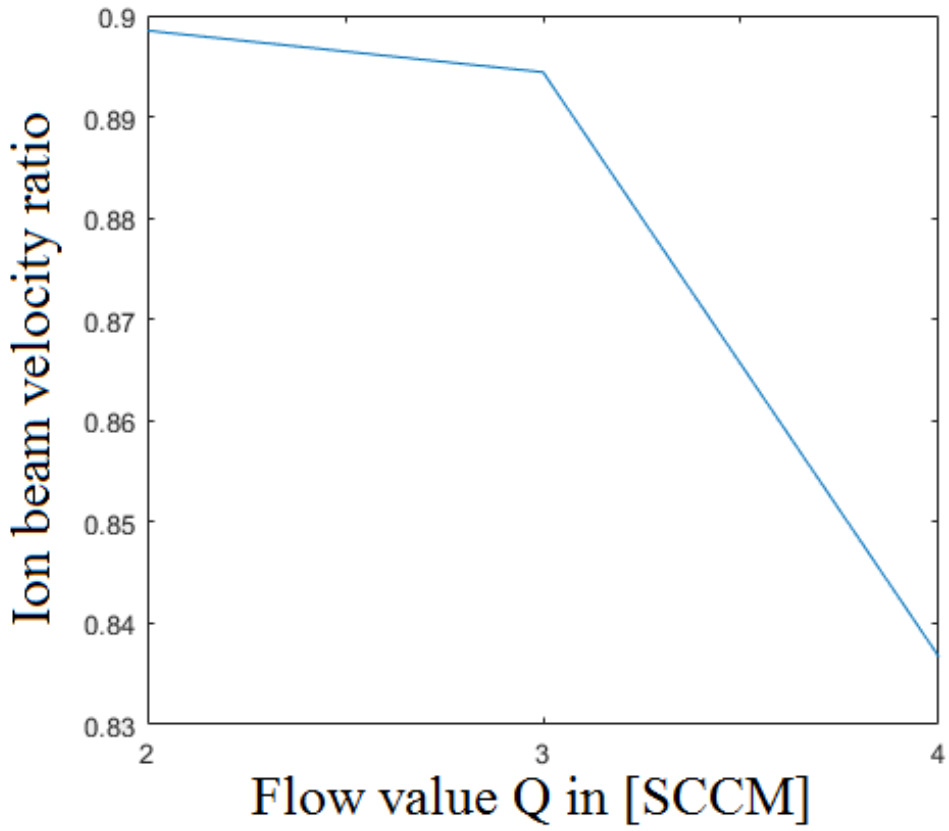

Figure 6.3: Center ion velocity ratio v_r versus pressure at RF-power = 400 W and magnetic coil current $I_{Coils} = 5$ A.

listed in Table C.6.

The plot shows that ϕ_{Br} has the largest flux ratio at pressure at 0.85 μBar at flow Q = 3 SCCM with the current parameter settings, with an increase of about 50 %. As shown in Section 5.3, a large pressure and can stop a beam from being generated, and from the results for the radial ion beam energy, the beam energy and radius decreases at pressures somewhere from $[0.85 - 1.05]$ μBar and above.

Lastly, the dependence of the ion beam velocity ratio dependency on the magnetic coil current was estimated, and is depicted in Fig. 6.5. The data values are listed in Table C.4.

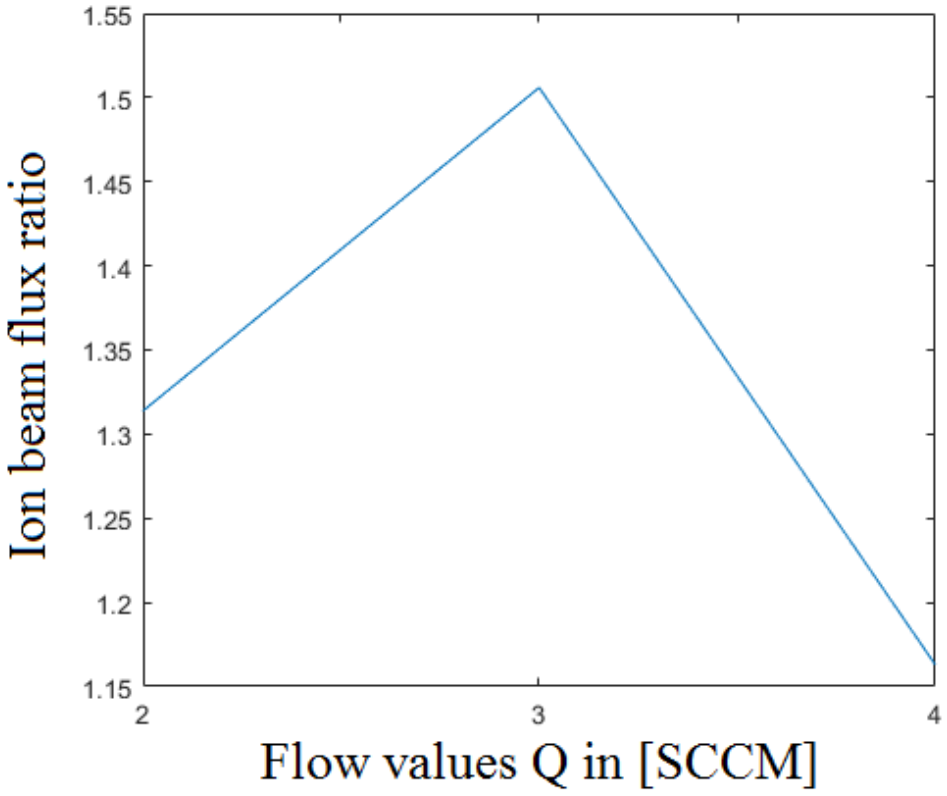

Figure 6.4: Center ion beam flux ratio ϕ_{Br} versus pressure at RF-power = 400 W and magnetic coil current $I_{Coils} = 5$ A.

The plot shows that the ion velocity ratio increases with the magnetic coil current. This is likely due to the increasing field strength which affects the trajectory of the ions, increases their speed while under the influence of the magnet band. Using v_{Br} along with n_{Br}, the ion beam flux ratio ϕ_{Br} is evaluated, and the results are shown in Fig. 6.6.

From the data for the ion beam, the maximum value of the flux ratio is found at $I_{Coils} = 5$ A at 160 Gauss at an increase of 50 %. The decrease at $I_{Coils} \leq 5$ A might be due to a density peaks below 100 Gauss which possibly decrease the ability to generate an ion beam due to the increased

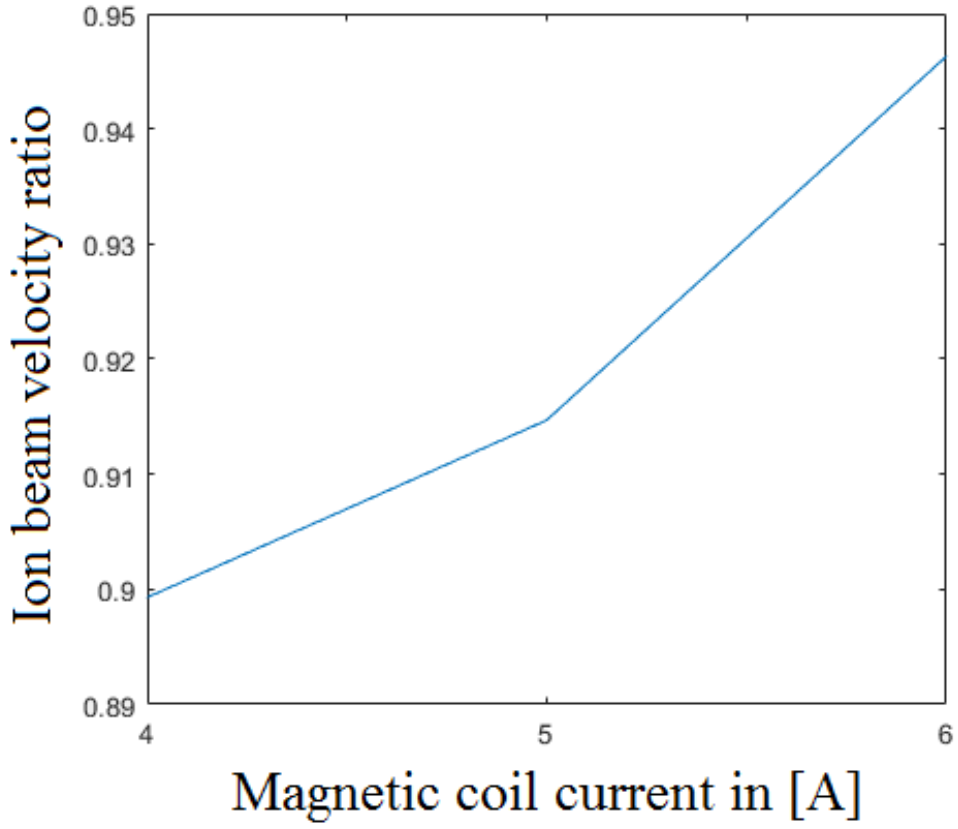

Figure 6.5: Center ion beam velocity ratio v_{Br} versus magnetic coil current I_{Coils} at RF-power = 400 W and pressure $P_{Cap} = 0.85$ μBar (Flow Q = 3 SCCM).

density. This phenomena will be discussed soon.

The results shows that the ion beam flux generally increases with the magnet band on at the port. With increased RF-power, the flux ratio ϕ_{Br} rises sharply to a plateau of around $[1.4 - 1.5]$ at RF-powers $>$ 300 W. The ratio ϕ_{Br} has a maximum at a flow of Q = 3 SCCM and a magnetic coil current $I_{Coils} = 5$ A. It is also possible to combine the RF-power value, pressure value and coil current values such that the ion beam flux ratio ϕ_{Br} may be increased even more than what the current results. The flux can again be used to obtain the thrust of the beam [42]. Since the ion beam

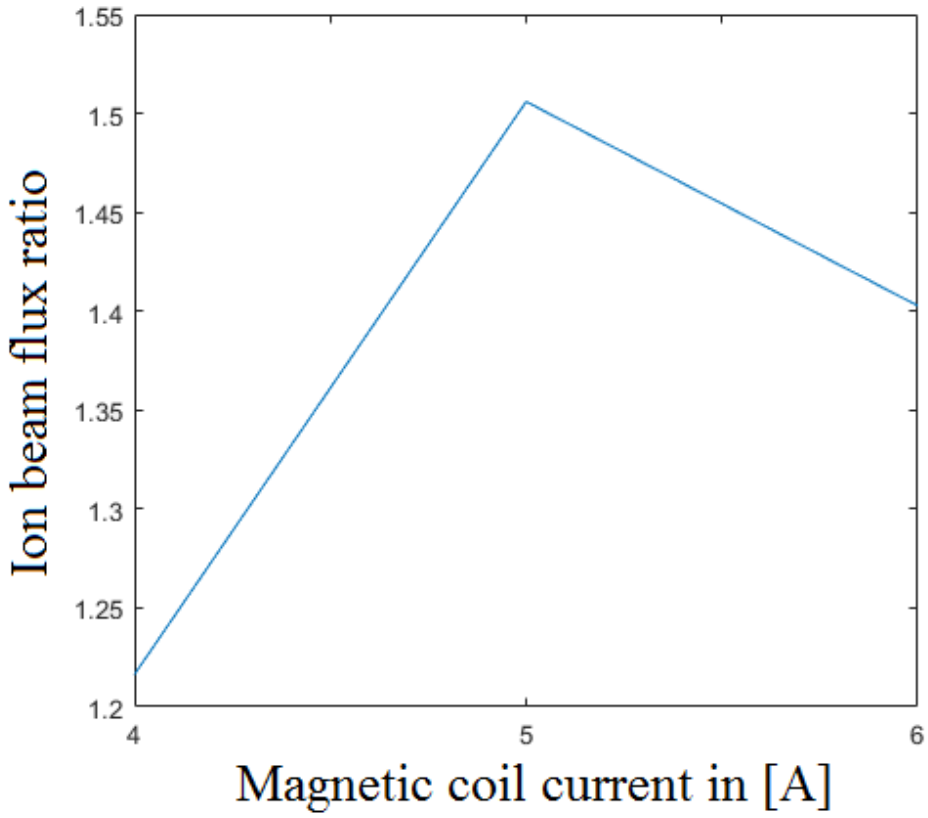

Figure 6.6: Center ion beam flux ratio ϕ_{Br} versus magnetic coil current I_{Coils} at RF-power = 400 W and pressure $P_{Cap} = 0.85$ μBar (Flow Q = 3 SCCM).

flux is increased by around 50 % with the magnet band at some of the parameter settings, this will essentially increase the thrust of the beam as well.

6.2 Density peak at low magnetic fields

From the results of the ion densities in Section 5.2.3, a density peak was discovered at a weak magnetic field below 100 Gauss at magnetic coil current $I_{Coils} \leq 3$ A. This phenomena has been discovered in different experiments

involving helicon sources, as shown in Fig. 6.7, [3].

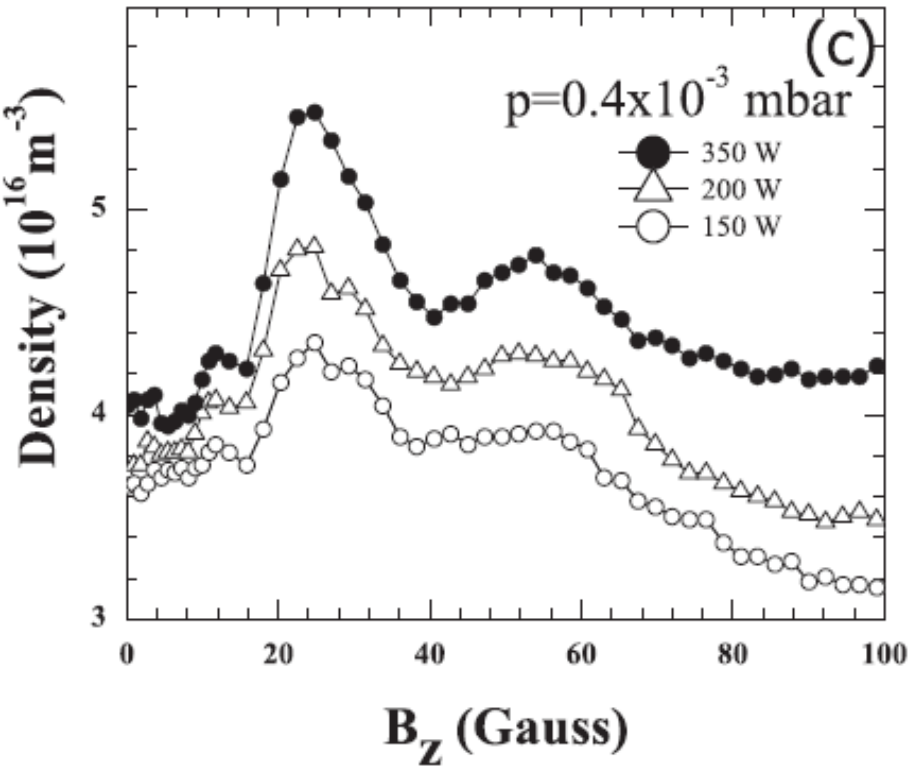

Figure 6.7: Density peak profiles for different RF powers (K. Barada, [3])

This phenomenon has also been observed in Njord measurements. The reason behind this density peak has still not been properly determined, but some suggestions have been given by different authors.

Brada [3] proposed that an oblique helicon wave propagating near the resonance cone boundary can cause an energy transfer from the helicon waves to the plasma when the low-field density peak appear. There was also reported multiple density peaks in low magnetic field and the absorption of left polarized wave near electron cyclotron resonance frequency.

Chen [43] suggested that the density peaks form due to constructive interference between a helicon mode of $m = +1$ produced by the antenna and the $m = +1$ mode generated due to the wall reflection of mode $m = -1$,

but this does not explain why the reflections only occur at weak magnetic fields.

Wang [44] has reported that there exist two density peaks in an expanding argon plasma with an axial magnetic field. He reported that the peaks are located somewhere at $[40-55]$ Gauss and at $[110-165]$ Gauss at an increasing RF-power from 100 W to 250 W and a pressure of 0.35 Pa, approximately half the pressure in Njord in most of the experiments. The experiments showed that there was an increased absorption of RF-power at the peaks, and the absorbed power of the two peaks showed a linear relation with the magnetic field. He suggests that the density peaks are caused to some extent by the excitation of the slow dispersion Trivelpiece-Gould (TG) waves through a non-resonance conversion.

Shamrai and Taranov [45] derived the wave dispersion relation for waves propagating parallel to the magnetic field in a bounded plasma medium analytically, and found that the wave dispersion relation has two modes. One is a fast helicon dispersion mode, and the other is the TG (slow dispersion) mode. They also predicted the possibility of mode conversion from helicon to TG mode in helicon plasmas. These two modes are well separated at magnetic fields higher than 200 Gauss for 13.56MHz, however at low magnetic fields below 100 Gauss they get coupled naturally under some typical conditions.

Cho [46] studied the dispersion characteristics of the radial eigenmodes and resistive loading of antennas in helicon plasmas and concluded that in case of helical antenna, the occurrence of a density peak at a critical low magnetic field is due to TG-helicon mode coupling when their perpendicular wave numbers are equal.

The physical reason behind this phenomena will not be solved in this thesis, as it is beyond its scope. However, measurements have showed

how the magnet affects its characteristics. As shown in Fig. 5.13, the ion density was larger at 35 Gauss (I_{Coils} = 1 A) and 67 Gauss (I_{Coils} = 2 A) without the magnet band, and from the ion density ratio n_r in Fig. 4.7, the ratio shows a ratio nearly down to nearly 0.8, a reduction close to 20 % with the magnet band on. It is clear that the plasma production is more efficient at this low magnetic fields, and the magnet cusps at the port reduces this efficiency. Because the plasma production comes from the use of helicon waves, the cusp fields must have a different interaction with the helicon waves at this weak field, hindering the waves to transfer energy to the electrons.

The plasma potential V_P and the ion density n_i data has shown a couple of characteristics by the parameter changes. First is that an reduction in $V_P$corresponds with an increase in n_i. An increase in RF-power causes an increase in n_i, due to the fact that splasma production increases with the RF-power. Lastly, an increse in pressure increases n_i as well, which is consistent with the power balance relation in a inductive coupled discharge plasma [4]. These characteristics for the parameter variables was determined by J. Hopwood [2, 4] by studying the electromagnetic fields in a RF inducted plasma, which also included a magnetic multipole confinement configuration. This shows that the data provided from the experiments in Njord is consistent with earlier results. Some of the results from Hopwood is given in Fig. 6.8 and Fig. 6.9.

From the results of the ion beam flux, it has been shown that the magnet band increase the flux up to 50 % for a single parameter change (RF-power, pressure and coil current), and a combination of the three parameters mights increase the flux even more. If one includes the entire background plasma and assume that the plasma velocity ratio v_r with and

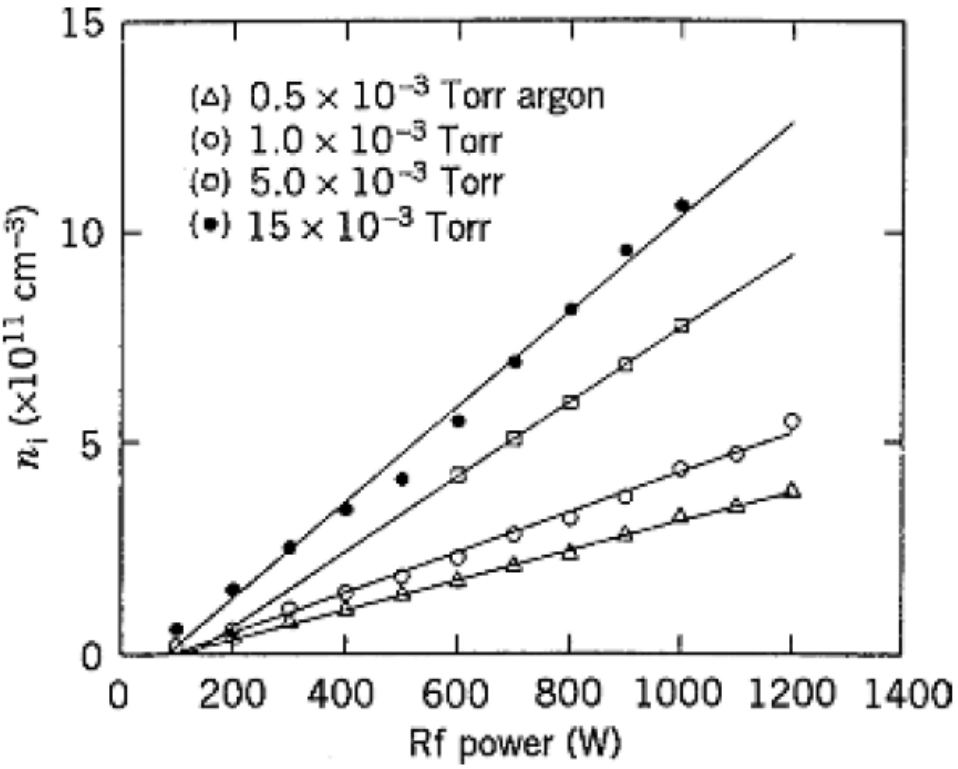

Figure 6.8: Ion density n_i versus RF-power and argon pressure ([4] 1993b).

without the magnet band has a similar ratio to the ion beam velocity ratio v_{Br}, the plasma flux ratio $\phi_r = n_r v_r$ can be increased up to 80 % from the singe parameter changes alone, and potentially doubled with a combination with them. This will also mean a doubling in the plasma momentum and the plasma thrust with the magnet band. This could be utilised by satellites and deep space probes which are propelled by plasma thrusters, resulting in either velocities nearly twice the amount with a magnetic multipole confinement, or alternatively it can increase the distance covered due to the reduction of plasma losses, effectively making use of the ions that would be lost due to collisions to the wall.

In order to increase the effect of a multipole confinement, more permanent magnets (PM) in a series or replacing them by more powerful, larger

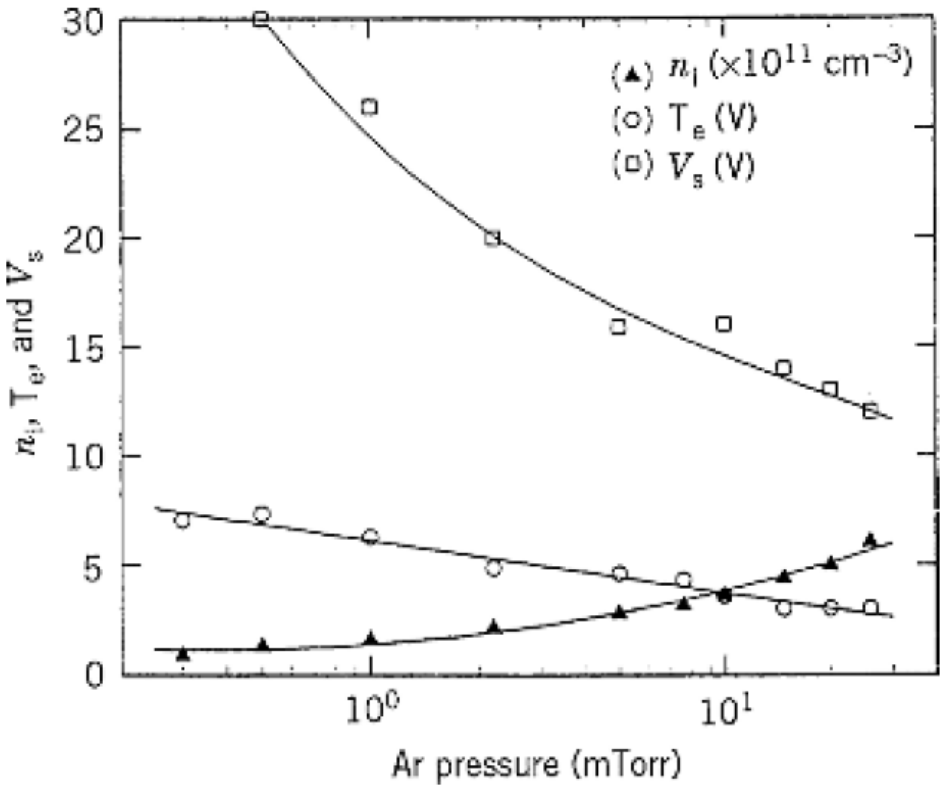

Figure 6.9: Ion density n_i, electron temperature T_e and plasma potential V_P versus argon pressure in a RF-power = 500 W discharge with magnetic multipole confinement ([4] 1993b).

PMs could be added, but such PMs can be difficult to work with, and they weigh more. A solution for this could be the use of a diamagnet (DM) when a power supply is available. A DM can be even more powerful that a PM, and they have the ability to adjust the magnetic field strength by fine-tuning the current which goes through it. The same effect can be achieved through the use of coils, inducing a magnetic field by running a current through the coil and fine-tune the current for adjusting the field. However, the DMs and coils are restricted in some cases, as they both require a power supply, and their physical size can make it harder to use them on small plasma devices or in confined spaces.

Chapter 7

Conclusion

The usage of the magnetic band showed that it could noticeably affect the plasma characteristics, sucha s enhance the density in a plasma source such as Njord. The plasma density increased by a ratio of two at RF-powers $\geq$ 600 W in the center of the plasma column and up to 30 % at the plasma edges. An increase in pressure has shown an increase in density as well, from 66.5 % at 0.65 μBar up to 90 % at 1.05 μBar under the influence of a 400 W RF-power and a magnetic field at a current coil value $I_{Coils} = 5$ A. Without any axial magnetic field, the magnet band has shown an increase in density just below 30 % at 400 W, but has shown a max effect just below 170 Gauss at a magnetic coil current of $I_{Coils} = 5$ A. A combination of the three variables may increase the density even further, giving a better multipole confinement system. The ion beam velocity was reduced overall around 10 %, but the increased beam density showed that the ion beam flux increased by 50 % both with an increased RF-power of 600 W, a pressure of 0.85 μBar and a magnetic coil current of $I_{Coils} = 5$ A, each variables changed separately. Combining the beam velocity and density, the result shows that the beam flux increases with the magnet band.

This is in a simple system consisting of a low-pressured, cold plasma in a

straight cylindrical source influenced by an expanding axial magnetic field. More complex systems with much higher energetic plasmas combined with non-lonear sources will require a different set-up for a multipole confinement system. This will require more studies and possibly experimentations in order to find out.

Appendices

Appendix A

Tables of the plasma potential results

In this appendix, the different radial plasma potentials are listed up. This includes

- Radial V_P profiles at different RF-powers with and without the magnet band
- Radial V_P profiles at different pressures/flows with and without the magnet band
- Radial V_P profiles at different axial magnetic field strengths with and without the magnet band

The center profiles are extracted from the radial profiles at r = 180mm.

Table A.1: Radial plasma potential V_P profiles in [V] versus RF-power in [W] at pressure $P_{cap} = 0.65$ μBar (Flow Q = 2 SCCM) and magnetic coil current $I_{Coils} = 5$ A at RF-power range $[100 - 400]$ W, with and without magnet band (S. Golay filter width: 15).

	With MagCusps				Without MagCusps			
r [mm]	100 W	200 W	300 W	400 W	100 W	200 W	300 W	400 W
0	40.8	40.9	40.5	39.8	41.8	42.3	42.8	40.1
10	41.8	42.2	40.8	40.2	42	43	43	40.5
20	42.1	42.5	42.5	40.8	42.8	43.5	43.5	40.8
30	42.5	43.5	42.5	41.8	42	43.8	44.15	41.2
40	42.8	43.7	43.5	42.1	43.5	44.4	44.5	41.8
50	42.8	43.8	43.8	42.5	43.5	44.8	44.5	41.8
60	43.8	44.5	44.2	42.8	44.8	45.2	45.15	42.5
70	44.5	44.8	44.8	43.2	44.5	45.5	45.5	42.5
80	44.5	45.2	45.15	43.7	44.8	45.8	45.8	42.8
90	45.2	45.8	45.8	44.5	45.2	45.8	46.1	43.3
100	45.5	45.85	45.85	45	45.5	46.15	46.15	43.5
110	45.5	46.1	46.15	45.2	45.8	46.5	46.15	43.8
120	46.2	46.5	46.5	45.5	46.2	46.5	46.7	44.2
130	46.2	46.85	46.8	45.8	46.5	46.85	46.85	44.5
140	46.5	46.85	46.85	46.2	46.5	47	47.5	44.5
150	46.5	47.3	47.2	46.2	46.5	47.5	47.5	44.8
160	46.5	47.5	47.5	46.2	46.85	47.5	47.5	45.2
170	46.6	47.5	47.5	45.8	46.5	47.5	47.5	45.2
180	46.5	47.5	47.2	46.2	46.8	47.5	47.5	45.2
190	46.5	47.2	46.85	46.2	46.5	47.5	47.4	45.1
200	46.5	46.85	46.8	45.6	46.5	47.5	47.5	45.2

Table A.2: Radial plasma potential V_P profiles in [V] versus RF-power in [W] at pressure $P_{cap} = 0.65$ μBar (Flow Q = 2 SCCM) and magnetic coil current $I_{Coils} = 5$ A at RF-power range $[500 - 800]$ W, with and without magnet band (S. Golay filter width: 15).

	With MagCusps				Without MagCusps			
r [mm]	500 W	600 W	700 W	800 W	500 W	600 W	700 W	800 W
0	39.5	36.8	39.8	36.1	39.8	39	37.5	37.2
10	39.8	37.5	37	36.5	40	39.5	38	37.5
20	40.1	39.1	38.1	36.8	40.5	39.8	38	37.8
30	40.4	40.1	39.8	37.3	40.8	40.1	39.3	38
40	41.5	40.5	39.5	38.5	41.1	40.5	39.3	39.5
50	42.1	41	39.8	38.8	41.8	41.5	40.5	39.5
60	42.5	41.2	40.5	39.8	42.1	41.8	40.8	40.1
70	42.8	42.2	40.8	40.2	42.5	42	41.1	40.5
80	43.5	42.5	41.2	40.5	42.5	42.2	41.8	40.5
90	43.8	42.8	42.2	41.1	42.8	42.5	42.1	41.5
100	44.3	43.3	42.5	41.5	43.5	42.8	42.5	41.8
110	44.5	43.8	42.8	42.5	43.8	43.5	42.8	42.1
120	45.2	44.2	43.5	42	44	43.7	43.1	42.5
130	45.3	44.2	43.5	43	44.2	43.8	43.5	42.8
140	45.5	44.5	43.8	42.8	44.5	44.2	43.6	42.5
150	45.6	45	44.1	43.5	44.5	44.5	43.8	42.5
160	46.3	45.5	44.2	43.2	44.8	44.5	44.2	43.2
170	45.8	45.5	44.2	43.5	44.8	44.5	44.3	43.5
180	45.8	45.2	44.2	43.5	45.2	44.5	44.8	43.5
190	45.5	44.2	44.2	43	44.8	44.5	44.2	43.5
200	45.5	44.9	43.9	43	44.8	44.5	44.2	43.2

Table A.3: Radial plasma potential V_P profiles in [V] versus RF-power in [W] at pressure $P_{cap} = 0.65$ μBar (Flow Q = 2 SCCM) and magnetic coil current $I_{Coils} = 0$ A at RF-power range $[100 - 400]$ W, with and without magnet band (S. Golay filter width: 9).

	With MagCusps				Without MagCusps			
r [mm]	100 W	200 W	300 W	400 W	100 W	200 W	300 W	400 W
0	33.5	31.5	29.1	26.9	36.1	32.5	30.5	27.8
10	33.8	31.5	29.5	26.8	36.5	33.1	31	28.1
20	33.8	31.8	29.8	27.1	36.8	33.2	31.9	28.4
30	34.1	32	30.1	28	37.1	33.6	31.5	29.1
40	34.5	32.5	31.1	28.1	37.5	33.8	32	29.5
50	39	33	31.1	29	37.8	34.1	32.8	29.8
60	35.1	33.1	31.8	29.5	38.1	34.5	33.1	30.8
70	35.5	33.5	32.1	29.8	38.8	35.1	33.5	31.1
80	35.8	33.8	32.8	30.1	38.8	35.5	33.8	31.5
90	36.1	34.1	33.1	31.1	39.1	39.8	34.1	31.8
100	36.5	34.5	33.5	31.2	39.5	35.8	34.8	31.8
110	36.8	35	33.8	31.6	39.9	36.1	35.1	32
120	37.1	39.1	34.15	31.8	39.8	36.5	39.1	33.1
130	37.2	35.2	34.5	32	40	36.8	35.5	33.3
140	37.5	35.4	34.8	32.5	40.2	36.8	35.8	33.5
150	37.6	35.5	35.1	33.1	40.3	36.8	39.8	33.8
160	37.8	35.8	35.15	33.1	40.5	36.8	36.1	33.8
170	37.8	35.8	35.4	33.1	40.5	37.1	36.2	33.8
180	37.8	35.8	35.15	33.5	40.5	37.1	35.8	34
190	37.6	35.8	35.15	33.1	40.2	37	35.8	33.8
200	37.3	35.5	35	33	40	36.8	35.8	33.8

Table A.4: Radial plasma potential V_P profiles in [V] versus pressures at RF-power = 400 W and magnetic coil current I_{Coils} = 5 A, with and without magnet band (S. Golay filter width: 15).

	With MagCusps			Without MagCusps		
r [mm]	2.0 SCCM	3.0 SCCM	4.0 SCCM	2.0 SCCM	3.0 SCCM	4.0 SCCM
0	40.5	33.4	30.3	43.15	35.8	32,15
10	41.15	33.8	30.45	43.5	36.15	32.45
20	41.8	34.3	30.45	43.8	36.5	32.8
30	42.5	34.8	30.8	44.2	36.8	33
40	43.15	35.45	31.8	44.5	37.15	33.45
50	43.85	35.8	32.1	45.15	37.5	33.8
60	44.5	36.5	32.5	45.5	37.8	34.15
70	44.5	36.8	33.1	45.8	38.15	34.45
80	44.8	37.5	33.45	46.15	38.5	37.8
90	45.5	37.8	34.1	46.5	38.8	35.15
100	45.8	38.5	34.45	46.5	39.15	35.5
110	46.2	38.5	34.7	46.85	39.7	35.8
120	46.5	38.8	34.8	47.5	39.8	36
130	46.5	39.15	35.1	47.85	40.15	36.15
140	46.85	39.5	35.45	47.85	40.3	36.5
150	47	39.8	35.5	47.85	40.5	36.5
160	47.5	39.8	35.8	48.15	40.5	36.5
170	47.5	39.8	35.8	48.2	40.5	36.8
180	47.5	39.8	35.8	48.2	40.5	36.8
190	47.2	39.8	35.8	48.2	40.5	36.8
200	47	39.5	35.8	47.85	40.5	36.8

Table A.5: Radial plasma potential V_P profiles in [V] versus pressures at RF-power = 400 W and magnetic coil current I_{Coils} = 0 A, with and without magnet band (S. Golay filter width: 15).

	With MagCusps		Without MagCusps	
r [mm]	3.0 SCCM	4.0 SCCM	3.0 SCCM	4.0 SCCM
0	29.1	26.1	30.8	27.1
10	29.8	26.45	30.8	27.45
20	30.45	26.8	31.45	28.1
30	30.8	27.1	32.1	28.6
40	31.45	28.1	32.45	29.1
50	32.1	28.45	33.1	29.45
60	32.8	28.8	33.8	30.1
70	32.8	29.45	34.45	30.45
80	33.8	30.1	34.8	30.8
90	34.1	30.3	35.4	31.1
100	34.8	30.8	35.8	31.8
110	35.15	30.8	36.1	32.1
120	35.8	31.45	36.45	32.45
130	36.15	31.8	36.45	32.8
140	36.5	32.1	36.8	32.8
150	36.8	32.1	37.15	32.8
160	36.8	32.45	37.8	33.45
170	36.8	32.45	37.8	33.45
180	36.8	32.8	37.8	33.8
190	36.8	32.8	37.5	33.45
200	37.15	32.45	37.8	33.1

Table A.6: Center plasma potential V_P in [V] versus magnetic coil current I_{Coils} at RF-power = 400 W, pressure P_{Cap} = 0.85 μBar (Flow Q = 3 SCCM), with and without magnet band.

I_{Coils}	With MagCusps	Without MagCusps
0	30.6	32.3
1	18	16.8
2	23.5	21.8
3	29.2	31.2
4	33.2	34.7
5	35.9	37
6	37.2	38.7

Appendix B

Tables of the ion density results

In this appendix, the different radial ion densities are listed up. This includes

- Radial n_i profiles at different RF-powers with and without the magnet band
- Radialn_i profiles at different pressures/flows with and without the magnet band
- Radial n_i profiles at different axial magnetic field strengths with and without the magnet band

The center profiles are extracted from the radial profiles at r = 180mm.

Table B.1: Radial ion density n_i profiles in m^{-3} versus RF-power at pressure $P_{Cap} = 0.65$ μBar (Flow Q = 2 SCCM) and magnetic coil current $I_{Coils} = 5$ A at RF-power range $[100 - 400]$ W, with and without magnet band (S. Golay filter width : 15).

	With MagCusps				Without MagCusps			
r [mm]	100 W	200 W	300 W	400 W	100 W	200 W	300 W	400 W
0	0.1713	0.2608	0.3549	0.4624	0.1782	0.2698	0.3401	0.4143
10	0.1812	0.2743	0.3733	0.484	0.1837	0.2742	0.3536	0.4244
20	0.1905	0.2956	0.4128	0.5374	0.1871	0.2798	0.3601	0.4378
30	0.202	0.3239	0.453	0.6	0.1982	0.2875	0.3703	0.458
40	0.2111	0.3456	0.4947	0.656	0.2035	0.2966	0.3814	0.47
50	0.226	0.3767	0.5294	0.6983	0.2105	0.3037	0.3939	0.462
60	0.2435	0.4075	0.5749	0.7522	0.2153	0.3113	0.4021	0.483
70	0.2606	0.4437	0.6135	0.8125	0.2214	0.3225	0.4173	0.5034
80	0.2761	0.4726	0.6685	0.8894	0.2307	0.3365	0.4352	0.5231
90	0.2928	0.5106	0.7212	0.9473	0.2421	0.3498	0.4483	0.5467
100	0.3067	0.5433	0.7749	1.0081	0.2497	0.362	0.4721	0.5731
110	0.3216	0.5748	0.8236	1.0773	0.2579	0.3732	0.4897	0.601
120	0.3385	0.6038	0.873	1.14	0.2708	0.3912	0.5171	0.625
130	0.3525	0.6335	0.9222	1.2037	0.2833	0.4079	0.5407	0.6587
140	0.3643	0.661	0.97	1.2647	0.2923	0.4211	0.5664	0.6937
150	0.3709	0.6739	0.9977	1.3050	0.3	0.4292	0.58	0.7054
160	0.3751	0.6775	1.005	1.3186	0.3049	0.4372	0.5824	0.7121
170	0.3736	0.6729	0.9967	1.3109	0.3093	0.4376	0.5832	0.715
180	0.3742	0.6693	0.9834	1.3	0.3123	0.439	0.5828	0.72
190	0.3782	0.6709	0.976	1.2968	0.3142	0.4397	0.5851	0.718
200	0.3794	0.672	0.9724	1.2981	0.3138	0.4406	0.5836	0.718

Table B.2: Radial ion density n_i profiles in m^{-3} versus RF-power at pressure $P_{Cap} = 0.65$ μBar (Flow Q = 2 SCCM) and magnetic coil current $I_{Coils} = 5$ A at RF-power range $[500 - 800]$ W, with and without magnet band (S. Golay filter width : 15).

	With MagCusps				Without MagCusps			
r [mm]	500 W	600 W	700 W	800 W	500 W	600 W	700 W	800 W
0	0.59	0.743	0.932	1.1564	0.5050	0.602	0.7368	0.895
10	0.6226	0.7928	1	1.3251	0.5168	0.6215	0.77	0.9256
20	0.6917	0.8778	1.1124	1.3734	0.533	0.6422	0.79	1.0465
30	0.7875	0.9993	1.269	1.5824	0.5466	0.665	0.8221	1.0310
40	0.861	1.1005	1.3953	1.7594	0.561	0.6856	0.8563	1.1
50	0.9189	1.2	1.51	1.9090	0.576	0.7045	0.893	1.1273
60	1	1.27	1.64	2.1175	0.5960	0.73	0.9241	1.19
70	1.08	1.3916	1.82	2.2889	0.6168	0.763	0.9777	1.258
80	1.178	1.5384	2.02	2.5495	0.649	0.8013	1.04	1.35
90	1.27	1.654	2.55	2.8622	0.6823	0.8538	1.1151	1.4430
100	1.3610	1.7856	2.4	3.15	0.7174	0.91	1.1971	1.57
110	1.4527	1.9105	2.6	3.553	0.7550	0.961	1.2558	1.7049
120	1.54	2.0309	2.8112	3.7240	0.7990	1.0255	1.373	1.8
130	1.635	2.2	3.0022	4	0.8460	1.099	1.4668	1.996
140	1.72	2.3	3.2	4.2876	0.8854	1.157	1.555	2.1308
150	1.789	2.4	3.3608	4.4785	0.9132	1.2053	1.6362	2.3
160	1.815	2.49	3.47	4.7142	0.9275	1.2396	1.68	2.42
170	1.83	2.52	3.55	4.8315	0.9275	1.249	1.7189	2.422
180	1.8123	2.5463	3.63	4.895	0.9368	1.25	1.8	2.4275
190	1.8102	2.53	3.594	4.83	0.9290	1.2595	1.774	2.42
200	1.81	2.53	3.52	4.8	0.911	1.252	1.7488	2.4177

Table B.3: Radial ion density n_i profiles in m^{-3} versus pressure at RF-power = 400 W and magnetic coil current $I_{Coils} = 5$ A, with and without magnet band (S. Golay filter: 15)

	With MagCusps			Without MagCusps		
r [mm]	2.0 SCCM	3.0 SCCM	4.0 SCCM	2.0 SCCM	3.0 SCCM	4.0 SCCM
0	0.4631	0.5412	0.6115	0.4225	0.4623	0.4589
10	0.4886	0.5862	0.6503	0.4345	0.4774	0.473
20	0.5344	0.6507	0.6961	0.4493	0.4919	0.4924
30	0.5921	0.7214	0.7795	0.4642	0.5046	0.5081
40	0.6503	0.7712	0.8475	0.4784	0.518	0.5233
50	0.7187	0.83	0.8966	0.4941	0.5332	0.5421
60	0.7546	0.89	0.9599	0.5123	0.5483	0.545
70	0.8213	0.9648	1.0238	0.5352	0.5754	0.5919
80	0.8857	1.0462	1.1059	0.5618	0.6002	0.6223
90	0.9532	1.123	1.1895	0.5971	0.6285	0.6515
100	1.10145	1.12054	1.2785	0.6274	0.6611	0.6895
110	1.0806	1.2845	1.3813	0.6622	0.6953	0.7273
120	1.1431	1.3653	1.4675	0.7034	0.7290	0.7723
130	1.2141	1.4405	1.5545	0.7421	0.7630	0.8134
140	1.2830	1.552	1.62	0.7774	0.7937	0.8422
150	1.333	1.5537	1.6585	0.7958	0.8143	0.8608
160	1.3589	1.5575	1.6907	0.8143	0.823	0.8853
170	1.3554	1.576	1.699	0.8117	0.8245	0.8816
180	1.35	1.548	1.6747	0.8108	0.8205	0.8786
190	1.3368	1.5335	1.6566	0.8092	0.8222	0.8783
200	1.3426	1.5199	1.6295	0.8106	0.8171	0.8709

Table B.4: Radial ion density n_i profiles in m^{-3} versus pressure at RF-power = 400 W and magnetic coil current $I_{Coils} = 0$ A, with and without magnet band (S. Golay filter: 15)

	With MagCusps		Without MagCusps	
r [mm]	3.0 SCCM	4.0 SCCM	3.0 SCCM	4.0 SCCM
0	0.5094	0.575	0.3979	0.4604
10	0.5763	0.6343	0.4442	0.5071
20	0.646	0.729	0.5011	0.5811
30	0.7339	0.8389	0.5799	0.6665
40	0.8524	0.9735	0.6606	0.7657
50	0.9853	1.1205	0.7602	0.8809
60	1.1441	1.2859	0.8804	1.0258
70	1.3255	1.483	1.0133	1.174
80	1.5303	1.6913	1.1559	1.3334
90	1.7306	1.8938	1.3103	1.4956
100	1.9611	2.1278	1.4602	1.67
110	2.1696	2.3524	1.6333	1.8617
120	2.3876	2.5848	1.8127	2.0264
130	2.5511	2.795	1.996	2.2163
140	2.7661	2.9622	2.1111	2.3211
150	2.923	3.1096	2.248	2.4308
160	2.9757	3.21	2.3515	2.5293
170	2.9822	3.2756	2.3495	2.5908
180	2.9635	3.2335	2.3386	2.5845
190	2.9537	3.1697	2.36	2.5367
200	2.848	3.0332	2.238	2.5164

Table B.5: Radial ion density ratio n_r profiles versus pressure at RF-power = 400 W with magnetic coil current $I_{Coils} = 5$ A and $I_{Coils} = 0$ A.

	$I_{Coils} = 5$ A			$I_{Coils} = 0$ A	
r [mm]	2.0 SCCM	3.0 SCCM	4.0 SCCM	3.0 SCCM	4.0 SCCM
0	1.096	1.17	1.13325	1.28	1.2489
10	1.1245	1.228	1.3748	1.2974	1.2508
20	1.1844	1.32283	1.4137	1.29	1.2555
30	1.2755	1.43	1.5341	1.2655	1.2587
40	1.3593	1.489	1.4953	1.29	1.2714
50	1.4545	1.5563	1.654	1.3	1.272
60	1.4729	1.6232	1.7024	1.3	1.2536
70	1.5345	1.6767	1.73	1.31	1.2632
80	1.57654	1.743	1.7771	1.324	1,2684
90	1.5964	1.7868	1.8258	1.32	1.2662
100	1.617	1.8233	1.8542	1.343	1.2741
110	1.6318	1.8474	1.9	1.328	1.2636
120	1.6251	1.873	1.89	1.317	1.2756
130	1.636	1.888	1.9111	1.278	1.2611
140	1.6504	1.9554	1.9235	1.31	1.2762
150	1.675	1.9080	1.927	1.3	1.2792
160	1.6688	1.8924	1.96	1.2654	1.2692
170	1.67	1.911	1.9272	1.27	1.2643
180	1.665	1.88665	1.9061	1.267	1.2511
190	1.652	1.865	1.8861	1.25	1.2495
200	1.6563	1.86	1.8721	1.2725	1.2054

Table B.6: Center ion density n_i versus magnetic coil current I_{Coils} at RF-power = 400 W an pressure $P_{Cap} = 0.85$ μBar (Q = 3 SCCM).

I_{Coils}	With MagCusps	Without MagCusps
0	2.9894	2.4125
1	7.8696	9.635
2	6.068	7.2548
3	3.3924	2.4825
4	2.2433	1.2324
5	1.4425	0.8026
6	1.0553	0.6511

Table B.7: Center ion density ratio n_r versus of magnetic coil current I_{Coils} at RF-power 400 W, pressure $P_{Cap} = 0.65$ μBar (Flow $Q = 2$ SCCM).

I_{Coils}	n_r
0	1.2391
1	0.8168
2	0.8364
3	1.3665
4	1.8203
5	1.7973
6	1.6208

Appendix C

Tables of the ion beam energy results

In this appendix, the different radial ion beam energies are listed up. This includes

- Radial E_{Beam} profiles at different RF-powers with and without the magnet band
- Radial E_{Beam} profiles at different pressures/flows with and without the magnet band
- Radial E_{Beam} profiles at different axial magnetic field strengths with and without the magnet band

The center profiles are extracted from the radial profiles at r = 180mm.

Table C.1: Radial ion beam E_{Beam} profiles in [J] versus RF-power at pressure P_{Cap} = 0.65 μBar (Flow Q = 2 SCCM) and magnetic coil current I_{Coils} = 5 A, with and without magnet band.

	With MagCusps				Without MagCusps			
r [mm]	100 W	200 W	300 W	400 W	100 W	200 W	300 W	400 W
130	16.7	19.8	18.7	19.7	22.4	24.2	25.1	24.1
140	19	20.4	20.8	19.6	23.4	25.6	25.1	24.5
150	19.5	19.9	20.4	19.5	23.8	25.4	25.8	24.8
160	20.7	19.8	20.5	20.4	23.8	25.8	25.1	24.7
170	21.3	20.8	19.8	20.4	24.4	25.8	25.5	24.4
180	20.4	20	20.2	20.1	23.8	25.5	25.5	24.4
190	20.7	20.1	20.8	19.8	24.1	25.9	25.8	24.7
200	20.7	20.7	20.2	19.4	23.5	26.1	25.4	24.7

Table C.2: Center ion beam energy E_{Beam} in [J] versus RF-Power at pressure P_{Cap} = 0.65 μBar (Q = 2 SCCM) and magnetic coil current I_{Coils} = 5 A, with and without magnet band.

RF	With MagCusps	Without MagCusps
100	20.4	23.8
200	20	25.5
300	20.2	25.5
400	20.1	24.4
500	19.4	24.2
600	17.8	23
700	17.8	21.4
800	17.8	21.7

Table C.3: Radial ion beam E_{Beam} profiles in [J] versus pressures at RF-power = 400 W and magnetic coil current $I_{Coils} = 5$ A, with and without magnet band.

	With MagCusps			Without MagCusps		
r [mm]	2 sccm	3 sccm	4 sccm	2 sccm	3 sccm	4 sccm
130	18.3947	14.0468		22.0749	16.7	15.05
140	18.7291	14.7187		24.0803	17.9	14.74
150	19.398	14.0468		24.7492	17.065	15.38
160	20.06	14.0468	12.2	24.4147	18.065	15.38
170	19.7325	14.3812	11.7	24.4247	18.4	14.7
180	19.7325	14.3812	11.4	24.4147	18.2	15.05
190	19.4	13.8839	10.5	24.4147	18	15.05
200	20.4	14.05	10.55	28.0836	18.4	14.7

Table C.4: Center ion beam energy E_{Beam} in [J] versus magnetic coil currents I_{Coils} at RF-power 400 W, pressure $P_{Cap} = 0.85$ μBar (Flow Q = 3 SCCM), with and without magnet band.

I_{Coils}	With MagCusps	Without MagCusps
0	none	none
1	none	none
2	none	none
3	none	16.1
4	14.8	18.3
5	16.4	19.6
6	18	20.1

Table C.5: Center ion beam density ratio n_{Br} and ion beam velocity ratio v_{Br} versus RF-powers at pressure $P_{Cap} = 0.65\mu$ Bar (Flow Q = 2 SCCM) and magnetic coil current $I_{Coils} = 5$ A.

RF	n_{Br}	v_{Br}
100	1.0604	0.9258
200	1.1121	0.8856
300	1.0855	0.89
400	1.4598	0.9076
500	1.3512	0.8954
600	1.5180	0.8797
700	1.4103	0.9120
800	1.2888	0.9057

Table C.6: Center ion beam density ratio n_{Br} and ion beam velocity ratio v_{Br} versus pressures at RF-Power = 400 W and magnetic coil current $I_{Coils} = 5$ A.

Flow Q	n_{Br}	v_{Br}
2	1.4598	0.90
3	1.6920	0.89
4	1.3367	0.87

Table C.7: Center ion beam density ratio n_{Br} and ion beam velocity ratio v_{Br} versus magnetic coil current I_{Coils} in [A] at RF-Power = 400 W and pressure $P_{Cap} = 0.85$ μBar (Flow Q = 3 SCCM).

I_{Coils}	n_{Br}	v_r
4	1.3515	0.90
5	1.6920	0.89
6	1.6123	0.87

Appendix D

Tables of the RF-power data

This chapter contains tables of the RF-power values with the actual power which goes in the chamber P_{In} and the reflected power P_{Ref}, as well as the VSWR values for each measurement.

Table D.1: RF-Power data at pressure $P_{Cap} = 0.65$ μBar (Flow Q = 2 SCCM), magnetic coil current $I_{Coils} = 5$ A at RF-power range $[100 - 800]$ W.

	With MagCusps			Without MagCusps		
RF	P_{In}	P_{Ref}	VSWR	P_{In}	P_{Ref}	VSWR
100	99	1	1	98	2	1
200	199	1	1	199	1	1
300	299	1	1	297	3	1
400	398	2	1	399	1	1
500	498	2	1	499	1	1
600	597	3	1	595	5	1
700	696	4	1	698	2	1
800	796	4	1	797	3	1

Table D.2: RF-Power data pressure profiles at RF-power = 400 W and magnetic coil current I_{Coils} = 5 A.

	With MagCusps			Without MagCusps		
Q	P_{In}	P_{Ref}	VSWR	P_{In}	P_{Ref}	VSWR
2	399	1	1	399	1	1
3	397	3	1	397	3	1
4	398	2	1	398	2	1

Table D.3: RF-Power data pressure profiles at RF-power = 400 W and magnetic coil current I_{Coils} = 0 A.

	With MagCusps			Without MagCusps		
Q	P_{In}	P_{Ref}	VSWR	P_{In}	P_{Ref}	VSWR
3	399	1	2	399	1	1
4	399	1	1	399	1	1

Table D.4: RF-Power data magnetic coil current profiles at RF-power = 400, pressure $P_{Cap} = 0.85$ μBar (Flow Q = 3 SCCM).

	With MagCusps			Without MagCusps		
I_{Coils}	P_{In}	P_{Ref}	VSWR	P_{In}	P_{Ref}	VSWR
0	397	3	1.26	399	1	1.18
1	399	1	1.36	399	1	1.39
2	399	1	1.21	399	1	1.15
3	399	1	1.21	399	1	1.18
4	399	1	1.21	399	1	1.28
5	398	2	1.30	399	1	1.27
6	398	2	1.30	399	1	1.25

Chapter 8

Bibliography

[1] G. Tribulato, "Characterization of a magnetized plasma in cylindrical geometry," Master's thesis, University of Tromsø UiT, 2007.

[2] M. A. Lieberman and A. J. Lichtenberg, "Principles of plasma discharges and materials processing, 2nd ed." *John Wiley & Sons, Inc., Hoboken, New Jersey*, 2005.

[3] K. K. Barada, P. K. Chattopadhyay, J. Ghosh, S. Kumar, and Y. C. Saxena, "Observation of low magnetic field density peaks in helicon plasma," *Phys. Plasmas*, vol. 20, p. 042119, 2013.

[4] S. W. J. Hopwood, C.R. Guarnieri and J. Cuomo, "Electromagnetic fields in a radio frequency induction plasma," *J. Vacuum Sci. Technol.*, vol. A11, p. 147, 1993.

[5] J. P. Freidberg, "Plasma physics and fusion energy," *Cambridge University Press, New York*, 2007.

[6] F. Isik, "Discussion: Comperative healing of human cutaneous surgical incisions created by the peak plasma blade, conventional electrosurgery, and a standard scalpel," *Plastic and reconstructive Surgery*, vol. 128, p. 112, 2011.

[7] D. B. Graves, "Low temperature plasma biomedicine: A tutorial review)," *Phys. Plasmas*, vol. 21, p. 080901, 2014.

[8] C. T. Russell and C. A. Raymond, "The dawn mission to vesta and ceres," *Space Sci. Rev.*, vol. 163, p. 3, 2011.

[9] J. Brophy, "The dawn ion propulsion system," *Space Sci. Rev.*, vol. 163, p. 251, 2011.

[10] C. Charles, "Plasmas for spacecraft propulsion," *J. Phys D: Appl. Phys*, vol. 42, p. 163001, 2009.

[11] J. Winter, R. Brandenburg, and K.-D. Weltmann, "Atmospheric pressure plasma jets: an overview of devices and new directions," *Plasma Sources Sci. Technol.*, vol. 24, p. 064001, 2015.

[12] L. Block, "A double layer review," *Astrophysics and Space Science*, vol. 55, no. 1, p. 59, 1978.

[13] R. W. Schrittwieser, "Nonlinear potential structures in plasmas," University of Innsbruck, Tech. Rep., 2015.

[14] Å. Fredriksen, L. N. Mishra, and H. S. Byhring, "The effects of downstream magnetic field on current-free double layers and beam formation in the njord helicon plasma device," *Plasma Sources Science and Technology*, vol. 19, p. 034009, 2010.

[15] Å. F. H.S. Byhring, C. Charles and R. Boswell, "Double layer in an expanding plasma: Simultaneous upstream and downstream measurements," *Phys. Plasmas*, vol. 15, p. 102113, 2008.

[16] F. F. Chen, "Helicon discharges and sources: a review," *Plasma Sources Sci. Technol.*, vol. 24, p. 014001, 2015.

[17] G. N. Harding and P. C. Thonemann, "A study of helicon waves in indium," *Proc. Physical Soc.*, vol. 85, p. 317, 1965.

[18] R. Boswell, "Very efficient plasma generation by whistler waves near the lower hybrid frequency," *Plasma Phys. Contr. Fusion*, vol. 26, no. 10, p. 1147, 1984.

[19] P. Chabert and N. Braithwaite, *Physics of radio-frequency plasmas*. Cambridge University Press, New York, 2011.

[20] D. M. Pozar, "Microwave engineering, fourth edition," *John Wiley & Sons, Inc., Hoboken, New Jersey*, 2012.

[21] T. Ohkawa and W. D. Kerst, "Multipole magnetic field configurations for stable plasma confinement," *Il Nuovo Cimento*, vol. 22, p. 784, 1961.

[22] K. N. Leung, R. D. Collier, L. B. Marshall, T. N. Gallaher, W. H. Ingham, R. E. Kribel, and G. R. Taylor, "Characteristics of a multidipole ion source," *Rev. Sci. Instrum.*, vol. 49, p. 321, 1978.

[23] K. Takahashi, K. Oguni, H. Yamada, and T. Fujiwara, "Ion acceleration in a solenoid-free plasma expanded by permanent magnets," *Phys. Plasmas*, vol. 15, p. 084501, 2008.

[24] K. Takahashi, Y. Itoh, and T. Fujiwara, "Operation of a permanent-magnets- expanding plasma source connected to a large-volume diffusion chamber," *J. Phys. D: Appl. Phys.*, vol. 44, p. 015204, 2011.

[25] K. Takahashi, Y. Shida, and T. Fujiwara, "Magnetic-field-induced enhancement of ion beam energy in a magnetically expanding plasma using permanent magnets," *Plasma Sources Sci. Technol.*, vol. 19, p. 025004, 2010.

[26] F. F. Chen, "Performance of a permanent-magnet helicon source at 27 and 13 mhz," *Phys. Plasmas*, vol. 19, p. 093509, 2012.

[27] F. F. Chen and H. Torreblanca, "Permanent-magnet helicon sources and arrays: A new type of rf plasma," *Phys. Plasmas*, vol. 16, no. 057102, p. 057102, 2009.

[28] MathWorks, "http://se.mathworks.com/help/signal/ref/sgolayfilt.html," *Documentation*.

[29] R. L. Stenzel, R. Williams, R. Agüero, K. Kitazaki, A. Ling, T. McDonald, and J. Spitzer, "Novel directional ion energy analyzer," *Rev. Sci. Instrum.*, vol. 53, p. 1027, 1982.

[30] I. H. Hutchinson, "Principles of plasma diagnostics," *Cambridge University Press, New York*, 1987.

[31] K. Junck and W. Getty, "Comparison of argon electron-cyclotron-resonance plasmas in three magnetic field configurations: 2. energy distribution of argon ions," *J. Vacuum Sci. Technol.*, vol. 12, no. 3, p. 760, 1994.

[32] E. Leal-Quiros and M. Prelas, "An enhancement of ion energy spectra resolution and sensitivity in a multigridded energy analyzer with a retarding grid potential: The variable energy analyzer vea," *IEEE Trans. Plasma Sci.*, vol. 16, p. 661, 1989.

[33] T. Honzawa, "Characteristics of gridded energy analyzers in relatively dense plasmas," *Fusion Engineering and Design*, 1997.

[34] G. Severn, D. Edrich, and R. McWilliams, "Argon ion laser-induced fluorescence with diode lasers," *Rev. Sci. Instrum.*, vol. 69, p. 10, 1997.

[35] R.F.Boivin and E. E. Scime, "Laser induced fluorescence in ar and he plasmas with a tunable diode laser," *Rev. Sci. Instrum.*, vol. 74, p. 4352, 2003.

[36] D. Gahan, S. Daniels, C. Hayden, D. O. Sullivan, and M. B. Hopkins, "Characterization of an asymmetric parallel-plate radio frequency discharge using a retarding field energy analyzer," *Plasma Sources Sci. Technol.*, vol. 21, p. 015002, 2012.

[37] C. Bohm and J. Perrin, "Retarding field analyzer for measurements of ion energy distributions and secondary electron emission coefficients in low pressure radio frequency discharges," *Rev. Sci. Instrum.*, vol. 64, p. 31, 1993.

[38] W. J. Miloch, N. Gulbrandsen, L. N. Mishra, , and Å. Fredriksen, "The role of acceptance angle in measurements with ion energy analyzers: Study by numerical simulations," *Appl. Phys. Lett.*, vol. 97, p. 261501, 2010.

[39] Y. Sakai and I. Katsumata, "An energy resolution formula of a three plane grids retarding field energy analyzer," *J. Appl. Phys.*, vol. 24 Part 1, p. 337, 1985.

[40] C. Charles, A. W. Degeling, T. E. Sheridan, J. H. Harris, M. A. Lieberman, and R. W. Boswell, "Absolute measurements and modeling of radio frequency electric fields using a retarding field energy analyzer," *Phys. Plasmas*, vol. 7, p. 5232, 2000.

[41] C. Charles, "A review of recent laboratory double layer experiments," *Plasma Sources Sci. Technol.*, vol. 16, p. R1, 2007.

[42] J. Ling, M. West, T. Lafleur, C. Charles, and R. Boswell, "Thrust measurements in a low-magnetic field high-density mode in the helicon

double layer thruster," *Journal of Physics D. Appl. Phys.*, vol. 43, no. 30, p. 305203, 2010.

[43] F. F. Chen, "The low-field density peak in helicon discharges," *Phys. Plasmas*, vol. 10, p. 2586, 2003.

[44] Y. Wang, G. Zhao, Z. W. Liu, J. T. Ouyang, and Q. Chen, "Two density peaks in low magnetic field helicon plasma," *Phys. Plasmas*, vol. 22, p. 093507, 2015.

[45] K. P. Shamrai and V. B. Taranov, "Volume and surface rf power absorption in a helicon plasma source," *Plasma Sources Sci. Technol., Volume 5, Number 3*, vol. 5, p. 474, 1996.

[46] S. Cho, "The resistance peak of helicon plasmas at low magnetic fields," *Phys. Plasmas 13*, vol. 13, p. 033504, 2006.